

**NPS ARCHIVE**  
**1998.06**  
**SMITH, R.**



DUDLEY KNOX LIBRARY  
NAVAL POSTGRADUATE SCHOOL  
MONTEREY CA 93943-5101







# NAVAL POSTGRADUATE SCHOOL Monterey, California



## DISSERTATION

### LOW LATITUDE IONOSPHERIC EFFECTS ON RADIOWAVE PROPAGATION

by

Rasler W. Smith

June 1998

Dissertation Supervisor:

Richard W. Adler

Approved for public release; distribution is unlimited

Prepared for:  
Naval Information Warfare Center  
9800 Savage Road  
Fort Meade, MD 20755-6000

Center for Reconnaissance Research  
Naval Postgraduate School  
Monterey, CA 93943

**NAVAL POSTGRADUATE SCHOOL  
Monterey, California 93943-5000**

Rear Admiral R.C. Chaplin  
Superintendent

This dissertation was prepared in conjunction with research sponsored in part by the Naval Information Warfare Activity, Fort Meade, MD and Center for Reconnaissance Research, Monterey, CA under Contracts N4175695WR57587 and MIPR 97110-T, respectively.

Reproduction of all or part of this report is not authorized without permission of the Naval Postgraduate School.



**REPORT DOCUMENTATION PAGE**

Form approved

OMB No 0704-0188

Public reporting burden for this collection of information is estimated to average 1 hour per response, including the time for reviewing instructions, searching existing data sources, gathering and maintaining the data needed, and completing and reviewing the collection of information. Send comments regarding this burden estimate or any other aspect of this collection of information, including suggestions for reducing this burden, to Washington Headquarters Services, Directorate for Information Operations and Reports, 1215 Jefferson Davis Highway, Suite 1204, Arlington, VA 22202-4302, and to the Office of Management and Budget, Paperwork Reduction Project (0704-0188), Washington, DC 20503.

**1. AGENCY USE ONLY (Leave blank)****2. REPORT DATE**

June 1998

**3. REPORT TYPE AND DATES COVERED**

Dissertation and Technical Report

**4. TITLE AND SUBTITLE**

Low Latitude Ionospheric Effects on Radiowave Propagation

**5. FUNDING**

N4175695WR57587 and MIPR 97110-T

**6. AUTHOR(S)**

SMITH, Rasler W.

**7. PERFORMING ORGANIZATION NAME(S) AND ADDRESS(ES)**

Naval Postgraduate School  
Department of Electrical and Computer Engineering  
Monterey, CA 93943-5000

**8. PERFORMING ORGANIZATION  
REPORT NUMBER**

NPS-EC-98-010

**9. SPONSORING/MONITORING AGENCY NAME(S) AND ADDRESS(ES)**

Naval Information Warfare Center  
Attn: CNSG/Code N9  
9800 Savage Road  
Fort Meade, MD 20755-6000

and

Center for Reconnaissance Research  
Attn: EC/Po  
Naval Postgraduate School  
Monterey, CA 93943

**10. SPONSORING/MONITORING  
AGENCY REPORT NUMBER****11. SUPPLEMENTARY NOTES**

The views expressed in this report are those of the author and do not reflect the official policy or position of the Department of Defense or the United States Government.

**12a. DISTRIBUTION/AVAILABILITY STATEMENT**

Approved for public release; distribution is unlimited.

**12b. DISTRIBUTION CODE****13. ABSTRACT (Maximum 200 words.)**

This dissertation provides experimental observations and analyses that associate low-latitude transionospheric signal scintillation with transequatorial VHF radio propagation and errors in transionospheric geopositioning. The experiment observed equatorial-region ionospheric total electron content (TEC) derived from Global Positioning System (GPS) signals using receivers on Oahu, Hawaii, Christmas Island, and Rarotonga, Cook Islands. The experiment simultaneously measured VHF transequatorial propagation of VHF television signals from Hawaii to Rarotonga. Analysis shows that a moving second moment of vertical-equivalent TEC strongly correlates to each VHF transequatorial radio propagation event. From experimental observation analysis, the author develops models for prediction of TEP and time-space distribution of low-latitude transionospheric scintillation. The author also develops equations that show the potential errors in time, frequency, and angle used in geopositioning solutions. These three parameters are potentially correctable using these techniques.

**14. SUBJECT TERMS**

Low latitude ionosphere, equatorial, scintillation, geopositioning, Global Positioning System, GPS, Total Electron Content, TEC, transequatorial propagation, TEP

**15. NUMBER OF  
PAGES**  
195**16. PRICE CODE****17. SECURITY CLASSIFICATION  
OF REPORT**

Unclassified

**18. SECURITY CLASSIFICATION  
OF THIS PAGE**

Unclassified

**19. SECURITY CLASSIFICATION  
OF ABSTRACT**

Unclassified

**20. LIMITATION  
OF ABSTRACT**  
SAR





Approved for public release; distribution is unlimited

**LOW LATITUDE IONOSPHERIC EFFECTS ON RADIOWAVE PROPAGATION**

Rasler W. Smith

B.S.E.E., University of Texas at Austin, 1979

M.S.E.E., Naval Postgraduate School, 1990

E.E., Naval Postgraduate School, 1990

Submitted in partial fulfillment of the  
requirements for the degree of

**DOCTOR OF PHILOSOPHY IN ELECTRICAL ENGINEERING**

from the

**NAVAL POSTGRADUATE SCHOOL**

**June 1998**

1 2 3 4 5 6 7 8 9 10 11 12





## ABSTRACT

This dissertation provides experimental observations and analyses that associate low-latitude transionospheric signal scintillation with transequatorial VHF radio propagation and errors in transionospheric geopositioning.

The experiment observed equatorial-region ionospheric total electron content (TEC) derived from Global Positioning System (GPS) signals using receivers on Oahu, Hawaii, Christmas Island, and Rarotonga, Cook Islands. The experiment simultaneously measured VHF transequatorial propagation of VHF television signals from Hawaii to Rarotonga.

Analysis shows that a moving second moment of vertical-equivalent TEC strongly correlates to each VHF transequatorial radio propagation event. From experimental observation analysis, the author develops models for prediction of TEP and time-space distribution of low-latitude transionospheric scintillation.

The author also develops equations that show the potential errors in time, frequency, and angle used in geopositioning solutions. These three parameters are potentially correctable using these techniques.





## TABLE OF CONTENTS

I.	INTRODUCTION .....	1
II.	THE PROPAGATION ENVIRONMENT .....	5
	A. SOLAR EMISSIONS .....	5
	B. THE EARTH'S MAGNETIC FIELD .....	6
	C. THE EQUATORIAL IONOSPHERE .....	8
III.	REMOTE OBSERVATION OF THE EQUATORIAL IONOSPHERE .....	21
	A. IONOSPHERIC SOUNDERS .....	22
	B. GLOBAL POSITIONING SYSTEM .....	30
	C. AIRGLOW MEASUREMENT .....	34
IV.	ANOMALOUS RADIOWAVE PROPAGATION AT LOW LATITUDES ....	37
	A. TRANSEQUATORIAL PROPAGATION .....	37
	B. TRANSIONOSPHERIC PROPAGATION .....	42
V.	THE EXPERIMENTAL DESIGN .....	45
	A. TRANSMITTER AND RECEIVER SITES .....	47
	B. EQUIPMENT EMPLACEMENT .....	48
	C. PREVIOUS DATA .....	51
VI.	THE TRANSEQUATORIAL VHF EXPERIMENT .....	53
	A. CIRCUIT ONSET TIME .....	54
	B. CIRCUIT CESSATION TIME .....	65
	C. CIRCUIT PROBABILITY .....	67

D.	PATH LOSS .....	73
VII.	THE TRANSIONOSPHERIC GPS EXPERIMENT .....	83
A.	TEC OVERHEAD CHRISTMAS ISLAND .....	83
B.	FREQUENCY DOMAIN TEC SCINTILLATION ANALYSIS .....	89
C.	STATISTICAL ANALYSIS OF TEC SCINTILLATION .....	92
D.	TIME-SPACE DISTRIBUTION OF TEC SCINTILLATION .....	94
E.	ELEVATION ANGLE EFFECTS .....	103
F.	TEC SCINTILLATION EFFECTS UPON GEOLOCATION .....	106
G.	SCINTILLATION PREDICTION .....	111
H.	NON-TEP SCINTILLATION .....	115
VIII.	THE ANCILLARY EXPERIMENTS .....	119
A.	THE IONOSONDE EXPERIMENT .....	119
B.	THE AIRGLOW EXPERIMENT .....	128
IX.	CONCLUSIONS AND RECOMMENDATIONS .....	131
A.	TRANSEQUATORIAL PROPAGATION PREDICTION .....	131
B.	SCINTILLATION AND GEOLOCATION .....	132
C.	EXTENSIONS OF CURRENT STUDY .....	135
APPENDIX A.	GEOGRAPHIC TO GEOMAGNETIC COORDINATES .....	139
APPENDIX B.	MAGNETIC DECLINATION ANGLE .....	141
APPENDIX C.	SOLAR MAGNETIC ANGLE .....	143
APPENDIX D.	TEP PREDICTION PROGRAMS .....	145
APPENDIX E.	PROBABILITY OF SCINTILLATION .....	173

APPENDIX F. SCINTILLATION MAGNITUDE PREDICTION .....	177
LIST OF REFERENCES .....	179
INITIAL DISTRIBUTION LIST .....	181





**To Mom and Dad**



## ACKNOWLEDGMENTS

Completing a research effort such as this one requires the cooperation and assistance of many individuals. Besides the sponsors, the Naval Information Warfare Activity and the Center for Reconnaissance Research, who provided financial support, many others graciously furnished time, advice, materials, or equipment. Some of these individuals are mentioned below.

First on my list is Professor Dick Adler who diligently fought to keep the project going for me after the funding vaporized. Besides his professional attitude and determination, his wit and views on life are unmatched and unforgettable. He is an apt role model for all who want to discern the difference between meaningful and meaningless.

For wise counsel and unparalleled knowledge, and his willingness to share that knowledge, I wish to recognize Professor Ray Vincent. He epitomizes the cliché of having forgotten more than I will ever know.

Professor Gus Lott was my Rock of Gibraltar. Besides initially suggesting the project, he was always there when the puzzle pieces didn't mesh. Whether it was finding supplementary funding, a point-of-contact, additional equipment, or technical advice, he was always there and ready to assist.

Without the assistance of the Cook Islands Government, and especially Mr. Stuart Kingan, I could never have completed this project. He and his wife, Tereapii,

opened their house, hearts, and laboratory to me without hesitation. To them I will be forever grateful.

From the Land Down Under, many thanks go the professionals of the Defence Science and Technology Organisation in Adelaide. Special thanks go to Dr. Russell Clarke and Mr. Stephen Leak. Not only did they lend me much needed equipment, but they help me erect, install, troubleshoot, and operate their system.

Saving the best for last, the one who encouraged and stood by me every step of the way, most special thanks to my wife, Franny. Never losing sight of the objective, she was my guiding light, confidant, research assistant, and secretary. I could never have made it without her selfless and competent assistance.



# I. INTRODUCTION

The reflecting layers of the ionosphere have been used to support long-distance communications since the early days of radio. In past years, many communicators have used HF (2 to 30 MHz) for long distance communications, and this band is still widely used for this purpose. Predictions of HF-propagation conditions have evolved to help communicators contend with diurnal, seasonal, and sunspot-cycle variations of the ionosphere. Recent advances in microcomputers have allowed HF-propagation prediction programs to become available to a large number of users at a very low cost.

While HF-prediction programs are highly useful to mid-latitude users, they have many limitations. At high latitudes (above about  $60^\circ$ ) and low latitudes (below about  $25^\circ$ ), prediction programs are less reliable. The mid-latitude ionospheric models do not adequately describe the ionospheric behavior of these areas (the two polar regions considered to be one genre). These areas exhibit anomalous propagation and, as such, are unpredictable. However, through anecdotal reports from amateur radio operators and other observers of radio propagation, it has been noted that these areas not only support HF communications but also VHF communications. Scientific exploration has contributed much to the knowledge of the morphologies of these regions, but attempts at communications-path predictions have generally been unsuccessful. Successful prediction of nighttime transequatorial VHF communications is the first of two major objectives of this dissertation.

Radio signal paths which originate in the northern and terminate in the southern hemisphere at a near-conjugate point (and vice versa) are known collectively as transequatorial propagation (TEP) paths. TEP is further divided into two types, identified as afternoon-TEP and evening-TEP. Afternoon-TEP is characterized by chordal propagation from one equatorial anomaly to the other and thence return to earth. Afternoon-TEP is generally time-restricted to between about 1000 local and sunset and supports frequencies up to about 60 MHz. Similar to mid-latitude propagation, the probability of afternoon-TEP increases with increasing sunspot numbers. Evening-TEP begins sometime after sunset when signals propagate via an ionospheric ducting mechanism. Since the signals are propagated within ducts, frequencies and strengths of the signals are higher than would otherwise be expected. Reports of evening-TEP propagation at frequencies as high as 432 MHz have been reported (Cracknell and Whiting, 1980), and reception at frequencies as high as 200 MHz was detected in this research effort.

The effects on signals influenced by the ducting mechanism mentioned are not all enhancements, however. Severe degradation of signals which pass through the ducts, i.e., to and from satellites, may prevent their reception and demodulation altogether. The signal degradation is a result of amplitude, phase, and frequency scintillation that is induced as the signal passes through the duct. One process which utilizes these transionospheric signals for its operation and is significantly degraded by the ducts, is the geolocation of radio transmitters.

Geolocation can be accomplished by making measurements at the receiver site of angle of arrival (AOA), time difference of arrival (TDOA), and frequency difference of arrival (FDOA). Both AOA and TDOA systems locate the emitter using multiple bearing determinations while FDOA systems use multiple range determinations.

If the receiver is aboard a space-borne vehicle, and the emitter is on or near the earth, the electromagnetic signal must pass through the ionosphere on its journey from the emitter to the receiver. Errors are introduced by the ionosphere to the measurement of angle, time, or frequency of arrival at the receiver.

If the ionospheric region through which the signal propagates is in the mid-latitudes of the earth, the structure and density of the ionospheric layers are sufficiently known and predictable. The mid-latitude ionosphere (in an undisturbed condition) can therefore be modeled with enough accuracy to compensate for the angle- and time-of-arrival errors.

In both high and low latitudes the ionosphere is not stable nor predictable. At present, no reliable model exists to predict ionospheric behavior in these regions. With no reliable models, the errors introduced to the geolocation factors cannot be compensated for, and the location of the emitter-of-interest may be unobtainable. Characterization of scintillation induced by the low-latitude ionosphere is the second major objective of this study.

The ionosphere of the low-latitudes is introduced in Chapter II. The equatorial E-layer electric and magnetic fields are described, which combine to

produce the equatorial anomalies. The instability of the dissipating anomalies is recounted along with duct formation. Methods for observing the ionosphere remotely are detailed in Chapter III with emphasis on equipment which was used in this research campaign. The theories of low-latitude transequatorial and transionospheric radiowave propagation are developed in Chapter IV. Chapter V contains the experimental setup whereby two oppositely-directed radio transmitter-receiver links were established in the mid-Pacific with accompanying ionospheric monitors. And Chapters VI, VII, and VIII include analysis of the collected data and derivations of the prediction algorithms. Algorithms developed in these chapters are included in the appendices as MATLAB programs.

The material of the dissertation falls into two major segments. The initial, Chapters I through IV, is considered background and explanatory. The remaining, given in Chapters V through IX, contains original and novel work including:

- ★ Derivation of low-latitude ionospheric predictors based upon mid-Pacific experiment
- ★ Prediction of TEP based upon TEP observations
- ★ Correlation of TEP and GPS-derived total electron content
- ★ Low latitude scintillation effects upon geolocation
- ★ Temporal and spatial scintillation models using GPS-derived total electron content, and
- ★ Bi-directionality of TEP circuit.



## II. THE PROPAGATION ENVIRONMENT

Free ions and electrons existing above about 90 km altitude constitute the earth's ionosphere. At low latitudes, on each side of the magnetic equator, the structure of the ionosphere differs from any other location. The magnetic equator is the only location in the terrestrial ionosphere where both the electric and magnetic fields are parallel to the surface of the earth. The effects of this singularity create the low-latitude ionosphere with its equatorial anomalies. The cause of this deviation is the complex interaction between the earth's magnetic field and the motions of electrons and ions in the equatorial ionospheric region. Understanding of the physics of the environment is the objective of this chapter.

### A. SOLAR EMISSIONS

Emissions from the sun provide the energy necessary to ionize the neutral molecules of the upper atmosphere. The ionizing energy arrives in two forms: electromagnetic (as either x-rays or ultraviolet rays) and charged particles (electrons, protons, and ions).

Radio noise is also emitted from the sun. The power density of noise at 2800 MHz (wavelength 10.7 cm) is measured daily at a receiving site near Ottawa. This power density, called the 10.7 cm flux, given in units of  $10^{-22} \text{ W m}^{-2} \text{ Hz}^{-1}$ , is reported to scientists at the National Geophysical Data Center (NGDC) in Boulder, CO. They in turn report daily readings (and past values) on their Internet homepage whose

address is <http://www.sel.bldrdoc.gov/today.html>. The flux values vary from about 65 to 250 units at the nadir and peak of the solar cycle, respectively.

Solar emissions are directly proportional to the sunspot number. This is due to heightened flare activity connected with an increase in the number of sunspots. Flares emit electromagnetic energy creating more x-rays and ultraviolet rays.

The 10.7 cm solar flux also increases with the elevated flare activity and as such is a dependable predictor of sunspot number. It reliably indicates energy available for ionization in the atmosphere.

## **B. THE EARTH'S MAGNETIC FIELD**

The magnetic field of the earth can be approximated to first order as a dipole field, with the poles tilted about  $11^\circ$  from the axis formed by the geographic poles. The north geomagnetic pole is located approximately at geographic latitude and longitude  $79.19^\circ$  N and  $70.98^\circ$  W, with the south geomagnetic pole located at  $79.19^\circ$  S and  $109.02^\circ$  E. The magnetic lines of flux leave the south magnetic pole and stream toward the north magnetic pole.

The inclined poles create a need for a new magnetic coordinate system, complete with equator, latitudes, and longitudes. Since the equatorial ionosphere is somewhat symmetric about the magnetic equator, it is necessary to convert from geographic to the geomagnetic coordinates for terrestrial points of interest. A method to compute the geomagnetic coordinates for a point of interest is given in Appendix A.

## 1. Lines of Flux

Magnetic lines of flux originate from the north pole of a dipole magnet and terminate on the south pole (indicating that the earth's magnetic poles are misnamed). As with a bar magnet, however, other lines originate from different locations toward the northern end and terminate at conjugate points on the southern end. This is depicted for the earth in Figure 1, where it is seen that the lines of flux are parallel to the earth's surface over the magnetic equator. The distance from the

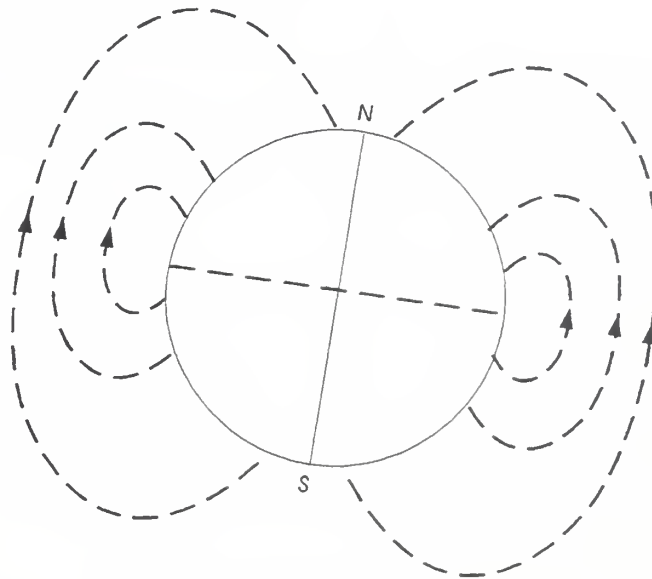


Figure 1. Magnetic lines of Flux.

earth's center to a point on a magnetic field line is found as  $r = R_e L \cos^2 \Phi$ , where  $R_e$  is the earth's radius,  $L$  is the height of the line at its equatorial plane crossing measured in earth radii, and  $\Phi$  is the magnetic latitude of the point of interest. The length of a field line between a point in one hemisphere and its magnetic conjugate in the opposite hemisphere is given by (Davies, 1990)

$$l = \frac{R_e}{\sqrt{3}} \left[ CG + L \ln(C + G) - \frac{L}{2} \ln L \right], \quad (1)$$

where  $C^2 = 3(L - 1)$  and  $G^2 = 4L - 3$ .

## 2. Magnetic Declination Angle

The angle from a point of interest to the geographic north pole is by definition 360 degrees or due north, which is called true north. The great circle heading from this same point of interest to the magnetic north pole is magnetic north. The difference between true north and magnetic north is the magnetic declination angle. A method to compute the magnetic declination angle is derived in Appendix B.

## C. THE EQUATORIAL IONOSPHERE

The earth's ionosphere is created by energy from the sun being imparted to neutral molecules in the upper atmosphere. When this energy is absorbed by a molecule, an electron is separated from the molecule leaving a free electron and an ion. The density of free electrons is the fundamental quantity from which propagation characteristics are derived. Prediction or measurement of the electron density is essential to the quantitative characterization of the ionosphere.

Electron density is generally directly related to the solar zenith angle,  $\chi$ . The solar zenith angle is the angle between a line drawn directly upward from the point of interest on earth to the line drawn from that same point to the sun, as shown in Figure 2. An accurate method of computing the solar zenith angle is given by



Bourges (1985). Since free electron production is maximum when the sun is directly overhead, the densities are generally highest in summer at noon.

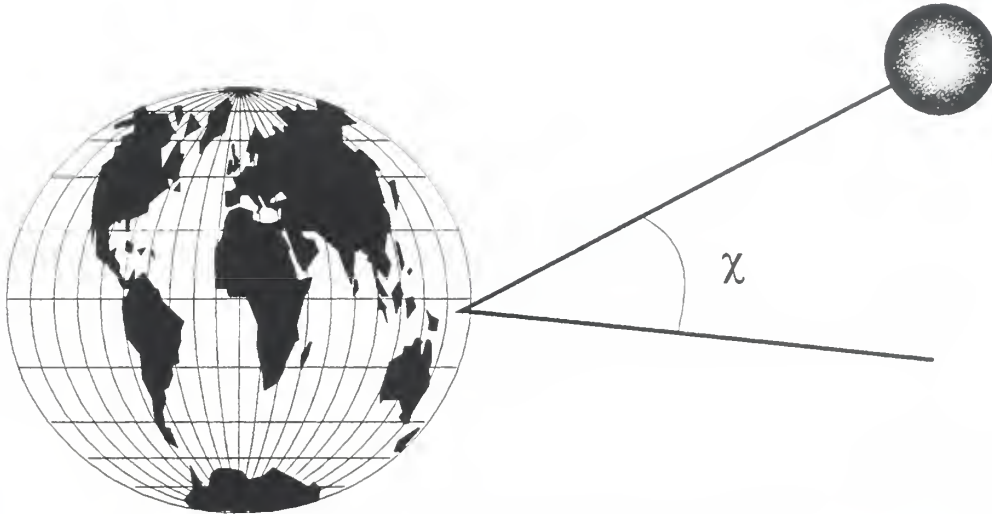


Figure 2. Solar zenith angle.

This generality does not hold at low latitudes. Directly over the equator the electron density is actually less than the densities north and south of the equator due to the *equatorial anomalies*. These equatorial (or Appleton) anomalies are caused by upward electron movement above the equator due to interaction between the earth's equatorial magnetic and electric fields. The equatorial electric field is discussed next.

### 1. The Equatorial Electrojet

The winds of the upper stratosphere interact with the plasma of the lower ionosphere. The prevalent winds in this region are directed upward during the day and downward at night (Woodman, 1970). Electrons and ions created from solar energy are swept up by these winds and move initially in the direction of wind flow, as they attempt to cross lines of flux of the earth's magnetic field. A force

perpendicular to the wind direction is applied to the charged particles by the lines of flux. This results in the ions being deflected in one direction and the electrons in the other (i.e., one west and the other east). The deflecting force due to the magnetic field is

$$\vec{F} = q\vec{V} \times \vec{B}, \quad (2)$$

where  $F$  is the force,  $q$  is the amount of charge,  $\mathbf{V}$  is the velocity of the charged particle, and  $\mathbf{B}$  is the magnetic flux density. The net effect of the deflections is a current flow directed in the east-west direction. This current flow is called the equatorial *electrojet*.

The electrojet occurs approximately 105 km above the earth in the E region. The current density at midday attains a value of about 14 A/km<sup>2</sup> west-to-east which creates an electric field directed in the same direction as the current, peaking at about 0.5 mV/m (Forbes, 1981; Hargreaves, 1992). Therefore, the earth's magnetic and electric fields' interaction with the neutral winds and the ionized particles of the lower ionosphere generates an electric field which encircles the globe above the magnetic equator. The field is directed from both the day and the night sides toward the dusk terminator, as shown in Figure 3.

## 2. The Equatorial Anomalies

Above the magnetic equator there are two fields, both parallel to the surface of the earth. The magnetic field is aligned magnetically south to north and, at all points above the magnetic equator, parallel to the earth's surface. During the day, the electric field is directed from magnetic west to magnetic east along the magnetic

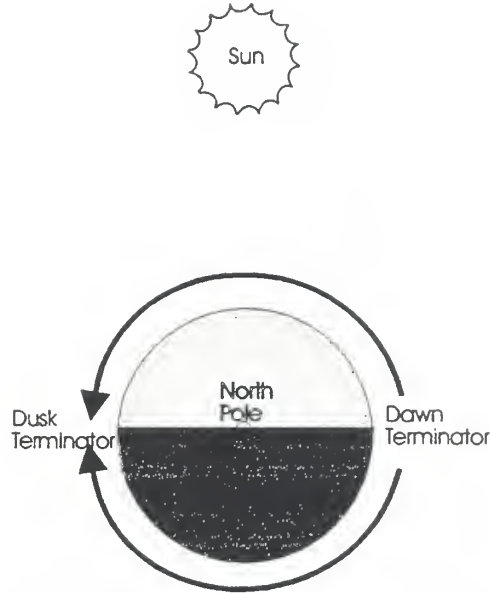


Figure 3. The earth's equatorial electric field (After Kelley, 1989).

equator and at all points parallel to the earth's surface. The interaction between these perpendicular fields and the free electrons, which are created by the ionizing energy, produces a condition called the *fountain effect*.

The fountain effect is the electrodynamic lifting of free electrons above the magnetic equator. The underlying physics can be seen by first dividing both sides of Eq. 2 by the charge,  $q$ , to obtain the electric field  $\mathbf{E}$ , i.e.,

$$\vec{E} = \frac{\vec{F}}{q} = -\vec{V} \times \vec{B}, \quad (3)$$

where the minus sign indicates the velocity of the electrons. Equation 3 can be crossed into  $\mathbf{B}$  to obtain

$$\vec{E} \times \vec{B} = (-\vec{V}_{\perp} \times \vec{B}) \times \vec{B}, \quad (4)$$

where the velocity which is perpendicular to both  $\mathbf{E}$  and  $\mathbf{B}$  is  $\mathbf{V}_{\perp}$ . Application of a

common vector identity to Eq. 4 produces

$$\begin{aligned}\vec{E} \times \vec{B} &= \vec{V}_{\perp}(\vec{B} \cdot \vec{B}) - \vec{B}(\vec{B} \cdot \vec{V}_{\perp}) \\ &= \vec{V}_{\perp} B^2.\end{aligned}\tag{5}$$

Thus the electrons move in the direction of  $\vec{E}$  crossed into  $\vec{B}$ , with velocity

$$\vec{V}_{\perp} = \frac{\vec{E} \times \vec{B}}{B^2}.\tag{6}$$

It is observed that the perpendicular electron velocity is independent of both its mass and charge. Indeed, a parallel derivation of the perpendicular velocity for the ions results in an identical equation. For the earth's orientation of the magnetic and electric fields, the perpendicular velocity is vertical: upward during daylight and downward during darkness. A representative magnitude of the midday velocity can be found by assuming the electric field to be 0.5 mV/m and the magnetic field at 50  $\mu\text{Wb}/\text{m}^2$  to produce a typical initial velocity of 10 m/s directed upward.

During the day electrons continue to be lifted until the effects of pressure, gravity, and the magnetic field overcome the effects of the  $\vec{E} \times \vec{B}$  field. The net result of the electric and magnetic field interaction is that free electrons and ions over the magnetic equator are forced straight up, rising to altitudes of up to 1000 km (Hargreaves, 1992). The electrons and ions then follow the magnetic lines of flux back toward the earth, increasing the electron density both north and south of the magnetic equator at latitudes of about 10 to 20 degrees. The electron density over the equator is thereby diminished due to the fountain effect. The fountain effect is illustrated in Figure 4.

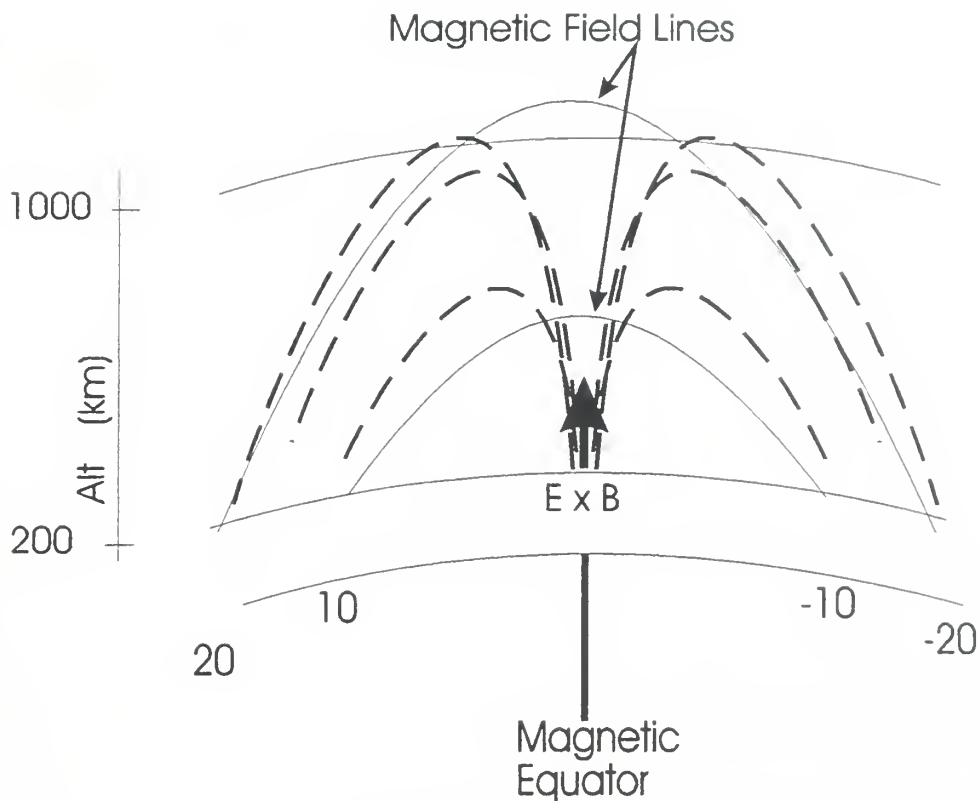


Figure 4. The fountain effect.

After sunset the E-region neutral winds shift from upward to downward. With the velocity vector downward, the electrojet reverses, flipping the polarity of the electric field. The  $\mathbf{E} \times \mathbf{B}$  plasma motion described by Eq. 6 now forces the electrons and ions downward, pulling plasma from the overhead area directly over the magnetic equator and evacuating the upper regions. The high plasma density of the anomalies begins to migrate back toward the magnetic equator, following the magnetic field lines, as shown in Figure 5. The dynamics of this plasma migration are unstable. If an outside perturbation stimulates this instability, the ensuing upheaval can affect the nighttime ionosphere by contributing to the formation of ionospheric “bubbles” or “ducts” also known as Equatorial Spread-F (ESF).

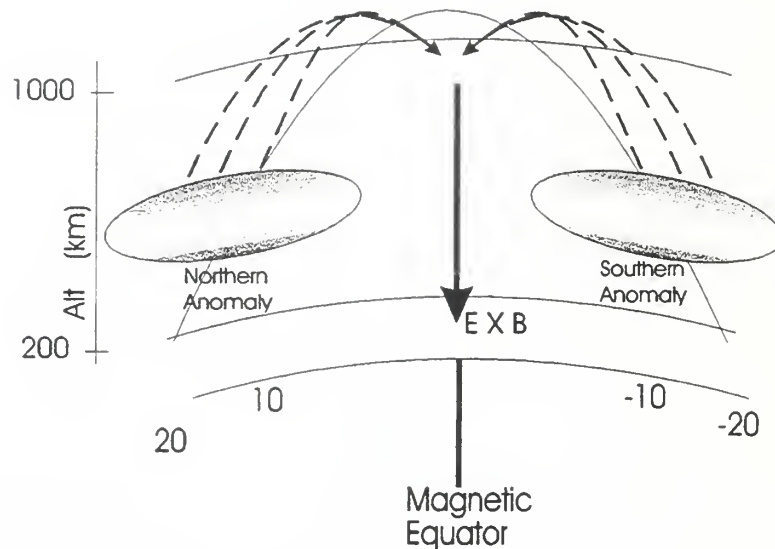


Figure 5. Plasma migration from anomalies to equator.

### 3. Equatorial Spread-F

Early ionospheric researchers using ionosondes observed the occurrence of a nighttime spread-F on equatorial ionograms. (Examples of ionograms with ESF are shown in Chapter III.) Their term for this phenomenon, Equatorial Spread-F, still survives today. Other names found in the literature, emphasizing different aspects of ESF, are ducts, bubbles, and plumes. ESF is also responsible for scintillations which occur on satellite communications signals at low latitudes. Equatorial scintillations have been observed at frequencies as high as 7 GHz. (Hargreaves, 1992)

The causes of ESF are still under discussion in the scientific arena, with many theories, both linear and non-linear, being advanced by different researchers. It is not known what initiates ESF, nor why it occurs one night and not the next. It is known that nighttime long-range transequatorial propagation of VHF signals, the observation of equatorial spread-F, and satellite signal scintillation are all different



manifestations of the same physical event. The onset of ESF has its origin in the formation of ionospheric ducts.

#### 4. Equatorial Ionospheric Ducts

After sunset, the ionizing energy from the sun vanishes and the formation of ions and free electrons in the ionosphere ceases. Equatorial anomalies lose their source of electrons and begin a process of equalizing the densities across the equator, as was shown in Figure 5. Left undisturbed, anomaly electrons migrate back toward the equator, refill the pocket of diminished electron density over the equator and, sometime after local midnight, the equatorial ionosphere is indistinguishable from the mid-latitude ionosphere. This is precisely what occurs on some evenings. When this orderly migration occurs, no other anomalous behavior ensues, i.e., no ESF, no TEP, and no scintillation.

On other evenings, some mechanism (possibly gravity waves) disturbs the orderly migration of electrons back toward the equator. A perturbation can cause turbulence to erupt within the anomalies. This evolution can be understood by first considering the undisturbed situation shown in Figure 6. As seen, the viewpoint is looking north at the juncture of the ionosphere and the free-space region of the stratosphere. The magnetic field lines are pointing north into the page and the electron density is  $N$  electrons/ $\text{m}^3$ . Gravity attempts to force the charged particles to descend in the direction of the acceleration,  $g$ , but the particles are held in place by the magnetic field. The manifestation of the opposing force of  $\mathbf{B}$  is a current flow generated in the direction indicated by  $\mathbf{J}$  in the figure. In an electrically neutral

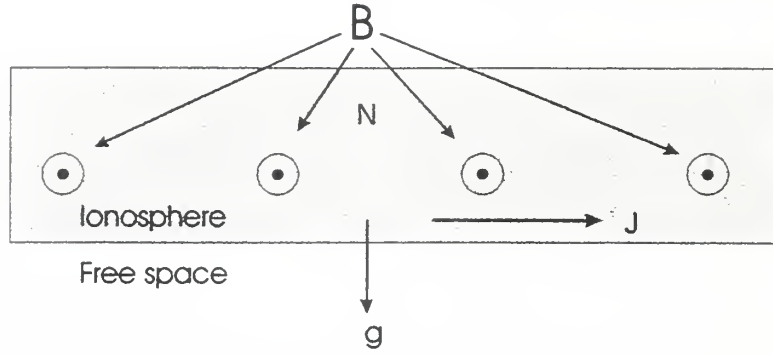


Figure 6. Current produced by gravity/B interaction.

ionosphere (the number of ions equals the number of electrons), the current density is given by Chen (1984) as

$$\vec{J} = N(M + m) \frac{\vec{g} \times \vec{B}}{B^2}, \quad (7)$$

where  $m$  and  $M$  are the electron and ion masses, respectively. Current flowing as indicated on the figure creates an electric field pointing in the same direction. The resulting  $\mathbf{E} \times \mathbf{B}$  force opposes the  $g$  force and keeps the charged particles from falling, resulting in a steady-state condition.

This steady-state becomes unstable in the presence of an external electric field. In Figure 7 the equilibrium situation of Figure 6 has been altered by the presence of a transient electric field. With positive alternations of the transient field, the upward directed  $\mathbf{E} \times \mathbf{B}$  force is augmented by  $\Delta \mathbf{E} \times \mathbf{B}$ , which overcomes the force of gravity, causing the plasma to ascend. With negative alternations, the opposite effect occurs, forcing the plasma in this region downward. The vortex formed by plasma motion destabilizes the ionosphere within the anomalies, creating a rising bubble which is devoid of plasma. The plasma which was contained in the

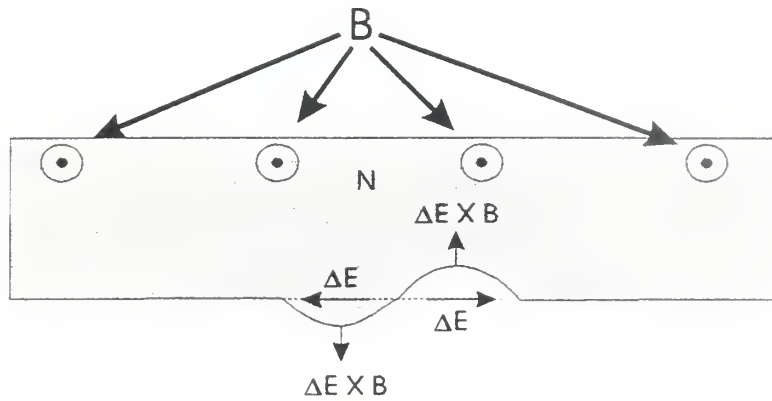


Figure 7. Transient electric field influence on  $E \times B$  field.

plasma-deficient bubble is forced to the top of the bubble. Initial stages of bubble formation was captured by the Altair non-coherent scatter radar at Kwajalein Island and is shown in Figure 8. The deficient region extends from the base of the ionosphere near 300 km to beyond 500 km.

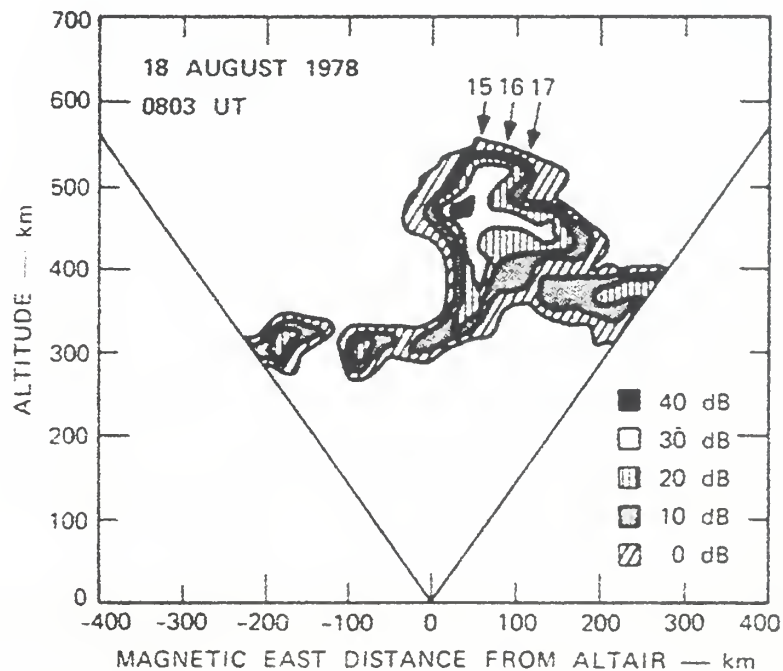


Figure 8. Initial bubble formation over Kwajalein (From Tsunoda, 1981)

Observations indicate an ascending of the deficient region similar to that observed when air bubbles rise within a heavier covering liquid, demonstrating a Rayleigh-Taylor instability. As the plasma-deficient region of the bubble rises into the denser area, it spreads north and south along magnetic field lines and grows higher and elongates toward the magnetic poles. Steep density gradients form at the boundary between the deficient area and the surrounding highly ionized area, forming an elongated duct. (Kelley, 1989)

Mature ducts extend to locations near the anomalies (i.e.,  $\pm 20^\circ$ ). Although their dimensions vary, an average configuration has been observed to be ovate with the east-west dimension approaching 50 km and the vertical dimension spanning 200 km. The electron density within the bubble itself is very low but at the ceiling it is high, with a density differential of three orders of magnitude (Tsunoda, 1981). The structure developed by this formation is an ionospheric duct, which can act as a waveguide, that traps north-south traveling electromagnetic waves and allows them to propagate over great distances to the opposite hemisphere. The structure of the duct ceiling is not homogeneous; it is imbedded with tube-like irregularities of varying size. Each irregularity, depending on its size and density, bends and delays, by differing amounts, electromagnetic signals passing through it, which can cause satellite signal scintillations. A pictorial representation of an ionospheric duct is shown in Figure 9.

After formation, the ducts migrate eastward in the nighttime equatorial ionosphere, due to prevailing nighttime eastwardly winds at F-region heights (Fejer,

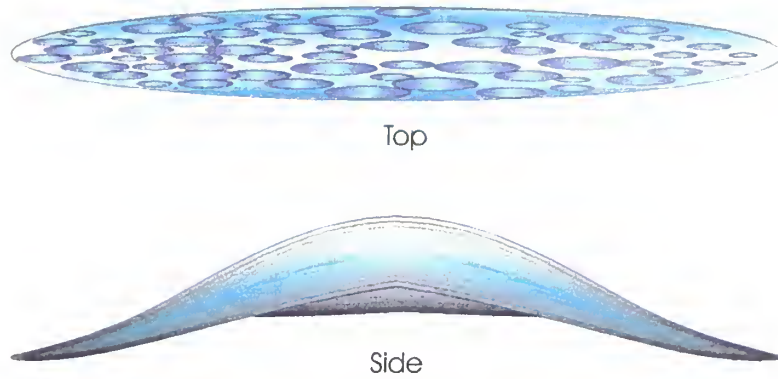


Figure 9. Top and side views of an ionospheric duct

et al., 1981). Duct formation is varied; single and multiple ducts can form, all migrating eastward. An overhead representation of these migrating ducts is shown in Figure 10. The imbedded irregularities move with the duct, producing different

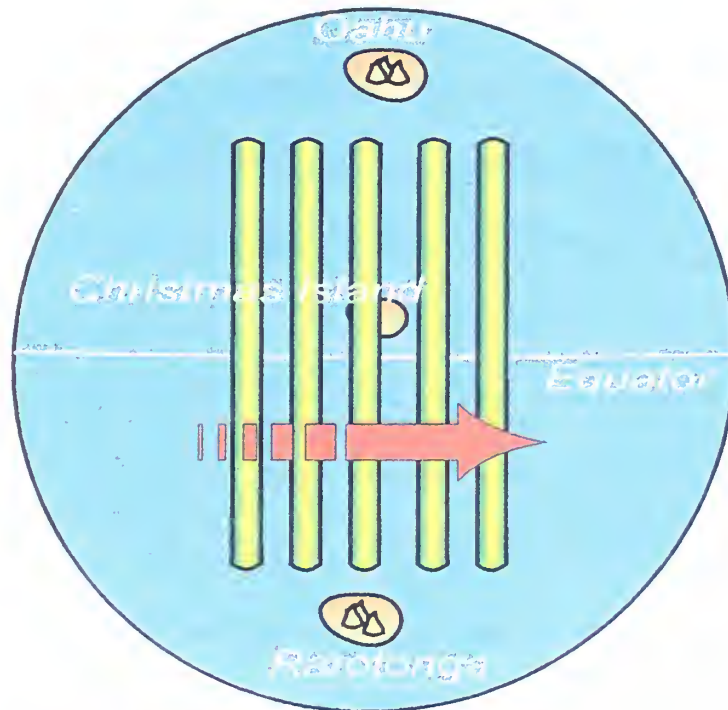


Figure 10. Ionospheric ducts moving eastward in nighttime sky

amounts of signal path bending, attenuation, delay, and Doppler frequency shift for an electromagnetic wave passing through the duct. This variation in signal

amplitude, phase, and frequency is called scintillation. Although an overhead duct may migrate eastward and no longer influence the area of the earth where it formed, other ducts which may have formed to the west progress overhead and continue to affect local observations.

Propagating electromagnetic waves, incident on duct apertures at appropriate angles can become trapped within the ducts. Propagation within a duct is analogous to waveguide propagation. Ducts follow magnetic lines of flux which have large radii of curvature (Hargreaves, 1992).



### III. REMOTE OBSERVATION OF THE EQUATORIAL IONOSPHERE

Knowledge of equatorial ionospheric conditions is essential for both conducting scientific ionospheric studies and for updating real-time employment. For example, the presence of an overhead duct indicates whether or not TEP is possible or whether there might be satellite communications scintillation. There are several methods by which the presence of an overhead duct can be ascertained. Regardless of the ionospheric observation method used, results may not apply beyond a few hundred miles in longitude. Propagation conditions may not be the same or even similar at a location distant from an observation site.

Remote ionospheric observation can be accomplished by using equipment based either on the earth or on satellites. Satellite-based observation equipment provides important information about the topside portion of the ionosphere which cannot be observed from earth. Since the goal of this research was to help characterize the behavior of the lower ionosphere, particularly with respect to equatorial spread-F and ducts, only earth-based observation equipment was used.

Active earth-based observation equipment includes coherent and non-coherent scatter radars, and vertical and oblique incidence sounders. Passive devices are Faraday rotation and time-of-flight measuring equipment, and atomic recombination airglow monitors. The equipment used for ionospheric monitoring during this experiment consisted of an oblique sounder, apparatus to measure time-of-flight of transionospheric signals, and an airglow monitor.

## **A. IONOSPHERIC SOUNDERS**

Ionospheric sounders, also called ionosondes, are monostatic or bistatic. The monostatic ionosonde is configured to monitor the ionosphere directly overhead in the vertical incidence configuration, or with an obliquely-launched antenna elevation angle, to monitor the ionosphere at a distant point using ionospheric backscatter. The bistatic ionosonde is used exclusively to observe ionospheric conditions over the path between the transmitting and receiving antennas in the oblique incidence mode.

Regardless of type, ionosondes emit pulsed, swept-frequency signals, analogous to that of a chirp radar. The time-of-flight is measured from transmission to reception, from which the ionospheric layer heights can be inferred. Sweeping the frequency allows the electron density of the layers to be ascertained.

The output data from sounders is stored graphically, depicting the layer heights on an ionogram. Newer, digital ionosondes (digisondes) store the data on magnetic media which can be evaluated using analysis software or displayed as an ionogram.

Although not used in this experiment, the vertical incidence sounder is described first. Oblique incidence sounder theory is derived from that of the vertical incidence sounder.

### **1. Vertical Incidence Ionosondes**

Creating ionograms using the vertical incidence ionosonde (VI) is the oldest method for monitoring the overhead ionosphere, and is still widely used today. A typical VI sweeps over a frequency range of 0.1 to 30 MHz in a time period of a few

seconds to a few minutes (Davies, 1990). A pulse at each frequency is transmitted, after which the sounder switches to the receive mode for a certain length of time. If an echo is received at that frequency, the round trip time of flight is measured, and a computed layer height is recorded. The next frequency is then transmitted and the process repeated.

Echos are created by the electromagnetic pulse being apparently *reflected* from an ionospheric layer. Although reflection is the assumed mechanism for returning the energy, it is actually returned through the process of refraction. When waves propagate from a medium of one refractive index into a second region with a different refractive index, the wavefront is bent or refracted. Ignoring collisions and the magnetic field, the refractive index of the ionosphere is given by Davies (1990) as

$$n \approx \sqrt{1 - \frac{f_N^2}{f^2}}, \quad (8)$$

where  $f_N$  is the plasma frequency. The plasma frequency is a quantity dependent upon physical constants and the plasma electron density, i.e.,

$$f_N = \left( \frac{Ne^2}{4\pi^2\epsilon_0 m} \right)^{1/2}, \quad (9)$$

where  $e$  and  $m$  are the charge and mass of an electron and  $N$  is the electron density in electrons/m<sup>3</sup>. These variables are all constants except for  $N$  so that

$$n \approx \sqrt{1 - \frac{80.5N}{f^2}}. \quad (10)$$

As the electron density increases, the plasma frequency rises, and for a given frequency,  $n$  decreases.

The refractive index for the ionosphere is therefore a function of frequency. The range over which the refractive index varies can be divided into three frequency dependent regions: (1)  $f > f_N$ , so that  $0 < n \leq 1$ , (2)  $f = f_N$ , and  $n = 0$ , and (3)  $f < f_N$ , yielding  $n < 0$ . Application of Snell's law to these three cases reveals that in region 1 the wavefront is bent toward the denser medium, in region 2 the wavefront is bent 90 degrees indicating a maximum height is attained (called the height of reflection  $h_r$ ), and in region 3, the refractive index is imaginary, signifying an evanescent region. The conclusions to be drawn from these observations are if (1)  $f > f_N$ , the propagating wavefront will be bent but not returned, (2)  $f = f_N$ , the wave is reflected from the layer, and (3)  $f < f_N$ , the wave will not propagate within that region.

The VI therefore operates by monitoring echos as the frequency is increased. The frequency at which an echo no longer returns is equal to the plasma frequency for the layer, from which  $N$  can be computed. The height at which this occurs is the layer height. This operation is conducted for each of the reflecting ionospheric layers, i.e., the E,  $F_1$ , and  $F_2$  layers. The plasma frequencies for these three layers are named  $f_0E$ ,  $f_0F_1$ , and  $f_0F_2$ , respectively. An idealized daytime vertical incidence ionogram is shown in Figure 11. At night the ionogram consists of just two traces, as the  $F_1$  disappears after sunset. Above the plasma frequency for each layer, the

transmitted signal does not return an echo, but instead escapes to a higher layer or to outer space.

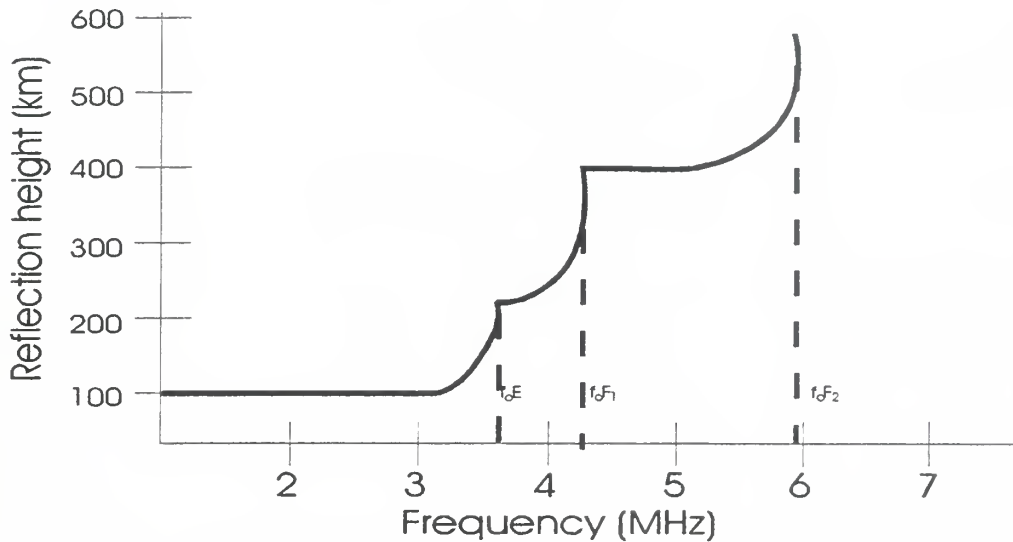


Figure 11. Ideal vertical incidence ionogram (After Hunsucker, 1991).

The presence of ESF in a vertical ionogram is the result of overhead ducts. Therefore, the VI can be utilized to signal the presence of an ionospheric duct overhead. The manifestation of ESF on the vertical incidence ionogram is that the reflections from the F layer are not the clean, coherent echos as shown in the figure above. Instead, the reflecting layer becomes dispersed in altitude, spreading the F-layer return. An example of an equatorial spread-F vertical incidence ionogram is shown in Figure 12.

The first frame of the figure begins in the upper left corner where four ionogram traces are seen. The bottom trace represents the E layer, while the other three depict the F layer. The lowest F layer trace is the actual F-layer return and the other two are round trip reflections from the earth. In the first frame, the E and first F layer returns are clean, nearly ideal traces.

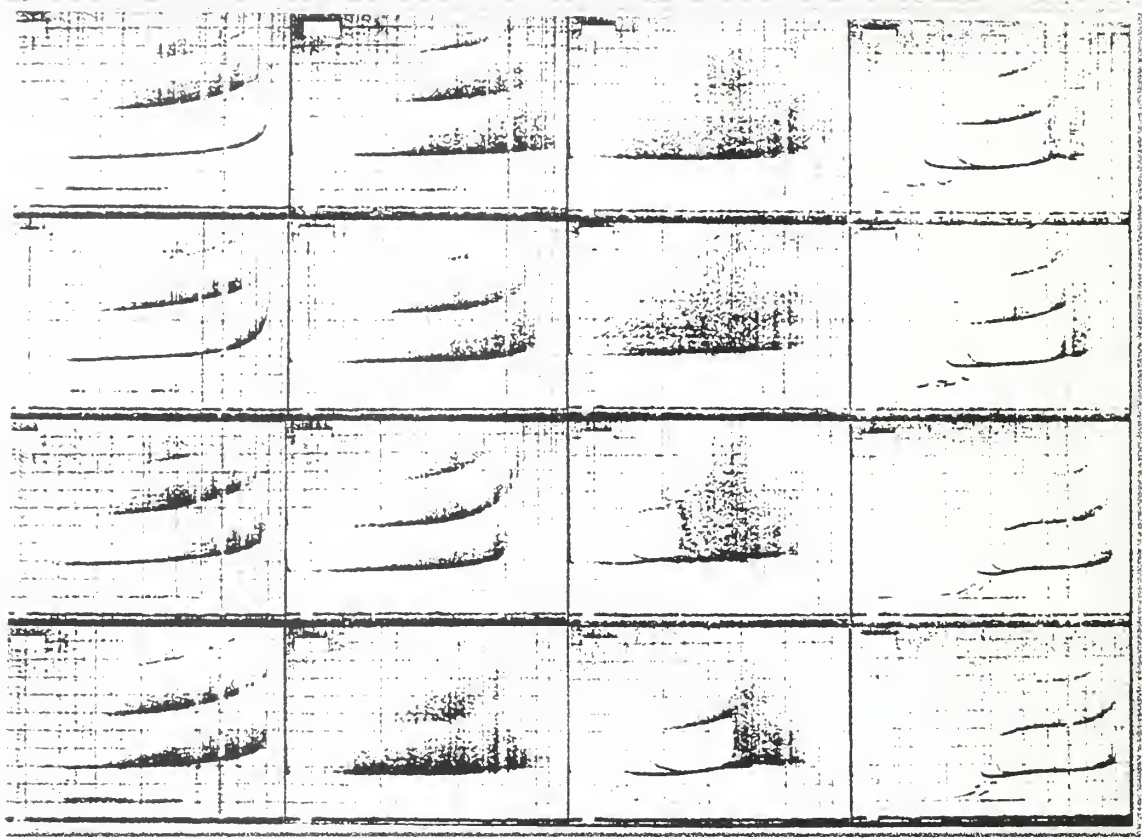


Figure 12. Equatorial spread-F progression. Beginning in upper left corner, then down, second column, etc., the times of each frame are: 2215, 2230, 2245, 2300, 0000, 0100, 0300, 0330, 0400, 0500, 0515, 0530, 0545, 0600, 0645, and 0700. (From McNamara, 1991)

Directly below the first frame, fifteen minutes later, the second frame shows the first F-trace beginning to acquire some “fuzz” or spread in height. The F-spread can be seen in the later frames to progressively deteriorate until morning when the layers re-form. From these ESF returns, overhead duct presence can be easily ascertained due to the spread on the F traces. It will be shown that ESF is readily recognizable from oblique incidence ionograms, as well.



## 2. Oblique Incidence Ionosondes

The oblique incidence ionosonde (OI) is situated with its transmitter and receiver spatially separated, usually over great distances. Depending upon the number of ionospheric hops between transmitter and receiver, several ionospheric reflection points can contribute to the composition of the ionogram. To preclude the ambiguities caused by the multi-hop path, the circuit planner usually limits the path length to that of one hop, approximately 4000 km in the mid-latitudes. When sounding across the magnetic equator, the single hop distance can be extended beyond 4000 km due to chordal reflection by the anomalies during the day, and trapping within an ionospheric duct at night.

The operation of the OI is similar to that of the VI. However, the transmitter and receiver of the VI are co-located and operate from the same precise clock. The OI operates from two separate clocks which must be synchronized in order to accurately measure time of flight of the propagating signals. Modern-day sounders utilize GPS timing to maintain synchronicity between the clocks.

The OI ionogram differs from that of the VI in two principal respects. First, the plasma frequency of the layers is effectively increased, so that a higher frequency can be reflected by an ionospheric layer, and second, a high or Pederson ray propagates obliquely (but not vertically), modifying the appearance of the oblique ionogram. The reflection frequency increase will be discussed first.

The angle formed at the ionospheric entrance point by the Poynting vector of the propagating wave and the vertical is called the incidence angle,  $\phi_0$ . (The

incidence angle of a VI wave is zero.) Snell's law states  $n_0 \sin \phi_0 = n_1 \sin \phi_1 = \text{const.}$  The first region is free space, i.e.,  $n_0 = 1$ , and the second region is at the point of reflection. Snell's law indicates  $\sin \phi_0 = n_r \sin \phi_r$ , where the r subscript betokens the reflection point. The incidence angle at the point of reflection is  $\phi_r = 90^\circ$  producing a refractive index at reflection

$$n_r = \sin \phi_0. \quad (11)$$

By substituting this value for n into Eq. 8, the frequency that reflects from the layer is found as

$$f = f_N \sec \phi_0. \quad (12)$$

Since  $\sec \phi_0 > 1$  for oblique incidence, the frequency that will reflect is always greater than that at vertical incidence.

The effect of higher frequencies being reflected on the oblique ionogram is that the layer traces of Figure 11 will be pushed to the right, i.e., an individual trace will bend toward the vertical at a higher frequency as shown in Figure 13. Also shown in the figure are the results of the second modifier of the OI ionogram, the Pedersen ray, which is discussed next.

As a reflection-bound ray with frequency  $f$  progresses obliquely into an ionospheric layer, it eventually reaches the point in the layer at which  $f = f_N \sec \phi_0$  where it is reflected. If this point is not at the peak electron density of the layer, the plasma frequency increases at altitudes higher than the reflection point. This factor allows for the possibility of a second ray satisfying the requirements of Eq. 12.

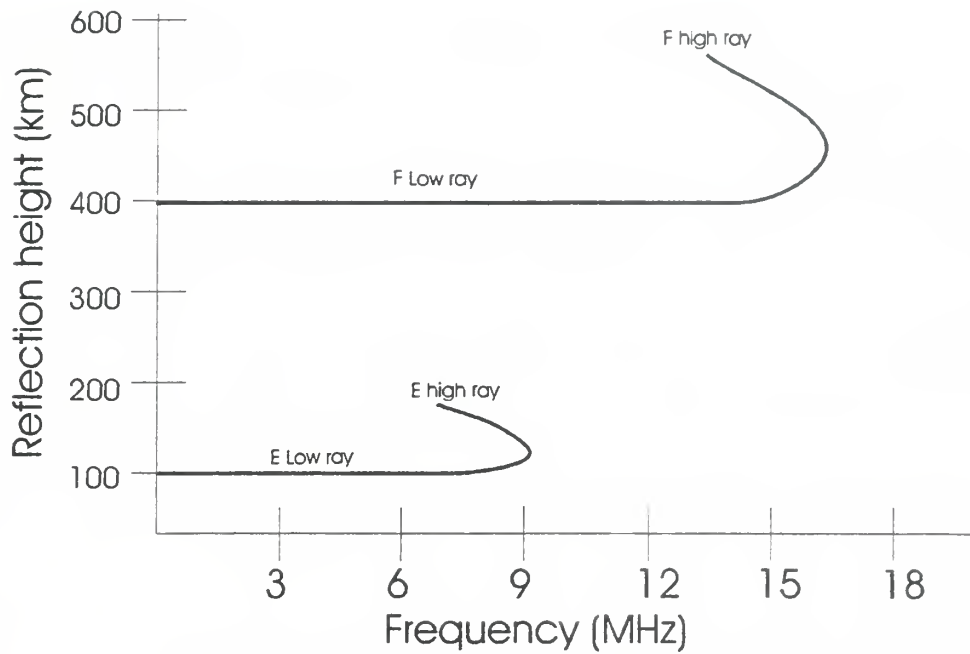


Figure 13. Ideal oblique incidence ionogram.

In Eq. 12, for a fixed frequency  $f$ , there are two degrees of freedom which can satisfy the equality. The first is found by solving for the incidence angle when  $f_N$  is fixed at a value less than layer maximum. The other is established by letting  $f_N$  assume the plasma frequency value at the peak of the layer. The equality can still be satisfied by decreasing the incidence angle. This second ray is called the Pedersen ray. Since this ray ascends higher into the layer than the first, the Pedersen ray is also called a high ray. When  $f_N$  for the first or low ray occurs at the peak of the layer, there is only one ray for the path.

The Pedersen ray produces its own trace on the OI ionogram. For every frequency transmitted there are two paths for the signal to propagate from transmitter to receiver, producing two traces on the ionogram (Nielson and Hagn, 1964). The second trace is not always detected however, since it suffers greater

attenuation over its longer path length. When the transmitted frequency reaches the peak plasma frequency for the layer, the two traces converge into one.

## B. GLOBAL POSITIONING SYSTEM

Sounders can be used to determine peak electron density and height. They convey no information concerning the total electron content of the ionosphere, however. By measuring the time of flight of transionospheric signals using the Global Positioning System, the ionospheric total electron content, and how it varies, can be observed.

The Global Positioning System (GPS) consists of a network of twenty-four active semisynchronous satellites which broadcast continuous, phase-modulated signals on two precise frequencies. The period of each satellite is approximately twelve hours. The signal passes through the ionosphere en route from the satellite to the earth-borne receiver. Precise measurements of the time of flight from transmitter to receiver can be made, from which the total electron content of the ionosphere can be deduced.

The two signals broadcast by each satellite, called L1 and L2, are transmitted on a pair of coherently derived frequencies. They are coherent in that they are integer multiples of a common base frequency,  $f_0$ , where

$$f_0 = 10.23 \text{ MHz.} \quad (13)$$

The frequency of L1 is set at

$$f_1 = q_1 f_0 = 154f_0 = 1575.42 \text{ MHz.} \quad (14)$$

and for L2 is

$$f_2 = q_2 f_0 = 120f_0 = 1227.60 \text{ MHz.} \quad (15)$$

(The constants  $q_1 = 154$  and  $q_2 = 120$  are multipliers of the base frequency.) Since the ionosphere is a dispersive medium, coherency between the two frequencies allows for precise measurement of how the ionosphere affects each frequency.

The primary function of a GPS receiver is to measure the time required for L1 and L2 to travel from a GPS satellite to the receiver. This is accomplished by the use of very stable local oscillators to measure the carrier phase of both L1 and L2 with great accuracy. As these “transionospheric” signals pass through the ionosphere en route to earth, the effects caused by the ionosphere can be detected, measured, and quantified, particularly, the difference in phase between L1 and L2.

As shown in Section A, the ionospheric index of refraction is a function of frequency and, for frequencies much greater than the plasma frequency, Eq. 8 can be approximated by (Hargreaves, 1992)

$$n \approx 1 - \frac{\omega_N^2}{2\omega^2} \quad (\omega \gg \omega_N), \quad (16)$$

where  $\omega_N = 2\pi f_N$ . The value of  $f_N$  was given as a function of  $N$  in Eq. 9 so that

$$\omega_N^2 = 3182N. \quad (17)$$

Substitution of  $\omega_N^2$  into Eq. 16 yields the refractive index

$$n \approx 1 - \frac{1591N}{\omega^2} = 1 - \frac{40.3N}{f^2}, \quad (18)$$

where  $\omega$  is in radians/second and  $f$  in hertz.

As an electromagnetic wave travels a distance  $\ell$  through a medium, the phase change through the medium is  $\Delta\phi = -\beta\ell$  (where  $\beta$  is the phase constant in radians per meter), if  $\beta$  is constant in the medium. If  $\beta$  is not constant, the phase must be found from integration, i.e.,

$$\Delta\phi = - \int \beta \, d\ell = - \int \frac{\omega n}{c} \, d\ell. \quad (19)$$

After  $n$  is inserted from Eq. 18, the phase change after passing through an ionized medium becomes

$$\begin{aligned} \Delta\phi &= -\frac{\omega}{c} \int n \, d\ell = -\frac{\omega}{c} \int \left[ 1 - \frac{1591N}{\omega^2} \right] d\ell \\ &= -\frac{\omega}{c} \ell + \frac{1591}{\omega c} \int N \, d\ell. \end{aligned} \quad (20)$$

The first term is simply the phase delay that occurs after traveling a distance  $\ell$  at the speed of light,  $c$ . The second term represents the phase advance caused by the ionized medium, where the refractive index is less than unity. The integral term is called the *total electron content* (TEC) of the ionized medium,

$$TEC = \int N \, d\ell, \text{ electrons/m}^2. \quad (21)$$

When the results are combined, the phase change is

$$\Delta\phi = -\frac{\omega}{c} \ell + \frac{5.3 \times 10^{-6}}{\omega} TEC = -\frac{2\pi}{\lambda} \ell + \frac{8.44 \times 10^{-7}}{f} TEC, \quad (22)$$

where  $\lambda = c/f$  and  $\omega = 2\pi f$ .



At the receiver, the phase can be measured but the values of  $\ell$  and TEC which contributed to it are unknown—one equation and two unknowns. With a two-channel GPS receiver, a second equation is added (the phase measurement on L2 as well as L1), while the values of  $\ell$  and TEC do not change. For the phase measurements to be combined in a meaningful way, they are normalized to the base frequency by dividing by their frequency multipliers,  $q_1$  and  $q_2$ . The normalized phase measurements of L1 and L2 are

$$\phi_i = -\frac{2\pi}{q_i \lambda_i} \ell + \frac{8.44 \times 10^{-7}}{q_i f_i} TEC = -\frac{2\pi f_0}{c} \ell + \frac{8.44 \times 10^{-7}}{q_i^2 f_0} TEC, \quad i = 1, 2. \quad (23)$$

The difference between these normalized phase measurements yields

$$\begin{aligned} \delta\phi &= \phi_2 - \phi_1 = \left( -\frac{2\pi f_0}{c} \ell + \frac{8.44 \times 10^{-7}}{q_2^2 f_0} TEC \right) - \left( -\frac{2\pi f_0}{c} \ell + \frac{8.44 \times 10^{-7}}{q_1^2 f_0} TEC \right) \\ &= \frac{8.44 \times 10^{-7}}{f_0} TEC \left( \frac{1}{q_2^2} - \frac{1}{q_1^2} \right) = \frac{8.44 \times 10^{-7}}{10.23 \times 10^6} TEC \left( \frac{1}{120^2} - \frac{1}{154^2} \right). \end{aligned} \quad (24)$$

Solving for TEC,

$$\begin{aligned} TEC &= 4.44 \times 10^{17} \delta\phi \frac{\text{electrons}}{\text{m}^2} \\ &= 44.4 \delta\phi \text{ TEC units}, \end{aligned} \quad (25)$$

where 1 TEC unit is equivalent to  $1 \times 10^{16}$  electrons/m<sup>2</sup>.

The TEC is a measure of the number of free electrons in the ionosphere between the observer and the satellite. In a stratified ionosphere, as is normally assumed at mid-latitudes, the TEC remains virtually constant throughout the day.

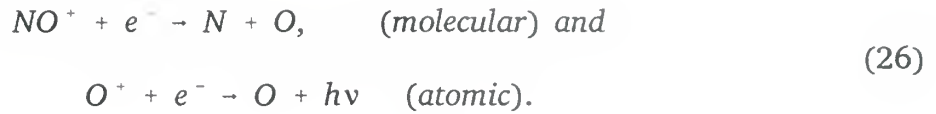
There are gradual changes associated with the amount of ionizing energy from the sun, so that at noon the TEC is expected to be at its peak and diminished somewhat at other times. In the tropical ionosphere, stratification is not expected nor usually observed. As ducts move overhead, the number of free electrons varies continuously, producing the subsequent changing of the TEC between observer and satellite. From the algorithm described in Eq. 25, the variation of TEC can readily be derived from measurements over time of the phase of L1 and L2 at the receiver.

Once the variation of TEC is determined, its value can be substituted into Eq. 22 to find the ensuing fluctuation of the phase of the received signal. This fluctuation is the phase scintillation. Phase scintillation can prevent the receiver from being able to tune and lock on to the incoming signal.

### **C. AIRGLOW MEASUREMENT**

The earth's atmosphere is comprised primarily by nitrogen and oxygen with lesser amounts of argon, carbon dioxide, helium, and hydrogen. As the altitude above the earth varies, the partial pressures contributed by each component varies. At different altitudes, different components become predominant. Between the altitudes of about 200 - 650 km, the predominant component is atomic oxygen. (Hargreaves, 1992)

When solar energy ionizes atoms and molecules, the free electrons begin to recombine with positively charged ions. Two types of recombination occur: molecular and atomic, examples of which are



The atomic recombination emits a photon with energy  $h\nu$  where  $h$  is Planck's constant and  $\nu$  is the photon radiation frequency. The molecular recombination occurs at a rate of about 1000 times that of the atomic recombination (Kelley, 1989). The second reaction is said to be radiative as a photon is emitted.

After sunset, solar ionization ceases and no new ions are created. Molecular recombination occurs rapidly leaving only the atomic ions available for further recombinations. Between 200 and 650 km, in the F-region, the predominant component is atomic oxygen, constraining the majority of the ions to be  $O^+$ . Recombination with  $O^+$  is radiative and a photon is released as the recombined atom returns to ground state energy level. The predominant energy level of these photons is such that they radiate a red color at 630 nm wavelength (Hargreaves, 1992). It has been determined that 630 nm emission originates predominantly between 200 and 400 km (Weill, 1966). Radiative emissions in the ionosphere, such as these, are called airglow.

Airglow is measured by the photon emission rate in Rayleighs,  $R$ , where

$$1R = 10^6 \text{ photons cm}^{-2}\text{s}^{-1}. \tag{27}$$

Emission rates are directly proportional to the electron density (Steiger, 1966) so that measurement of the airglow recombination rate is an indirect method of measuring electron density. Observation of airglow is accomplished by using a

photometer which is an optical device with a large viewing angle but a small bandwidth. Typical photometers have bandwidths of a few tens of angstroms.

To summarize the foregoing paragraphs, by measuring the 630 nm airglow, the electron density of the F-region, particularly between 200 and 400 km, can be ascertained.

Airglow photometers can be used near the magnetic equator to monitor the low latitude ionosphere. Since overhead ducts have a deficiency of electrons and ions, there are fewer recombinations than outside the duct. With fewer recombinations, the airglow intensity is diminished looking up into the duct. As the ducts move eastward in the nighttime sky, a contrast can be seen between the dimly glowing ducts and the separating ionosphere. Airglow deficient regions have been observed in the equatorial region to extend to about 1200 km north-south and 50-200 km east-west (Weber, et al., 1978).

## **IV. ANOMALOUS RADIOWAVE PROPAGATION AT LOW LATITUDES**

Propagation of radiowaves which does not follow accepted behavior is considered anomalous. In low latitudes, non-standard propagation caused by the ionosphere can be traced to the equatorial anomalies and the instabilities that arise upon their dissipation. Because of the high electron density of the anomalies, the sphere-of-influence of the ionosphere is no longer limited to just the High Frequency (HF) band as in mid-latitudes, but extends into VHF and beyond.

This low-latitude anomalous behavior can be divided into two domains: extended range propagation across the magnetic equator on terrestrial paths, and inordinate scintillation on earth-space links. The first domain falls under the general heading of transequatorial propagation while the second appertains to transionospheric propagation.

### **A. TRANSEQUATORIAL PROPAGATION**

Sky wave propagation entails a radiowave transmitted by an earth-bound antenna in the skyward direction, with subsequent ionospheric reflections before being received at a distant location. If the wave experiences only one ionospheric reflection en route, the path is termed single hop. Due to the spherical geometry of the earth and the ionospheric layers, standard single-hop paths are limited to approximately 4000 km. The frequencies which are supported over these long-range paths are restricted to HF.

Long-range single-hop sky wave propagation in the north-south direction across the magnetic equator can occur over distances much greater than 4000 km. The literature contains many cases of established links in excess of 5000 km at frequencies into the VHF band. Some reports of low-UHF propagation have also been documented. Anomalous propagation of this genre is known as transequatorial propagation (TEP).

Transequatorial propagation can be categorized into two separate types. The first is a daytime phenomenon involving the anomalies, called afternoon-TEP. The second occurs after sunset utilizing ionospheric ducts, called evening-TEP.

### **1. Afternoon-TEP**

The anomalies are created by the fountain effect which repositions free electrons created over the magnetic equator. This produces two regions of anomalously high electron density. It was shown in Chapter III that an oblique incidence sky wave will reflect from the ionosphere at altitudes where  $f = f_N \sec \phi_0$ . The plasma frequency is proportional to the electron density so that the inordinately high electron density of the anomalies will reflect higher than normal sky wave frequencies.

The high electron density of the anomalies explains how higher than normal frequencies can be propagated, but it does not justify the increase in single-hop propagation distance. The reason for increased propagation distance is visualized by observing that the radiowave can reflect from one anomaly to the other and thence back to earth, as is depicted in Figure 14.



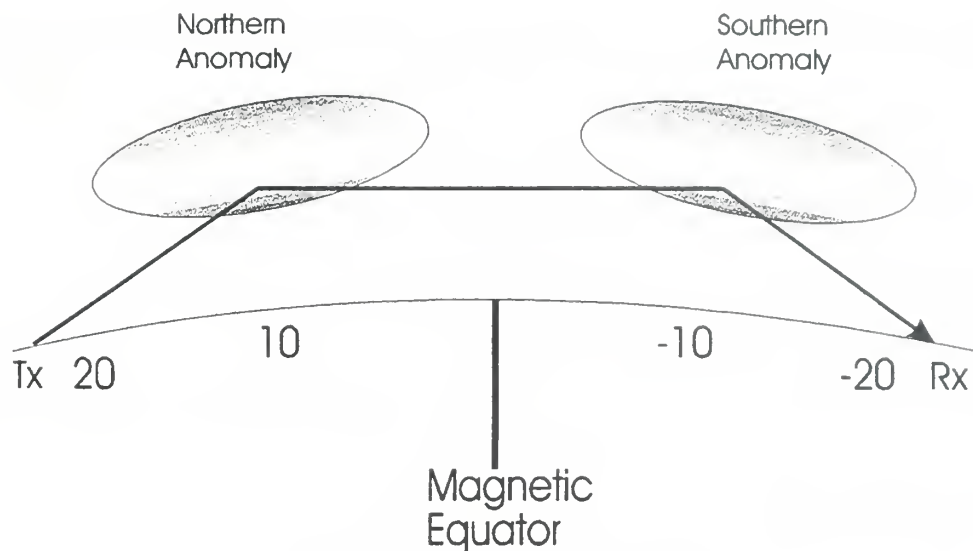


Figure 14. Afternoon-TEP.

## 2. Evening-TEP

After sunset the migration of the anomaly electrons back toward the magnetic equator can become unstable. As was discussed in Chapter II, this instability results in the formation of ionospheric ducts which extend from one equatorial anomaly to the other. The ceilings of the ducts follow the magnetic field lines, raising the tops of the ducts, over the magnetic equator, to several hundred km in altitude.

A duct can act as a waveguide, trapping a properly oriented north-south traveling radiowave. Once trapped, the wave is subsequently guided to the opposite hemisphere. Because of the curvature of the duct, the reflections within the duct occur in a “whispering gallery” mode whereby only the ceiling of the duct is used for reflection. This results in low reflection loss and allows high signal strengths to be received in the opposite hemisphere. The losses which do occur result primarily from aspect-dependent coupling at the apertures of the duct, discussed next.

For TEP there is no direct free space path between the transmitter and the receiver. The losses which contribute to the path loss of TEP are:

- 1) free space loss exterior to duct,  $L_{FS}$ ;
- 2) coupling losses entering and exiting the duct,  $L_C$ ; and
- 3) reflection losses within the duct,  $L_R$ .

The total loss is  $L_T(\text{dB}) = L_{FS}(\text{dB}) + L_C(\text{dB}) + L_R(\text{dB})$ . These loss locations are illustrated in Figure 15.

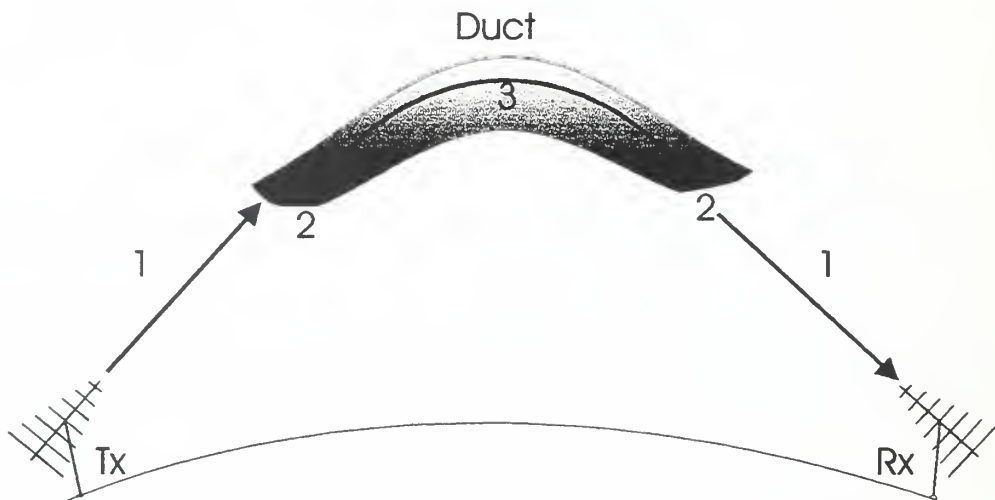


Figure 15. Path losses from transmitter to receiver via ionospheric duct.

The free space spreading loss represented by locations 1 are easily computed if the heights of the duct apertures are known; the loss at positions 2 is a function of the difference between the direction of the Poynting vector of the propagating wave and the axis of the duct; and the losses shown at position 3 are normally quite low since the ceiling electron density is high. Loss factors 1 and 3 are fairly static with low variation, leaving the variations in the path loss mainly a result of the coupling losses of loss factors 2.

The coupling losses which result as a difference in the wavefront propagation directions and the axes of the duct of factors 2 are dependent upon several different variables. Among these are the height of the duct aperture, the height of the apex of the duct (which follows the magnetic flux lines), and the relative positions of the transmitter and receiver sites on the ground with respect to their optimum ground positions, addressed in the following paragraph..

These physical height parameters of the duct are not known a priori but the ranges of movement are generally known and can be statistically modeled. The optimum positions on earth for signal transmission and reception can be determined by using the mean values of the heights. Studies of these positions have been made both experimentally and theoretically (Heron, 1981; Platt and Dyson, 1989), and the optimum north-south positions have been found to be approximately  $\pm 18^\circ$  magnetic latitude. The optimum east-west positions are for the magnetic longitudes of the two sites to the same.

Platt and Dyson, in their theoretical waveguide modeling, show a span of reception locations on the earth varying from  $14^\circ$  to  $26^\circ$  magnetic latitude and  $\pm 2^\circ$  from the transmitter magnetic longitude. The further the reception position is from the optimum position, the lower the magnitude of the received signal will be due to coupling losses.

When scattered worldwide reports of the transmit and receive locations are considered, the latitudinal limits of the Platt and Dyson model are seen to be reasonable. However, Nielson (1969) successfully established a TEP path with a

difference in longitude of  $6^\circ$ . This indicates that the theoretical limit of  $\pm 2^\circ$  in longitude difference is too conservative, and that the limit should be at least  $\pm 6^\circ$ .

## **B. TRANSIONOSPHERIC PROPAGATION**

The anomalous propagation of TEP discussed above has beneficial ramifications in that the propagation distance and frequency range have been enhanced. The transionospheric effects are not beneficial and can be disastrous. The effect upon radiowaves which pass through an ionospheric duct is scintillation in phase, amplitude, and frequency, sometimes severe. Intense scintillation has been observed on radiowaves passing through the low latitude ionosphere at frequencies as high as 7 GHz (Hargreaves, 1992).

Scintillation causes problems for all radio receivers. It prevents receiver lock-on, demodulation, and error-free reception, etc. In this report, scintillation effects upon geolocation will be emphasized and demonstrated. Geolocation methods include Angle of Arrival (AOA), Time Difference of Arrival (TDOA), and Frequency Difference of Arrival (FDOA).

The cause of the low-latitude scintillation was discussed in Chapter II, where it was shown that the duct ceilings are imbedded with myriad-sized tube-like enhancements of electron density irregularities. Electromagnetic waves passing through these irregularities are bent and delayed.

Quantifying the effects upon transionospheric radiowaves can be achieved by utilizing the total electron content explained in Chapter III. The TEC is found using GPS receivers, and the following scintillation-induced quantities can be derived.

## 1. Time Delay

The differential phase change due to propagation through an ionized region was found, in Eq. 22 in Chapter III, to be

$$\Delta\phi_{ion} = \frac{8.44 \times 10^{-7}}{f} TEC. \quad (28)$$

Changes in phase and time can be related as

$$\Delta\phi = 2\pi f \Delta t, \quad (29)$$

and the time delay associated with the phase change of Eq. 28 is

$$\Delta t = \frac{8.44 \times 10^{-7}}{(2\pi f) f} TEC = \frac{1.34 \times 10^{-7}}{f^2} TEC. \quad (30)$$

This time delay has the potential to degrade a TDOA geolocation solution.

## 2. Doppler Shift

A frequency change can be induced into a signal passing through an ionized region. The change in instantaneous radian frequency, as a function of time, is found by differentiating the signal phase with respect to time, i.e.,  $\Delta\omega = \Delta\phi/\Delta t$ . The phase of the transionospheric signal was given in Eq. 22, and by differentiating,

$$\Delta\omega = 2\pi\Delta f = \frac{d}{dt} \left( \frac{8.44 \times 10^{-7}}{f} TEC \right). \quad (31)$$

The change in cyclic frequency is found as

$$\Delta f = \frac{8.44 \times 10^{-7}}{2\pi f} \frac{d}{dt} (TEC) = \frac{1.34 \times 10^{-7}}{f} \frac{d}{dt} (TEC) \text{ Hz}. \quad (32)$$

Frequency changes have deleterious effects on FDOA systems.

### 3. Angular Deviation

By definition, a wavefront undergoing refraction changes propagation direction. Since the refracting ducts are in motion and comprised of random shapes and electron densities, the modifications in direction of the waves passing through them are difficult to ascertain. If the wave approaches the tube from directly above, the angular change in direction can be estimated from wedge refraction theory (Davies, 1990) as

$$\alpha = \frac{c}{2\pi} \frac{8.44 \times 10^{-7}}{f^2} \frac{d}{dx} (TEC) = \frac{40.3}{f^2} \frac{d}{dx} (TEC), \quad (33)$$

where  $d/dx$  (TEC) is the change in the TEC in the horizontal direction. Angular direction changes can destroy the geolocation solution for AOA systems.



## V. THE EXPERIMENTAL DESIGN

There are two distinct, independent manifestations of the presence of an ionospheric duct: (1) the trapping of a propagating radiowave within the duct and subsequent shunting to the opposite hemisphere and (2) the scintillations induced upon waves passing through the duct. These are shown in Figure 16. The two

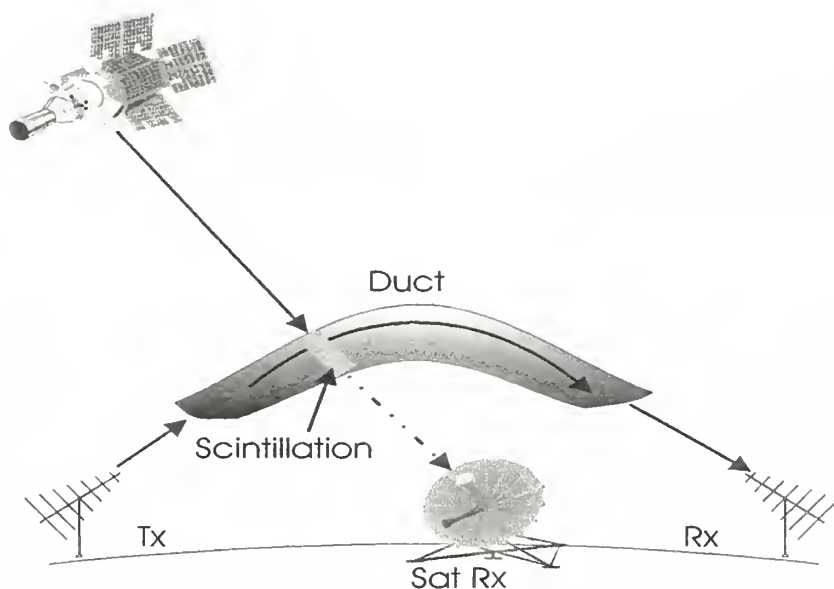
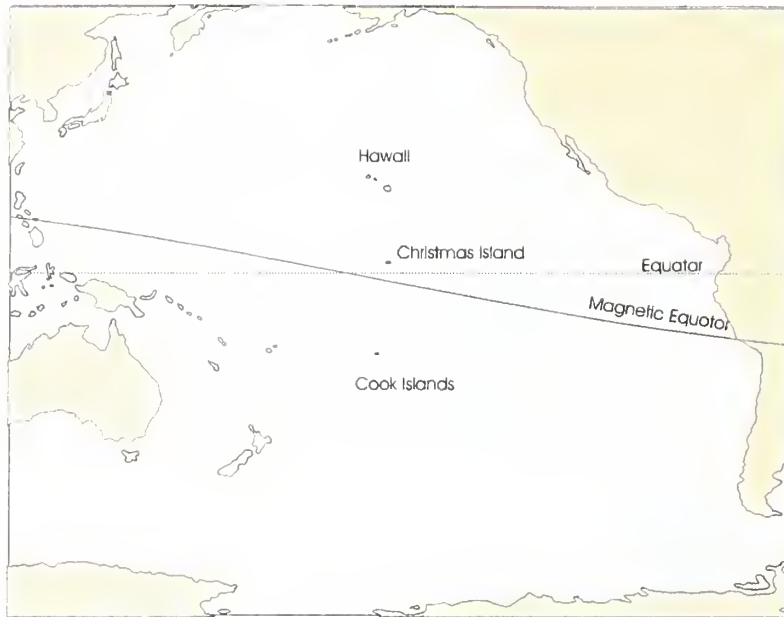


Figure 16. Terrestrial signal trapping and space signal scintillation.

events are temporally and geographically correlated and the presence of one implies a probability of the other.

To exploit this correlation, first a terrestrial radio link was established between the Hawaiian Islands in the north Pacific and the Cook Islands in the south Pacific. The geography is shown in Figure 17.



**Figure 17.** Central Pacific showing Hawaii, Cook Islands, and Christmas Island.

The transmitted signal was commercial television station KHON Channel 2 in Honolulu, between 54 and 60 MHz. A receiver was placed in Rarotonga in the Cook Islands with a recorder calibrated to record received signal power of the video carrier at 55 MHz.

Concurrently, a Global Positioning System receiver was collocated with the receiver in Rarotonga to monitor the total electron content of the ionosphere of the southern Pacific. The Jet Propulsion Lab (JPL) maintains a GPS-TEC receiver in the Hawaiian Islands. The data from this receiver (and many others as well) is posted to their web page. This data was utilized as an ionospheric observation of the northern Pacific. Since the viewing region of these two GPS receivers did not overlap, a third GPS receiver was placed near the equator on Christmas Island. The viewing region of this third receiver overlapped the regions of the first two.

The concurrent monitoring of both a TEP signal via radios, and of the ionosphere using GPS, provides information about the nighttime low-latitude ionosphere and its effects on radiowave propagation. The addition of two complementary pieces of monitoring equipment for a short time period enhanced this monitoring capability. The first was collocating an airglow monitor with the GPS receiver to observe the nighttime equatorial ionosphere above Christmas Island. The other was the installation of an oblique ionosonde over the same path as the TEP circuit but directed in the opposite direction. The sounder not only supplies data concerning the bi-directionality of the path, but delivers daytime propagation path characteristics as well.

The purpose of this experiment was threefold: 1) determine factors which control TEP, either deterministically or statistically, 2) determine if scintillation can be correlated with the occurrence of TEP, and 3) develop predictive capability of TEP and temporal and spatial occurrence of scintillation.

The remainder of this chapter outlines the criteria used in the selection of the sites for the different equipment locations.

#### **A. TRANSMITTER AND RECEIVER SITES**

The equatorial ionosphere should first be modeled based on an ideal, benign environment. Only by modeling thus can any predictability of the occurrence of ESF or ionospheric ducts can be expected. There is no location on earth which provides a completely benign environment, but candidate areas should be free of radical temperature, wind, and magnetic deviation changes.

In addition to a moderate environment, the transmit and receive locations which are to be used in that environment must be within latitudinally limited regions where known TEP originates and terminates, i.e, approximately  $15^{\circ}$  –  $25^{\circ}$  magnetic latitude.

A third useful feature is the ability to monitor the local ionosphere at the transmitter and receiver sites, and at mid-point of the path, the magnetic equator. Equatorial monitoring should be at or near the sub-propagation point of the TEP signal.

The sites selected meet all the above requirements. The transmitter was located on Oahu in the Hawaiian Islands and the receiver was on Rarotonga in the Cook Islands. The first requirement is met since the propagation path is entirely over the Pacific Ocean with no mountains to alter the neutral winds, the magnetic equator is very near the geographic equator, and the magnetic declination is about  $11^{\circ}$  . The second requirement is met since TEP observations have been made on this path for 30 years. The third requirement is met by Christmas Island situated at  $2^{\circ}$  north of the equator, very near the sub-propagation path.

## **B. EQUIPMENT EMPLACEMENT**

### **1. Oahu**

The selected VHF transmitter, TV Channel 2, KHON has an omnidirectional antenna with an ERP of 100 kW located at 21.32N, 157.85W geographic, 21.45N, 91.11W magnetic. The station operates 23 hours per day, with one hour off for

maintenance. The maintenance hour is always after midnight and therefore does not pose insurmountable difficulties in observing nighttime TEP.

During September 1995 the receive portion of an oblique sounder was emplaced on Oahu. The site location was at the Navy's NCTAMS on Wahiawa. The sounder itself is the property of and on loan from the Defence Science and Technology Organisation (DSTO) of Adelaide, Australia (analogous to an arm of DOD). The frequency of the sounder transmitter swept from 2 to 70 MHz which was received on three different antennas. The first receiving antenna for the frequency range 2 – 32 MHz was a rosette, already in place at Wahiawa, which was not being used for other purposes. The second, which was used for 32 – 55 MHz, was a log periodic array (LPA), property of DSTO. The last antenna, an off-the-shelf Winegard TV yagi, was used for 55 – 70 MHz. The clock was maintained precisely using GPS. The received frequency and time of flight were stored as digital ionograms on the receiving suite's computer hard drive.

## **2. Rarotonga**

Two VHF receivers were located at the receive site in Rarotonga, at the laboratory of the Cook Islands Scientific Officer, Mr. Stuart Kingan. The lab was situated at 21.22S, 159.74W geographic, 20.53S, 84.64W magnetic, for a transmitter-receiver separation distance of approximately 4700 km. The magnetic longitude separation between transmitter and receiver was 6.47 degrees. The receivers were tuned to the carrier frequency of the TV transmitter from KHON

Channel 2. Each receiver was fitted with a low-band TV Winegard LP-Yagi antenna with pre-amps, one polarized horizontally and the other vertically. Calibrated AGC voltage of each receiver was fed to a dual trace chart recorder. The signal strength was derived by conversion of the calibrated AGC whenever the ducts exist and allow TEP from the Oahu transmitter.

During September 1995, the transmitter for the oblique sounder was collocated with the VHF receivers in Rarotonga. As with the receiver, the clock was maintained with GPS timing. The swept sounder frequency signal was transmitted from two antennas, twenty-four hours per day. The first antenna, used for 2 – 30 MHz, was an inverted Vee. The second, used from 30 to 70 MHz, was a terminated rhombic.

A GPS TEC system was collocated at the receiver site. The GPS equipment was a dual receiver, 12 channel, Z-12 Ashtech. With two receivers, both L1 and L2 can be received simultaneously for up to 12 different satellite transmitters. The TEC measurements were made and recorded continuously.

### **3. Christmas Island**

A GPS TEC Z-12 Ashtech system was emplaced at the NOAA site, 2.01N, 157.4W geographic, 2.64N, 86.86W magnetic, on Christmas Island. The TEC was monitored and recorded continuously. For a short period in September 1995, an airglow monitoring system was erected and overhead measurements made and recorded nightly by Dr. Michael Taylor from Utah State University.



### C. PREVIOUS DATA

An added bonus to this particular path is that Mr. Kingan has recorded the start and stop times of the reception of this same TV signal at Rarotonga in the past. His data are continuous from April 1966 through December 1976. He has graciously provided this data which has been incorporated into the analysis.



## VI. THE TRANSEQUATORIAL VHF EXPERIMENT

The data collected during the experiment outlined in Chapter V will be analyzed, and when appropriate, prediction algorithms developed. The data analyzed in this chapter are the VHF reception measurements, which were collected at Rarotonga from April 1966 to December 1976 and from March 1995 to March 1996. The early data consists of the start and stop times of the reception of TV Channel 2, at 55 MHz, from Honolulu. The latter data are a continuous monitoring of the signal strength received from Channel 2.

In Chapter V it was noted that two receivers were used to monitor Channel 2, one with vertical and the other with horizontal polarization. As expected, due to the polarization becoming random during ionospheric propagation, neither polarization delivered a power level statistically greater than the other. In October 1995, one of the receivers was re-tuned to monitor other frequencies in addition to Channel 2. Successful reception of frequencies up to and including Channel 11, at 200 MHz, from Honolulu has been observed even though the receiving antenna's bandwidth extends only to Channel 6, at about 90 MHz.

Analysis of the data is concentrated on those aspects of the communications medium necessary for the existence of a circuit. Predictions of the probabilities of a circuit existing, the starting and stopping times, the frequencies which will propagate, and the path loss are the goals. Several of these factors are directly controlled by the relative position of the sun and by the strength of the solar flux.

## A. CIRCUIT ONSET TIME

The circuit commencement times for the continuous period from April 1966 to December 1976 are plotted in Figure 18. Path onset times are seen to exhibit

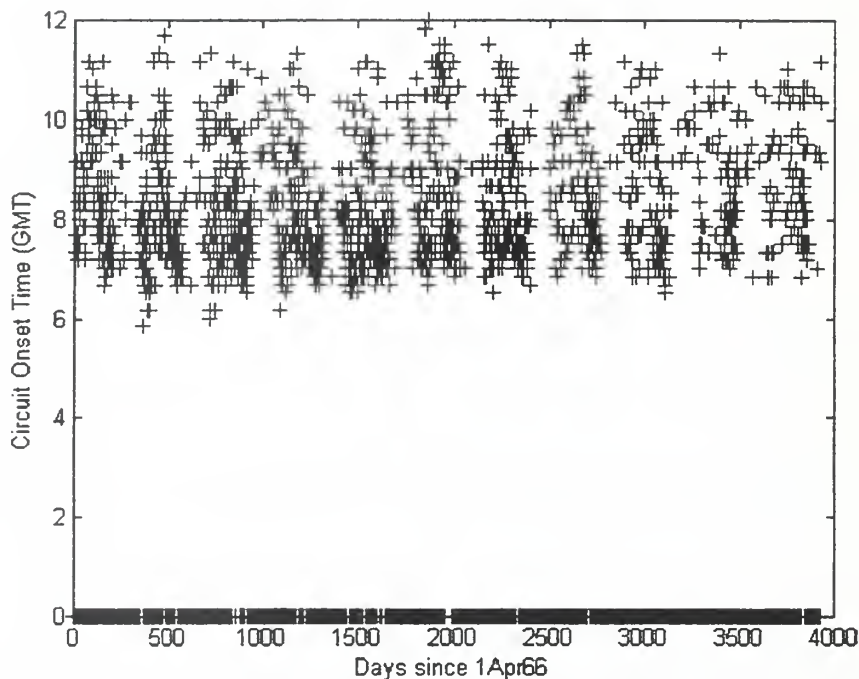


Figure 18. Circuit commencement times.

some form and regularity but are also characterized by randomness, as are all ionospherically influenced signals. The zero readings at the bottom of the graph show days on which the path did not materialize. The first step in the analysis of the circuit commencement signal is ascertaining correlation between path onset time and a physical parameter, i.e., determining if the path onset time is the dependent variable based on a physical parameter which is an independent value. One candidate independent variable is daily solar flux values for each day in the figure. Those solar flux readings are shown in Figure 19.

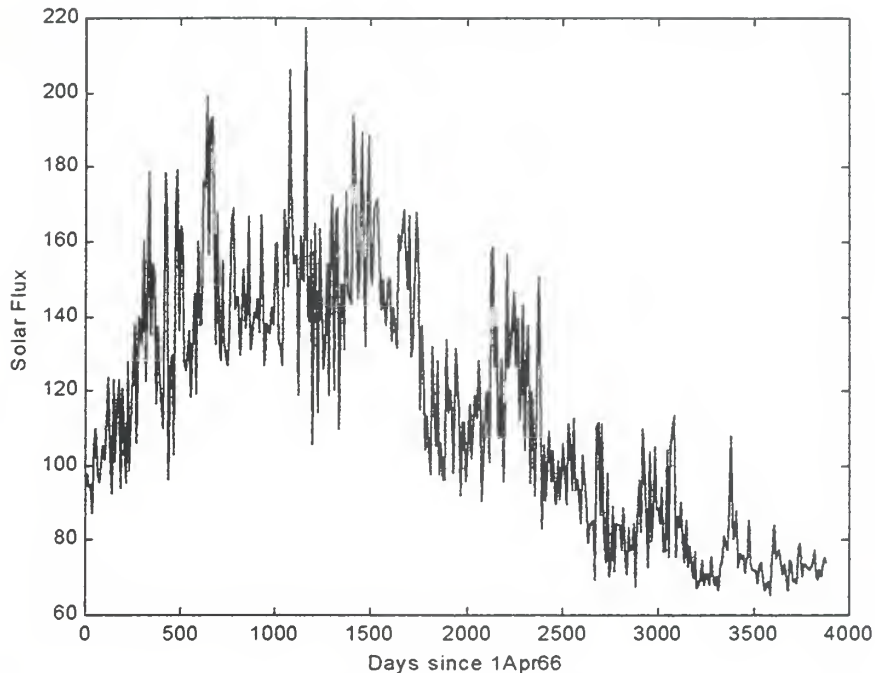


Figure 19. Solar flux.

An effective method of determining correlation between path commencement times of Figure 18 and the solar flux of Figure 19 is to compute the cross correlation between the two. The cross correlation between the path onset time and the solar flux is shown Figure 20. Notice that there is a good correlation of about 0.65. This correlation is strong enough to establish solar flux as a reliable partial predictor of path onset time.

A second candidate as an independent variable controlling onset time of the circuit is the solar zenith angle, or more specifically the cosine of the solar zenith angle. The cosine of the solar zenith angle for the same days as above is plotted in Figure 21.

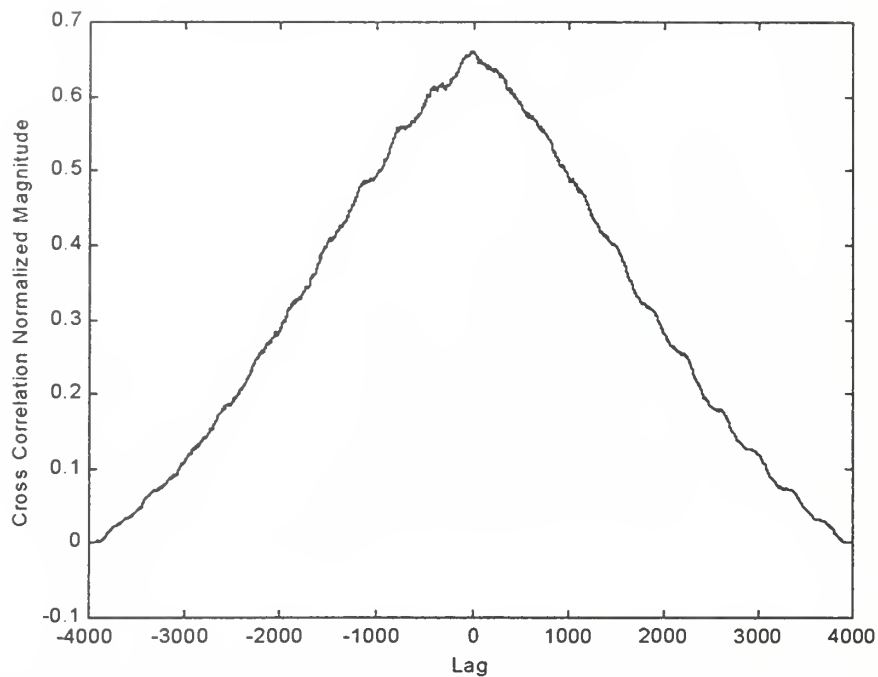


Figure 20. Normalized cross correlation of onset time and solar flux.

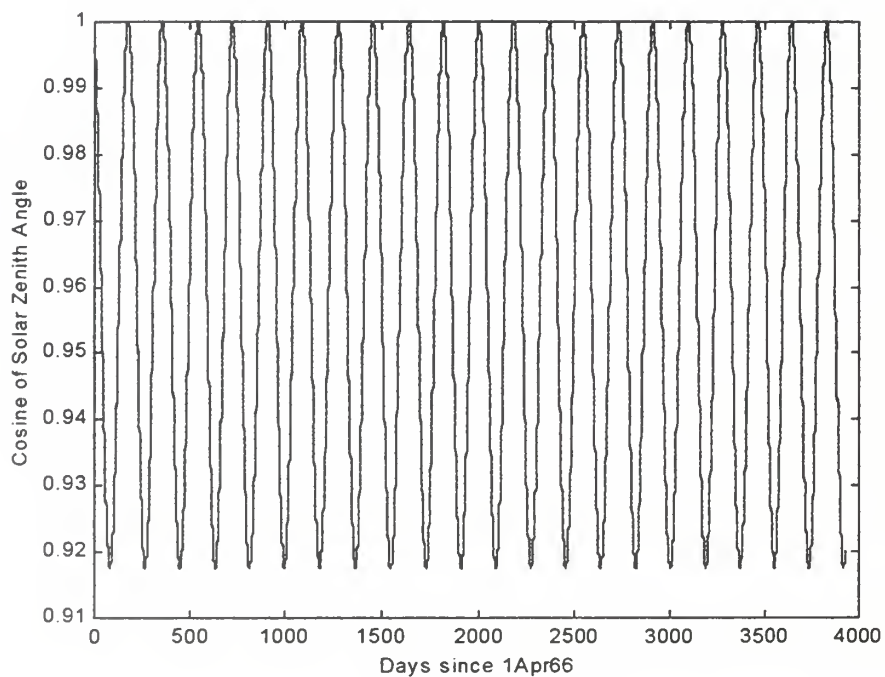


Figure 21. Cosine solar zenith angle.



The cross correlation function of the path onset time with the cosine of the solar zenith angle was computed and is shown in Figure 22. Again a correlation of about 0.65 is seen between the two signals. This also indicates a good candidate as an independent variable with partial control of circuit commencement time.

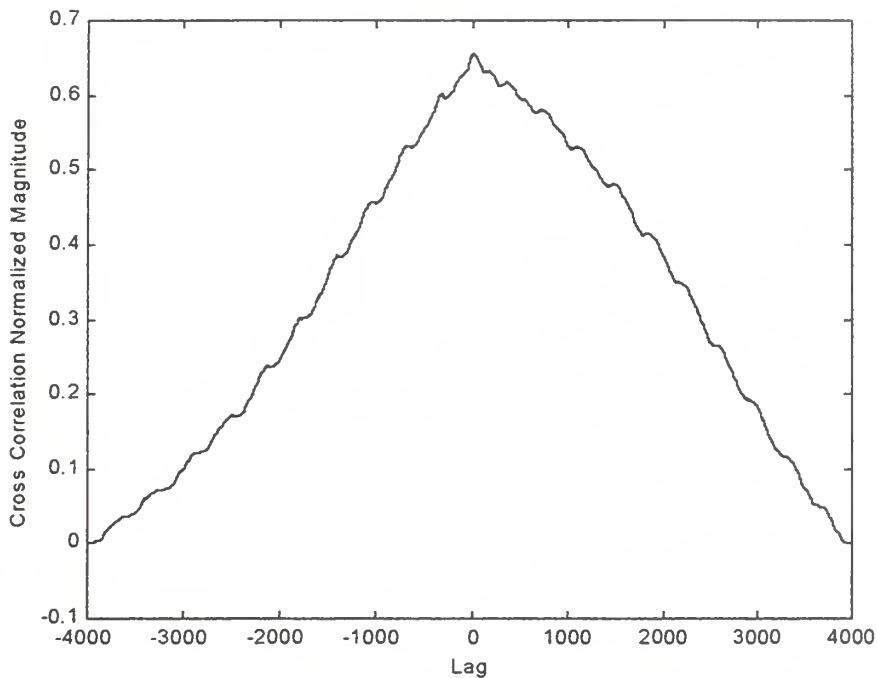


Figure 22. Normalized cross correlation of onset time and cosine solar zenith angle.

If days which have no propagation are removed from Figure 18, i.e., remove the zeros, the cross correlations between circuit onset times, given that the circuit exists, and the two independent variables can be computed. These are shown in Figures 23 and 24.

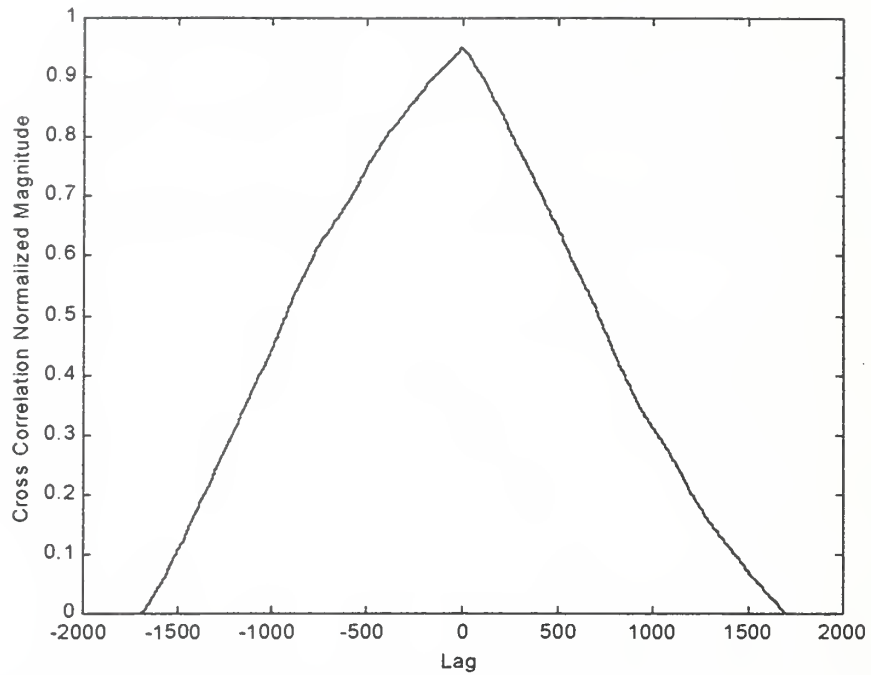


Figure 23. Normalized cross correlation of onset time and solar flux, given that circuit exists.

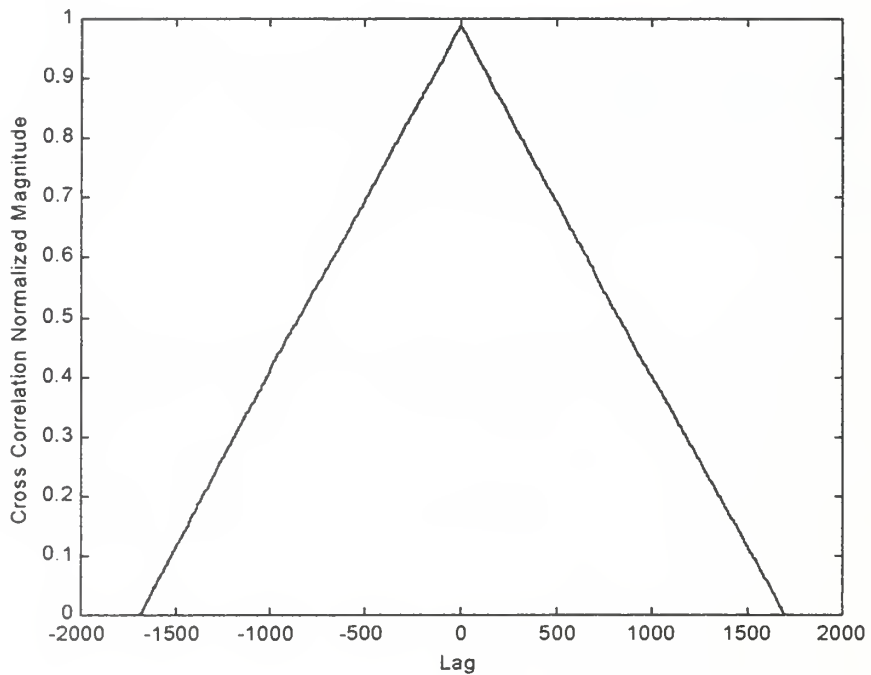


Figure 24. Normalized crossed correlation of onset time and cosine solar zenith angle, given that circuit exists.

In these two figures cross correlations have increased to above 0.95 indicating very strong correlations between circuit commencement time and each of the other two parameters. From this two things are learned:

(1) These two candidates are indeed responsible for at least part of the response of circuit onset time, and

(2) The zeros, i.e., days when there is no propagation, appear to be controlled by one or more other factors since the correlation factor increased with the removal of non-propagating days.

The signals on those days where propagation does occur were smoothed with low-pass filtering. Non-causal finite-impulse-response filtering of 50 delay elements was used to obtain filtered circuit onset time and solar flux. The cosine solar zenith angle was also filtered to remove the discontinuities resulting from removal of the non-propagating days. These filtered factors are shown in Figures 25, 26, and 27.

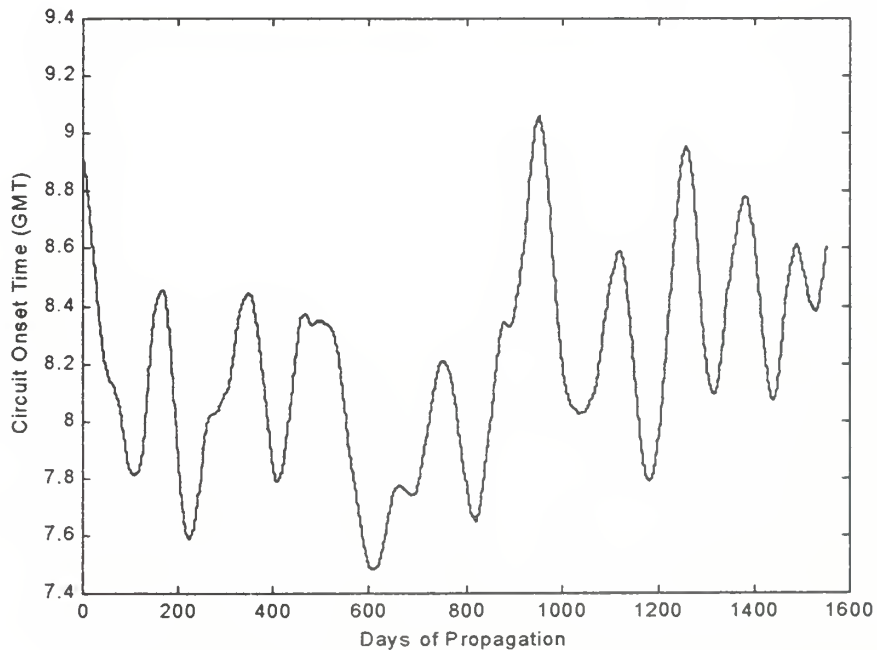


Figure 25. Filtered onset times.

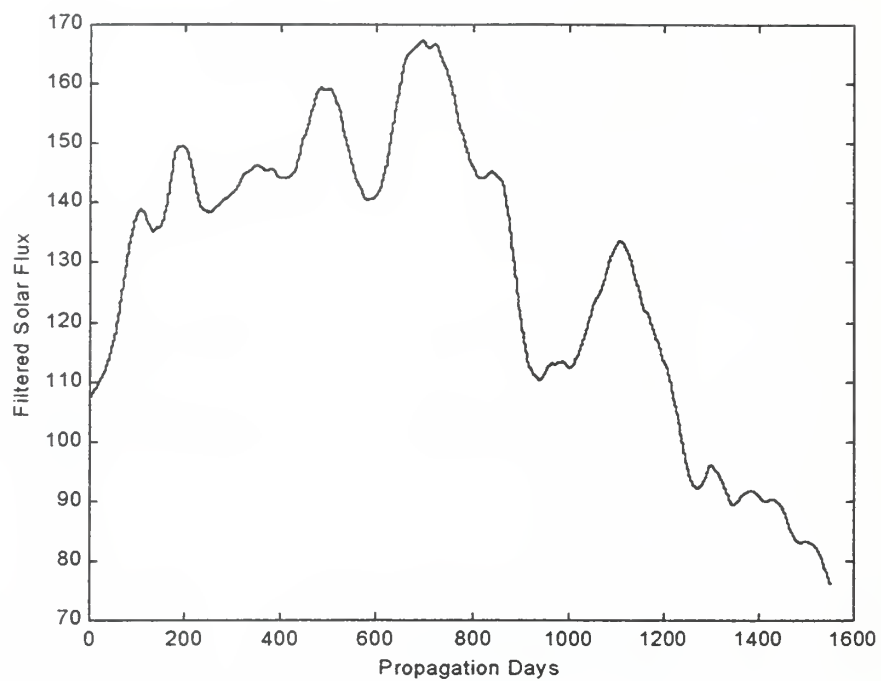


Figure 26. Filtered solar flux.

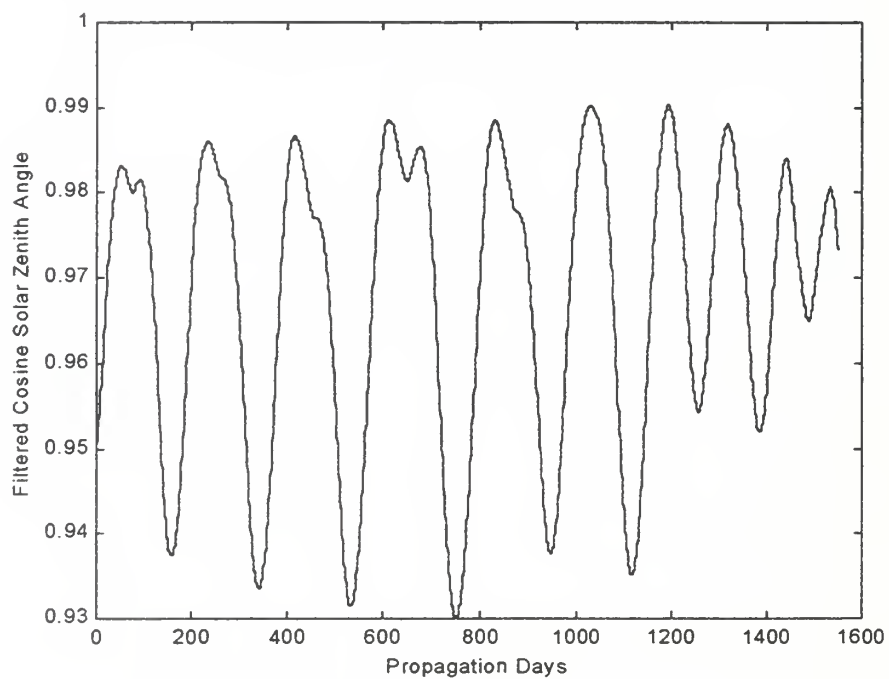


Figure 27. Filtered cosine solar zenith angle.

The filtered data, which emphasize the desired qualities and de-emphasize those which are undesired, are plotted against each other to see how they relate to one another. The dependence of circuit commencement time upon solar flux is obtained by plotting the filtered onset time against the filtered solar flux. The result is shown in Figure 28.

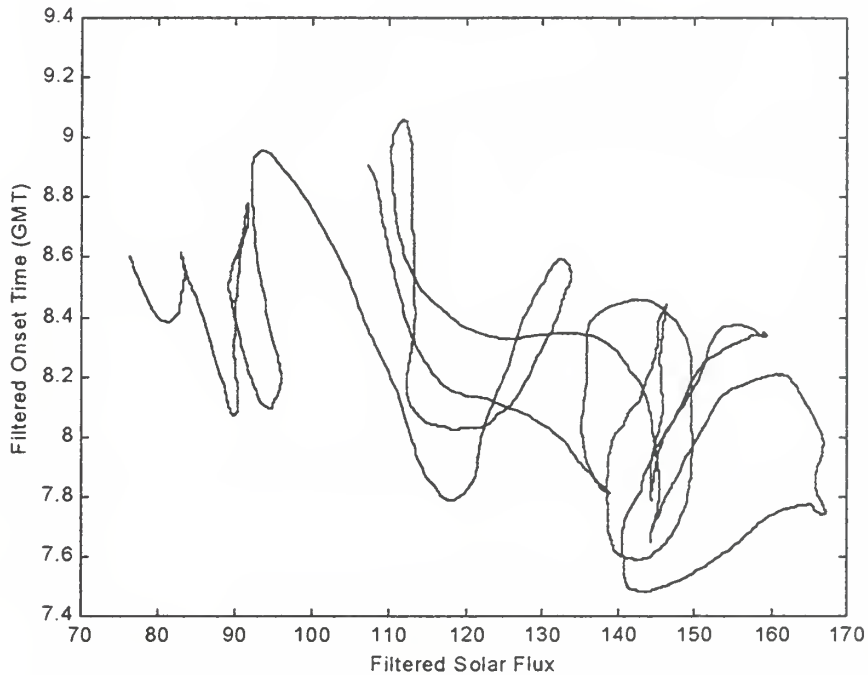


Figure 28. Filtered onset time versus filtered solar flux.

The relationship between the filtered onset time and the filtered flux appears to have an inverse relationship from Figure 28. This is also apparent by comparing the general waveform shape of Figures 25 and 26. A good fit, in the least squares sense, is obtained by the quadratic relationship

$$OT(f) = 0.0000181(fl_x)^2 - 0.0123(fl_x) + 9.46 \quad (GMT), \quad (34)$$

where  $OT(f)$  is the onset time response to  $fl_x$ , which is the 10.7 cm solar flux.

Similarly the filtered onset time can be plotted against the filtered cosine solar zenith angle. In Figure 29 the relationship between the two appears almost linear.

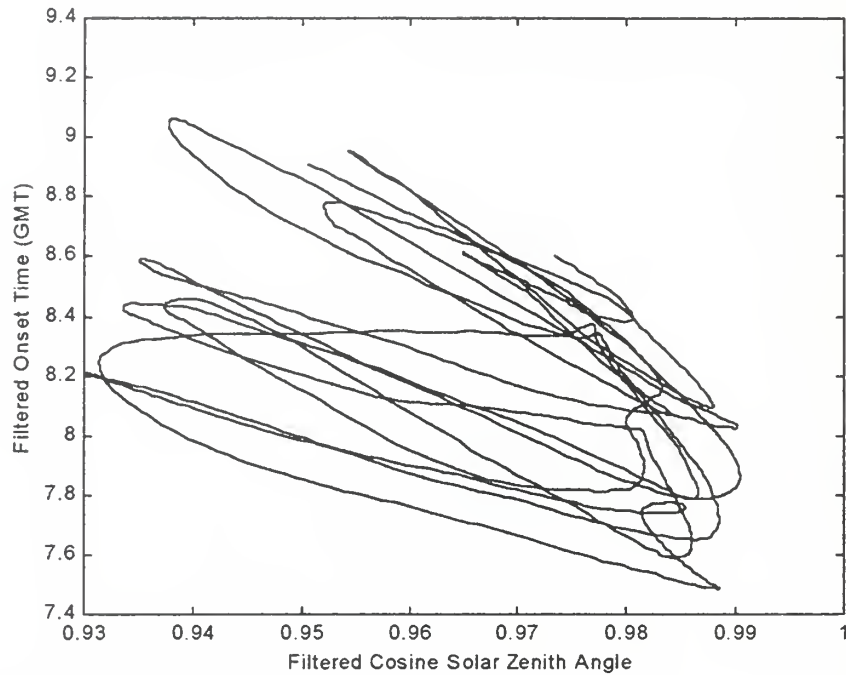


Figure 29. Filtered onset time versus filtered cosine solar zenith angle.

A good least squares fit is obtained by the linear relationship

$$OT(\chi) = 18.61 - 10.76(\cos(\chi)) \quad (GMT). \quad (35)$$

The individual contributions of both the zenith angle and the solar flux, and the interaction between them can be obtained by multiplying together Equations 34 and 35, i.e.,

$$OT(f\chi) = OT(f) * OT(\chi). \quad (36)$$



The results of the multiplication can then be least squares fitted to the filtered onset time to obtain

$$OT = 0.011 OT(f\chi)^2 - 1.334 OT(f\chi) + 48.06 \quad (GMT). \quad (37)$$

If this equation is a good fit to the observed onset times, plotting it against the data should yield a straight line at  $45^\circ$ . In Figure 30 the filtered onset time is plotted on the y axis and OT from Equation 37 is plotted on the x axis. Clearly, the prediction equation is valid since the plotted result approaches a  $45^\circ$  relationship in the least squares sense.

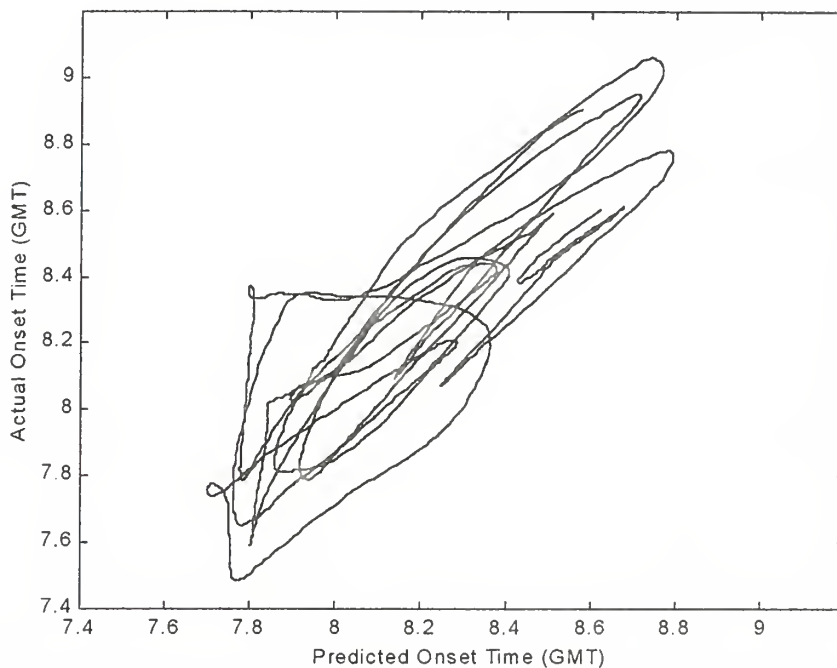


Figure 30. Actual onset time versus predicted onset time.

Filtered and predicted onset times are plotted together against the propagating days in Figure 31. There are a few deviations from the observations in

the predictions, but overall the data fit very well. The observed data are shown in blue and the predicted values in red.

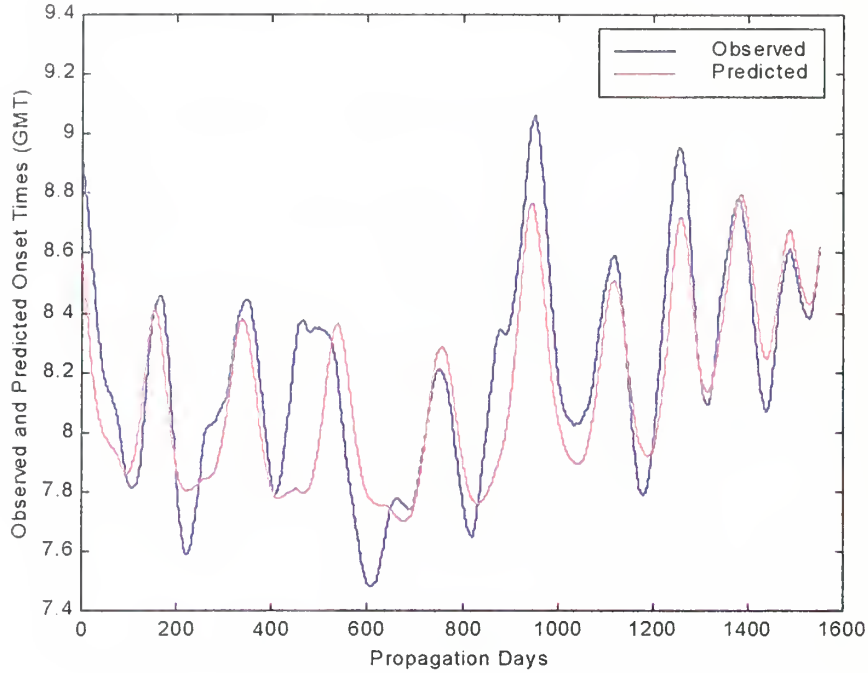


Figure 31. Observed and predicted onset times.

Although the analysis of circuit onset time has been conducted using GMT rather than local time for convenience, the onset time is actually a locally-controlled event. When predicted onset times are converted from GMT to local time,

$$Local\ Time = GMT + \frac{longitude}{15}. \quad (38)$$

For the equatorial-path crossing-longitude of this data set of  $201^\circ$ , the resulting local time is GMT + 13.4. With this adjustment Eq. 37 can be modified as

$$OT = 0.011\ OT(f\chi)^2 - 1.334\ OT(f\chi) + 61.46 \quad (local). \quad (39)$$

## B. CIRCUIT CESSATION TIME

The circuit filtered cessation times for the same continuous period from April 1966 to December 1976 are plotted in Figure 32.

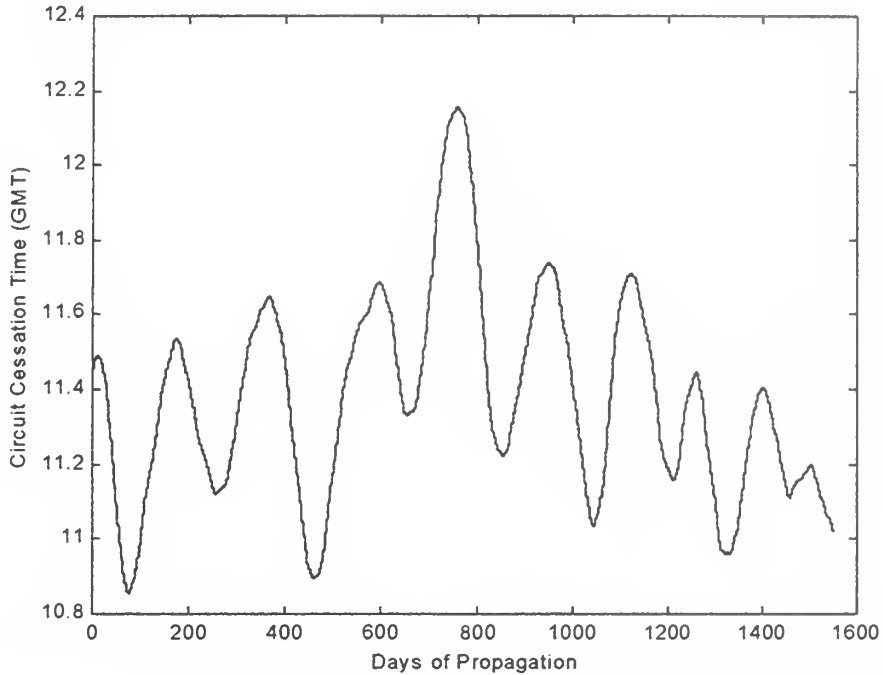


Figure 32. Filtered circuit cessation times.

The techniques used in the last section to predict circuit onset times are used to determine a prediction model for the circuit cessation times of Figure 32. Independent variables are found to be the 10.7 cm solar flux and the sine of the solar zenith angle. An exponential relationship is found which approximates the circuit cessation time as

$$CT = e^{\frac{flx + \sin(\chi) + 10}{100}} + 10 \quad (GMT). \quad (40)$$

A plot of the predicted value of the cessation time against the observed cessation time is expected to show a 45° angle. This plot is shown in Figure 33.

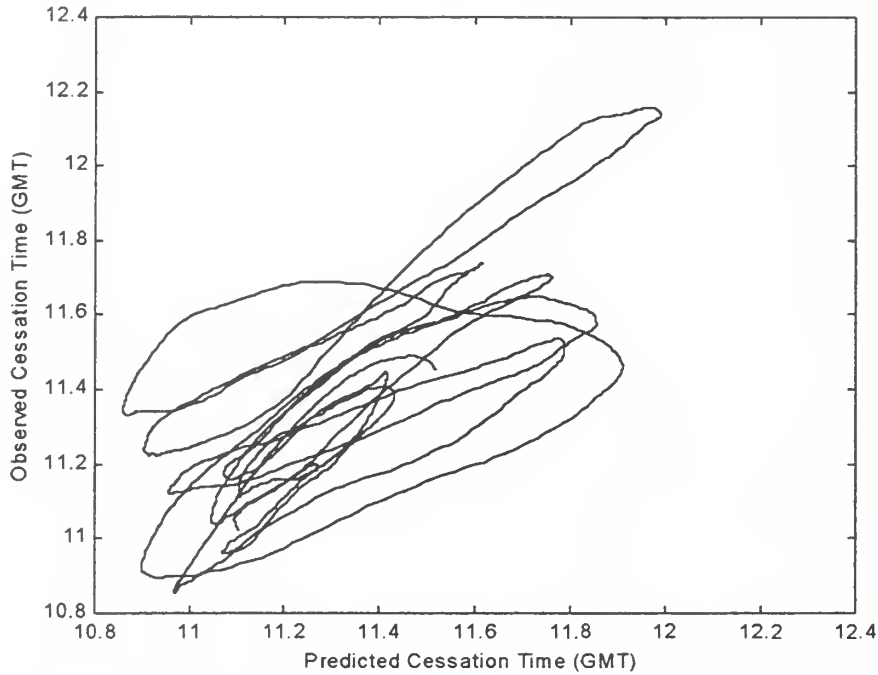


Figure 33. Observed versus predicted circuit cessation time.

In the least squares sense, there is a 45° relationship. A plot of the predicted and observed cessation times versus the days of propagation is shown in Figure 34, with the observed cessation time shown in blue and the predicted shown in red. There is a reasonable match between predicted and observed cessation times.

By using Eq. 38, Eq. 40 can be modified to localize it as

$$CT = e^{\frac{flx \cdot \sin(\chi) + 10}{100}} + 23.4 \quad (local). \quad (41)$$

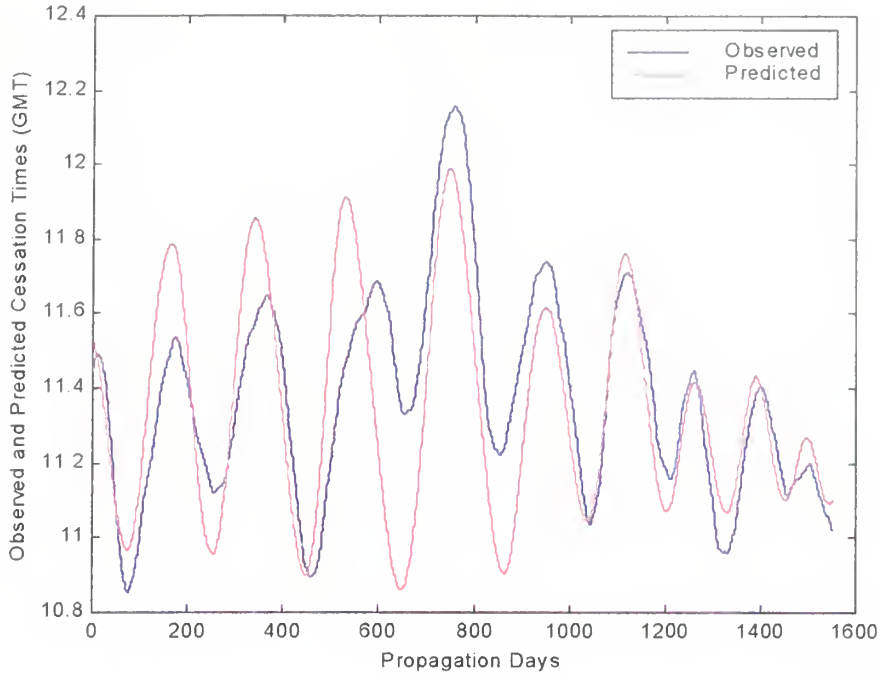


Figure 34. Comparison of observed and predicted cessation times.

### C. CIRCUIT PROBABILITY

With the ability to predict the starting and ending times of the propagation circuit for those days where the circuit exists now available, a measure of the probability that the path will actually exist is needed. The independent variables are again the relative position of the sun and the amount of ionizing energy available to create electrons for the anomalies and the ensuing propagation duct. In the previous two analyses the solar zenith angle was seen to be a controlling variable. In this analysis of the frequency of circuit occurrence, the probability function will depend more heavily on the position of the setting sun relative to the magnetic equator. This will be defined in this dissertation as the solar magnetic angle or SMA. A method to compute the SMA is given in Appendix C.

The specific times of occurrence, for example as shown in Figure 18, are not required to determine if a circuit exists or not. Instead all the starting times of Figure 18 can be converted to ones, i.e., the existence of a path equates to a one and the nonexistence of a path remains at zero. Groups of sequential ones will then indicate a higher probability of occurrence than a single one or a zero. If the data are non-causal filtered to provide moving averages of the number of sequential ones, the result is a moving probability function. To obtain a finer scale than when looking for trends as in the previous analyses, only twenty delay elements are used. Figure 35 shows the result of converting the data of Figure 18 to ones and zeros and the non-causal filtering.

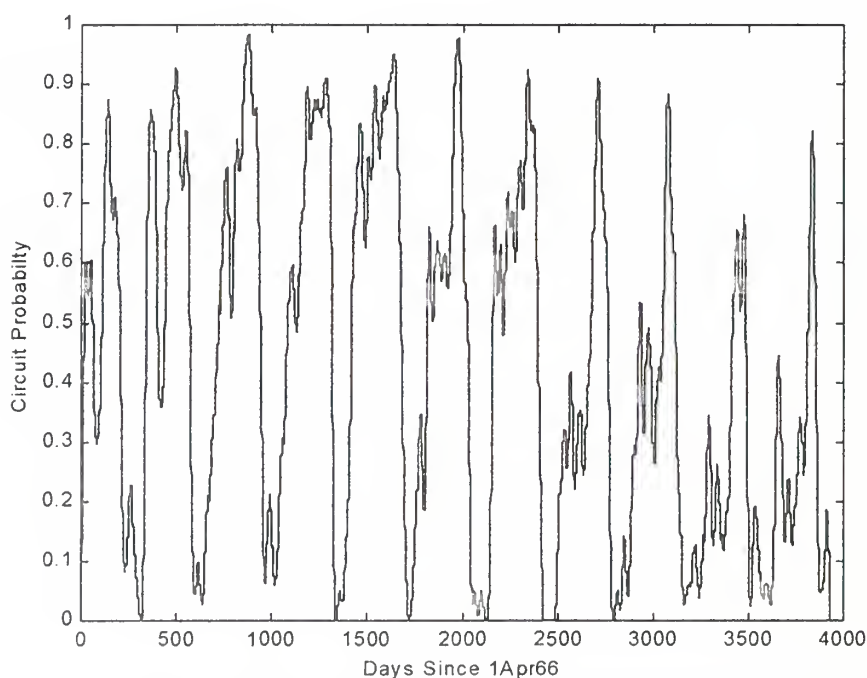


Figure 35. Twenty-one day moving average TEP circuit probability.



With knowledge that the circuit has the highest probability of occurrence when the SMA is near zero, i.e., when the sun sets on the magnetic equator, an overlaid normalized plot of the cosine of the SMA, scaled to the range 0 – 1, and the 21-day moving average circuit probability, is produced as shown in Figure 36.

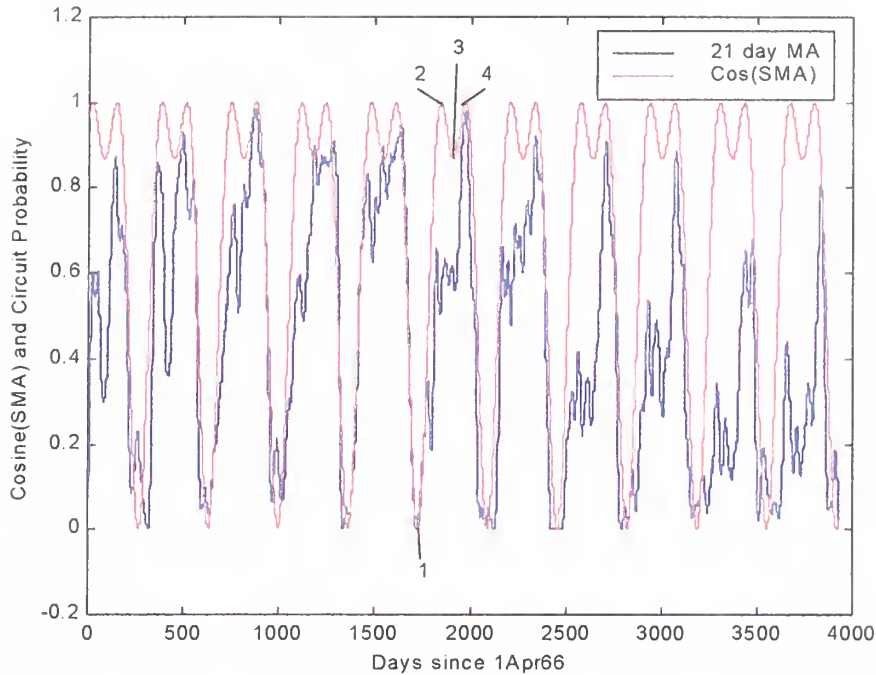


Figure 36. Comparison of 21-day moving average circuit probability and  $\cos(\text{SMA})$ . Indexes on plot indicate SMA positions: 1) Winter solstice, 2) Solar south-to-north magnetic equator crossing, 3) Summer Solstice, and 4) Solar north-to-south magnetic equator crossing.

The  $\cos(\text{SMA})$  (in red) is in phase with the fluctuations of the amplitude of the probability plot (in blue). These magnitudes are not identical, indicating that there are other controlling variables. The overall shape of the probability plot is similar to that of the solar flux over the same period, from Figure 19. A good fit to the envelope is formed as a function of the solar flux as

$$Envelope = \frac{flux}{480} + 0.6. \quad (42)$$

If the envelope is multiplied by the cosine of the SMA shown in red in Figure 36, a better fit to the circuit probability shown in blue is obtained. The result of this multiplication is shown in Figure 37 with the frequency of occurrence signal again shown in blue and the modeled signal shown in red.

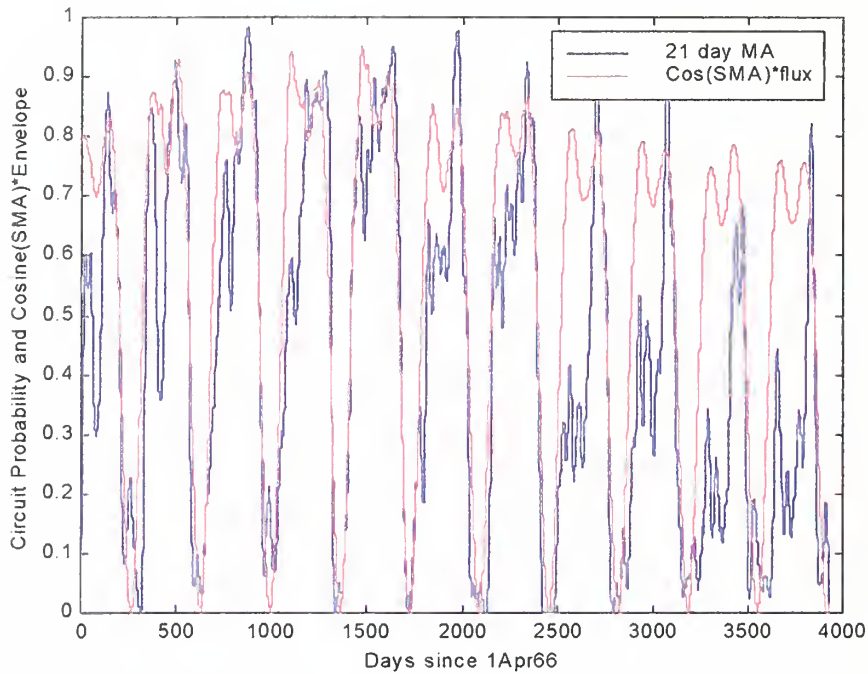


Figure 37. 21-day moving average circuit probability and cos(SMA) multiplied by solar flux envelope.

Although this model approaches the actual probability, another controlling variable must be accounted for. Each cycle of the cosine of the SMA has two peaks, and the probability plot similarly has two peaks which are in phase with the cos(SMA) peaks. The first peak of the probability shown in blue is much lower than

the second peak. This may be due to the delay in “charging” the local nighttime ionosphere. Similar to a capacitor where the voltage lags the applied current, the number of free electrons in the nighttime ionosphere is dependent upon the number of free electrons during the last night and the night before. Even though the sun is directly overhead during the day, there are not as many free electrons when the sun approaches from the opposite hemisphere as when it approaches from the same hemisphere. Since the data set has an  $11^\circ$  magnetic declination angle, the sunset side of the magnetic equator makes an angle of  $11^\circ$  north of the geographic equator. When the sun passes the magnetic equator heading north [the first peak in the cosine(SMA)], there are relatively few free electrons in the local nighttime ionosphere. The sun completes its journey to the north then returns toward the magnetic equator [indicated by the second peak of the cosine(SMA)]. The difference is that the sun has remained in the northern magnetic hemisphere between the peaks, allowing the nighttime ionosphere to become more ionized.

This difference in relative sun position can be accounted for by simply integrating the cosine(SMA) over several past solar magnetic angles, adding that value to the current SMA, and normalizing to keep the value between 0 and 1. A good fit is found by integrating over 150 days. The result of this integration is in Figure 38 which shows the complete modeling of the circuit probability with the observed frequency, in blue, and the predicted probability in red.

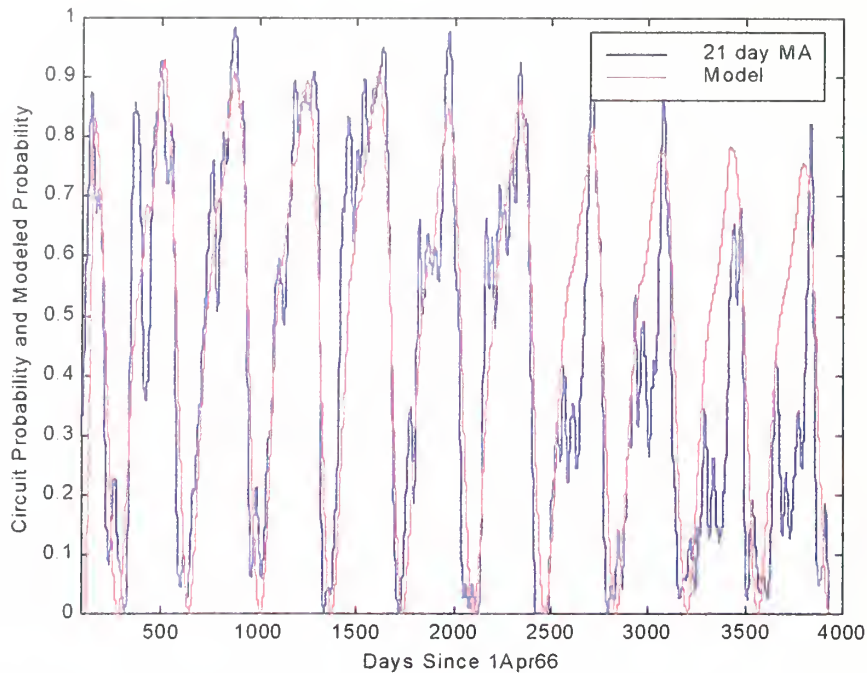


Figure 38. Probability of path occurrence. 21-day moving average circuit probability shown in blue and prediction model shown in red.

Local maxima in the circuit probability plot occur when  $\cos(\text{SMA})$  is zero, i.e., when the sun sets on the magnetic equator. This is because the probability of symmetric anomaly formation is greatest when solar energy irradiates both magnetic hemispheres equally. The magnetic hemispheres receive equal solar energy when the sun sets on the magnetic equator.

Local circuit probability minima occur at the solstices. As the setting sun is furthest from the magnetic equator at these points, asymmetric anomaly formation has greater probability. Since the solar position at the winter solstice is further from the magnetic equator than at the summer solstice, the anomaly asymmetry is even more pronounced, resulting in a lower circuit probability.

Absolute symmetry between the anomalies is seldom, if ever, achieved. It appears that there may be a symmetry threshold, above which TEP forms and below which it does not. Symmetric formation is affected not only by solar energy, but also by atmospheric and ionospheric winds, which reposition plasma. Asymmetric anomaly formation may account for non-propagation days, whether the asymmetry is caused by solar position or winds.

#### D. PATH LOSS

##### 1. Free Space Path Loss

In line-of-sight link budget calculations, the path loss is defined as the inverse of the ratio of received power to transmitted power, i.e.,

$$L_p = \left( \frac{P_r}{P_t} \right)^{-1}. \quad (43)$$

The free space (or spreading) path loss is a function of the transmitted frequency and the range from the transmitter to the receiver,

$$L_p(\text{free space}) = \frac{(4\pi)^2 f^2 R^2}{c^2} = \frac{f^2 R^2}{5.7 \times 10^{14}}, \quad (44)$$

where  $f$  is in hertz and  $R$  is in meters.

The above equation is in absolute loss, whereas the path loss is normally expressed in decibels (dB). Converting both sides of Equation 44 to decibels,

$$L_{dB} \approx 32 + 20 \log(f) + 20 \log(R), \quad (45)$$

where  $f$  is in MHz and  $R$  is in kilometers.

## 2. Received Signal Strength

The signal power input to a receiver is a function of the transmitter power, the transmitter and receiver antenna gains, and the path loss. Depending on the scenario, there may or may not be control over power and gains. The control over propagation path for this experiment was the positioning of the receiver and the receiving antenna gain.

Because of the path variability, the received TEP signal strength is not constant nor consistent. The total TEP path losses were given in Chapter IV as the free space losses, the coupling losses, and the reflection losses. The free space losses can be modeled by assuming a statistical median distance from the radio terminals to the duct apertures. The reflection loss is not known but presumed to be very low. For modeling purposes it is assumed to have a value of 6 dB. As the radio terminal positions were fixed in this experiment, it was not possible to determine coupling losses resulting from latitudinal and longitudinal terminal variations. However, using the known optimum positions, and the range of latitudes and longitudes from those positions that allow TEP, coupling factors (inverse of coupling losses) can be modeled as follows:

- 1) At optimum positions assume a multiplicative coupling factor of unity
- 2) At and beyond the latitude- and longitude-TEP-limits assume a coupling factor of zero
- 3) Assume cosinusoidal roll-off at all points between 1) and 2).



If it is assumed that the distances from radio terminals to the duct apertures have a median value of 275 km, the free space losses can be computed using Eq. 45, giving total path loss as

$$\begin{aligned} L_T &= L_{FS} + L_C + L_R \approx (87 + 20 \log(f)) + L_C + 6 \\ &= 93 + 20 \log(f) + L_C \text{ dB.} \end{aligned} \quad (46)$$

The free space path loss increases with frequency. The upper limit of frequencies which will propagate via TEP ducting is not known. The highest frequency observed in this experiment, 200 MHz, is used as the upper limit of the TEP model. The normal minimum HF frequency of 2 MHz is used for the lower limit.

If both the transmitter and receiver are located at the optimum magnetic positions of  $18^\circ$  (one in the northern hemisphere, one in the southern) the coupling losses of Eq. 46 would be zero, but not at other latitudes. Since geomagnetic latitudes for TEP are restricted to  $14^\circ$  to  $26^\circ$ , latitude coupling factors are modeled as cosine functions, for reasons stated above. If the latitude is less than  $18^\circ$  the modeling equation for the coupling factor (CF) is

$$CF_{lat} = \cos \left( \frac{2\pi(lat-18)}{16} \right), \quad 14^\circ \leq lat \leq 18^\circ. \quad (47)$$

Similarly, if the latitude is greater than  $18^\circ$ , the equation for the coupling factor is

$$CF_{lat} = \cos \left( \frac{2\pi(lat-18)}{32} \right), \quad 18^\circ < lat \leq 26^\circ. \quad (48)$$

The latitude coupling factor is shown in Figure 39.

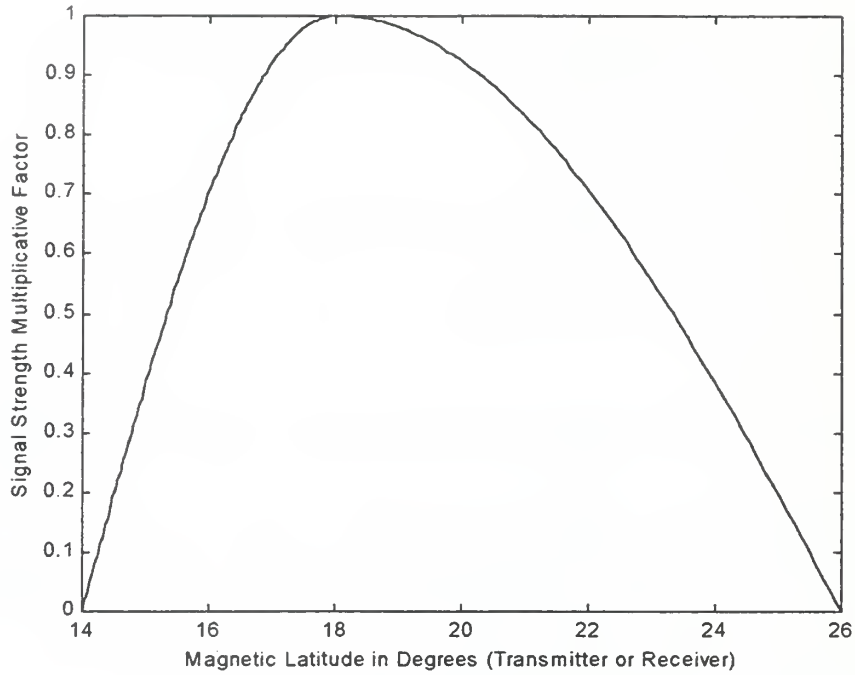


Figure 39. Latitude coupling factor.

Signal strength also drops when the receiver magnetic longitude differs from that of the transmitter. The longitude difference of this data set is  $6.5^\circ$  with substantial reception power, so a longitudinal limit of  $8^\circ$  is selected. When signal strength is modeled with a cosine function, to the limit of an  $8^\circ$  longitudinal difference, an optimal signal strength multiplicative factor equation is obtained as

$$CF_{long} = \cos \left( \frac{2\pi(long_{TX} - long_{RX})}{32} \right), \quad 0^\circ \leq |long_{TX} - long_{RX}| \leq 8^\circ. \quad (49)$$

This factor is shown in Figure 40. These two multiplicative coupling factors can be inverted, expressed in decibels, and combined as coupling loss of Equation 46 to get the total path loss.

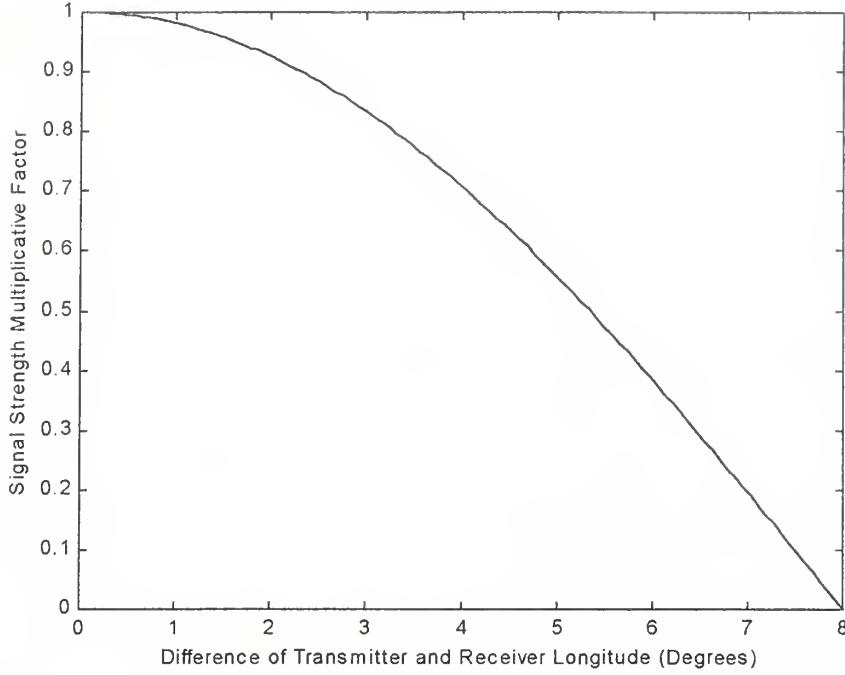


Figure 40. Longitudinal coupling factor.

Received signal strength variation with time is the last factor to be modeled. The data shows that signal strength starts from zero, builds as the duct passes to the east, then falls off, as shown for five days in Figure 41. Although not always true (e.g., densely versus sparsely separated ducts), signal strength varies sinusoidally with time. The coupling factor equation for time dependence is approximated as

$$CF_{time} = \sin \left( \frac{2\pi(t-T_o)}{2(T_c-T_o)} \right), \quad T_o \leq t \leq T_c, \quad (50)$$

where  $t$  is the time of interest,  $T_o$  is the circuit onset time, and  $T_c$  is the circuit cessation time. Figure 42 shows a plot of the time coupling factor with a circuit onset time of 1830 and a circuit cessation time of 2200. This multiplicative factor

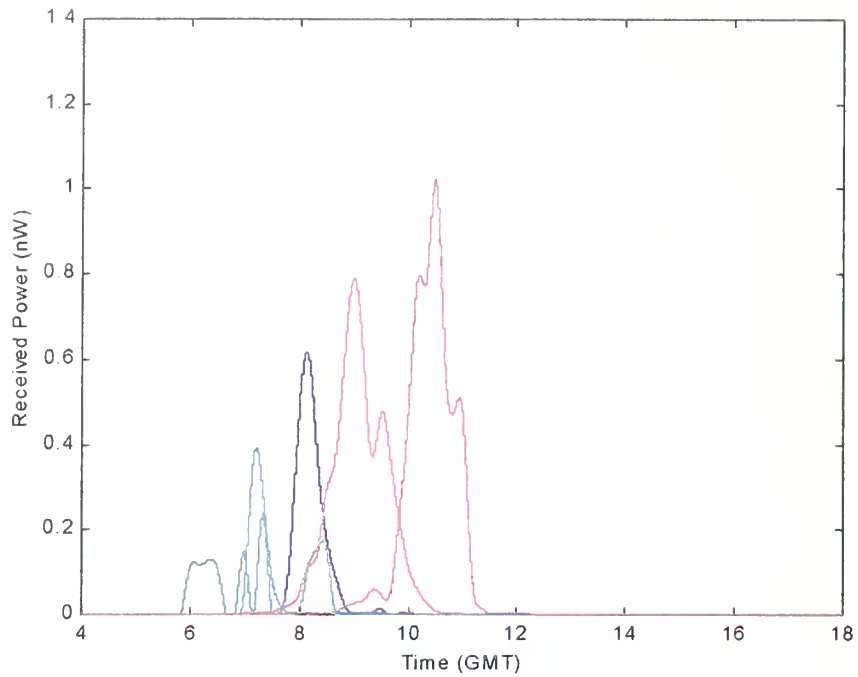


Figure 41. Signal strength roll-off with time over five days. Each day is represented by a different color.

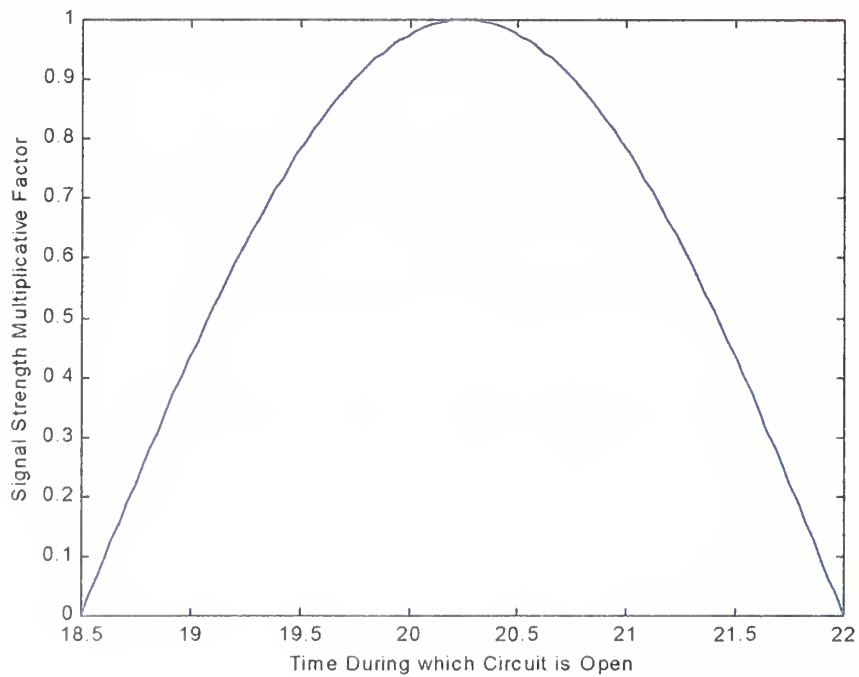


Figure 42. Time coupling factor for onset at 1830 and cessation at 2200 local.

can likewise be converted to decibels and added to the other coupling loss factors, completing the path loss model whose modeling equation is

$$L_T = 93 + 20 \log(f) - 10 \log(CF_{lat_{Tx}}) - 10 \log(CF_{lat_{Rx}}) - 10 \log(CF_{long}) - 10 \log(CF_{time}). \quad (51)$$

The prediction of received signal strength is found by subtracting the loss from the transmitted power expressed in decibels.

As validation of the path loss model, the TEP path values and Eq. 51 can be used to compute the expected value of peak reception power and compared with the average peak reception power measurements at Rarotonga. Using the ERP, magnetic latitudes and longitudes, and transmitted frequency of the VHF TEP path, the expected value of peak reception power is found to be 3.51 nW. The peak daily reception power values at Rarotonga during the experiment are shown in Figure 43. The mean peak reception power computed from the observations at Rarotonga shown in this Figure is 3.25 nW. Comparing this average value with the expected value predicted using Eq. 51 (3.51 nW) enhances the credibility of this model.

As an example of the different contributions to the path loss, consider an onset time of 1800, cessation time of 2200, transmitter location 15°N magnetic, receiver location 21°S magnetic, and the difference in longitude between the transmitter and receiver to be 4°. The total path loss is computed as

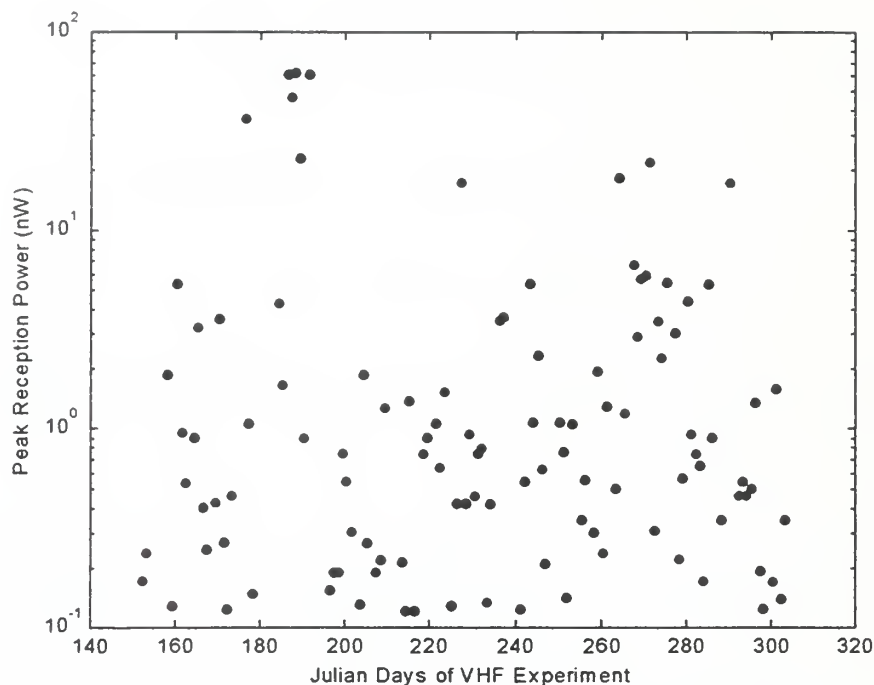


Figure 43. Peak daily reception power at Rarotonga.

$$\begin{aligned}
 L_T &= 93 + 20 \log(f) - 10 \log \left( \cos \left( \frac{3\pi}{8} \right) \right) - 10 \log \left( \cos \left( \frac{3\pi}{16} \right) \right) \\
 &\quad - 10 \log \left( \cos \left( \frac{\pi}{3} \right) \right) - 10 \log \left( \sin \left( \frac{\pi(t-18)}{4} \right) \right) \\
 &= 101 + 20 \log(f) - 10 \log \left( \sin \left( \frac{\pi(t-18)}{4} \right) \right) \text{ dB.}
 \end{aligned} \tag{52}$$

The result is graphed in Figure 44 for the duration of the circuit at frequencies from 2 to 200 MHz.

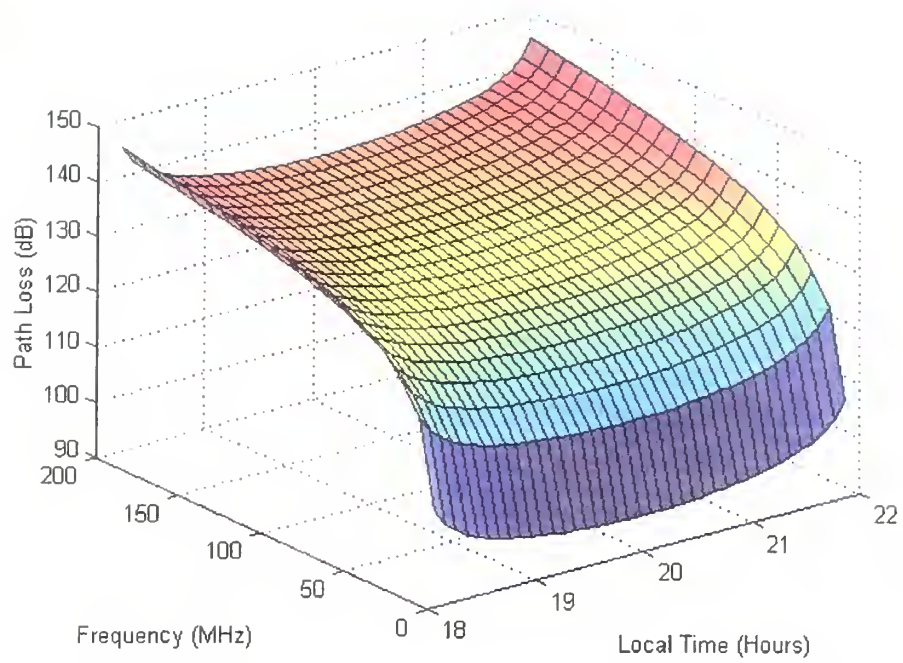


Figure 44. Path loss for example values.





## VII. THE TRANSIONOSPHERIC GPS EXPERIMENT

The data analyzed in this chapter are the GPS signal recordings collected in Rarotonga, Hawaii, and Christmas Island from March 1995 to October 1995. Correlations were made with the VHF reception data collected at Rarotonga over the same time period. The VHF data are a continuous monitoring of received signal strength from Honolulu and are considered to be the ground truth for purposes of this experiment. The GPS recordings are the derived total electron content (TEC) from all the visible GPS satellites at each site, and for the positions of those satellites.

Since the objective of this chapter is to identify and attempt to predict scintillation caused by the equatorial ionosphere, the VHF data must be used to help differentiate between a scintillating and a non-scintillating GPS signal. Geographically, Christmas Island is situated virtually beneath the midpoint of the propagation path from Hawaii to the Cook Islands. This spatial coincidence can be exploited by monitoring the GPS signal directly overhead Christmas Island during times of known VHF propagation and non-propagation to discern the difference between the scintillating and non-scintillating GPS signal.

### A. TEC OVERHEAD CHRISTMAS ISLAND

If the Christmas Island data set is filtered to exclude all but GPS signals arriving from satellites near directly overhead, these signals can be compared with VHF signals propagating overhead at the same time. If the presence of ionospheric ducts is identifiable by using GPS, this procedure should highlight their presence.

One such signal is that from GPS satellite 2 (commonly called a PRN) on Julian day 259 in 1995. The ground track of the signal from that satellite is shown in Figure 45

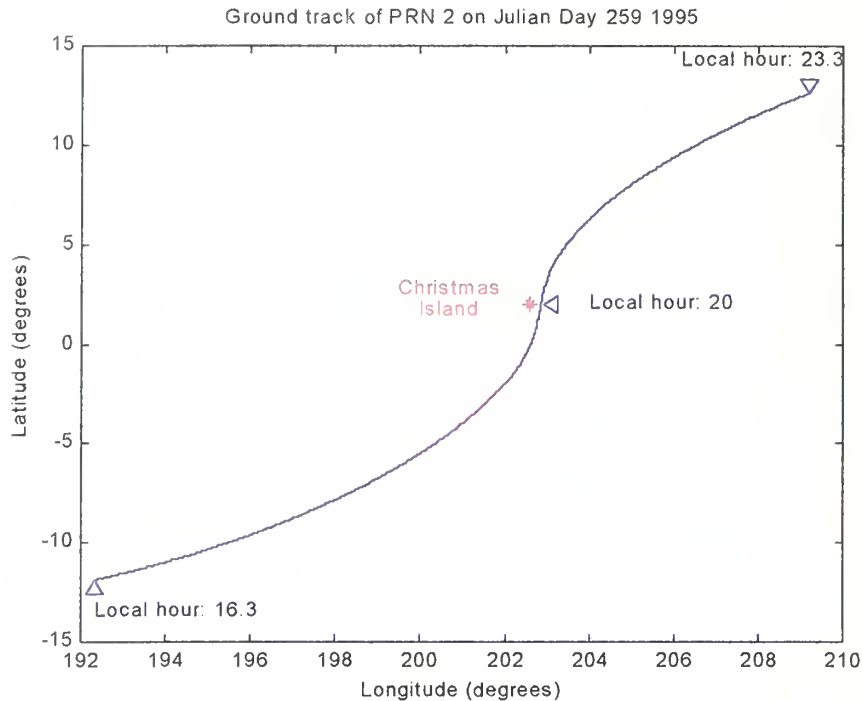


Figure 45. Ground track showing proximity of GPS satellite to Christmas Island.

where the satellite progresses south to north, crossing nearly overhead Christmas Island at 2000 local mean time (LMT). With sunset occurring at approximately 1800, this combination of satellite position and time provides an optimum positional relationship from which to observe the overhead TEC and the formation of an ionospheric duct.

On this particular day, the VHF signal from Hawaii to Rarotonga did propagate, beginning at approximately 2000 LMT. Recall that the presence of the VHF signal is indicative of the existence of a duct. In Figure 46, the TEC from PRN 2 (shown in blue) is plotted along with the signal strength of the VHF signal

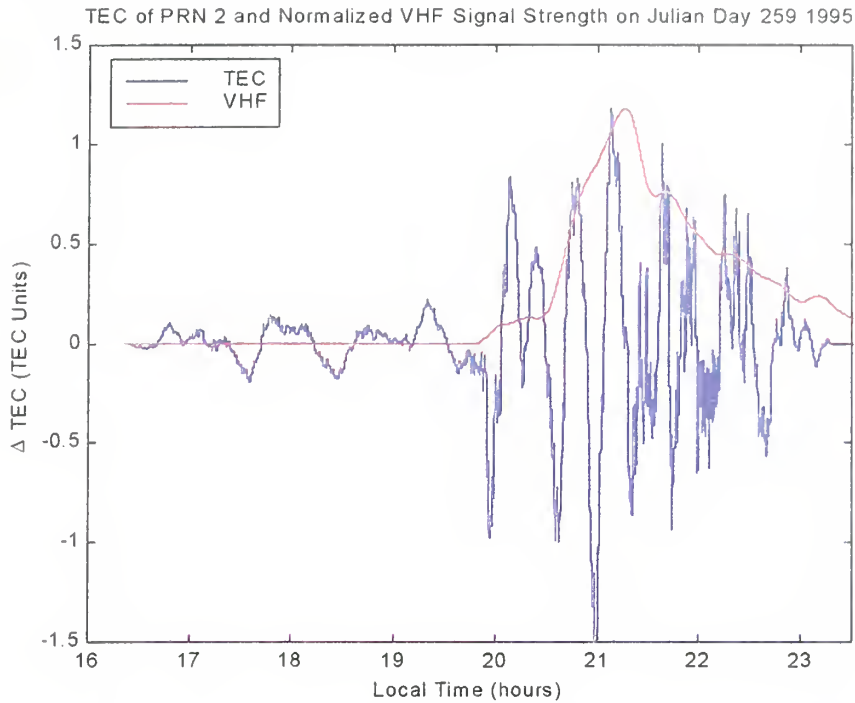


Figure 46.  $\Delta$ TEC overhead Christmas Island and normalized VHF signal strength at Rarotonga. One TEC unit is equal to  $10^{16}$  electrons/m<sup>2</sup>.

(normalized to the maximum TEC value) shown in red. Notice that the overhead crossing time of 2000 coincides with the onset of the VHF signal propagation, thus capturing the TEC response to the formation of an ionospheric duct. The TEC is seen to vary between approximately  $\pm 0.1$  TEC units prior to the onset of the VHF propagation. Just after the VHF signal begins, the TEC begins to vary between approximately  $\pm 1$  TEC units, an increase of 1000%. (As noted in Eq. 25, 1 TEC unit =  $10^{16}$  electrons/m<sup>2</sup>.) This behavior continues, diminishing as the VHF signal strength wanes until the satellite is out of field of view at approximately 2330.

It is apparent from the signals of Figure 46 that the TEC derived from the GPS signal is indicative of the presence of an ionospheric duct. If this were the sole occurrence of this type of TEC response however, little significance would be

attributed to it. Similar behavior is conspicuous throughout the data set as further evidenced by the signals shown in Figures 47 and 48. Figure 47 shows the ground track for PRN 2 on Julian Day 267. With the overhead crossing time of 1930 the formation of another duct can be recorded via GPS-TEC. This is illustrated in Figure 48 where the VHF signal is again seen to begin coincidentally with the satellite passing overhead the receiving station.

As a third example, a day is chosen on which there is VHF propagation but the

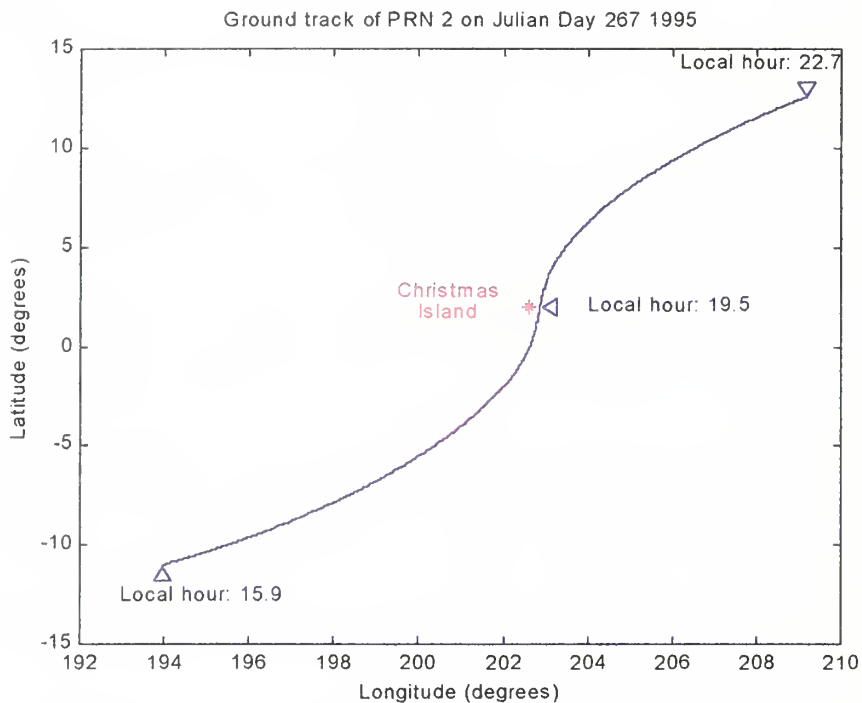


Figure 47. Ground track overhead Christmas Island on Day 267.

satellite overhead position does not coincide with the onset of the duct. On this day the satellite passes overhead at midnight, 2400. Figure 49 depicts the onset of the VHF signal at about 2230, at which time the initiation of the scintillating TEC signal

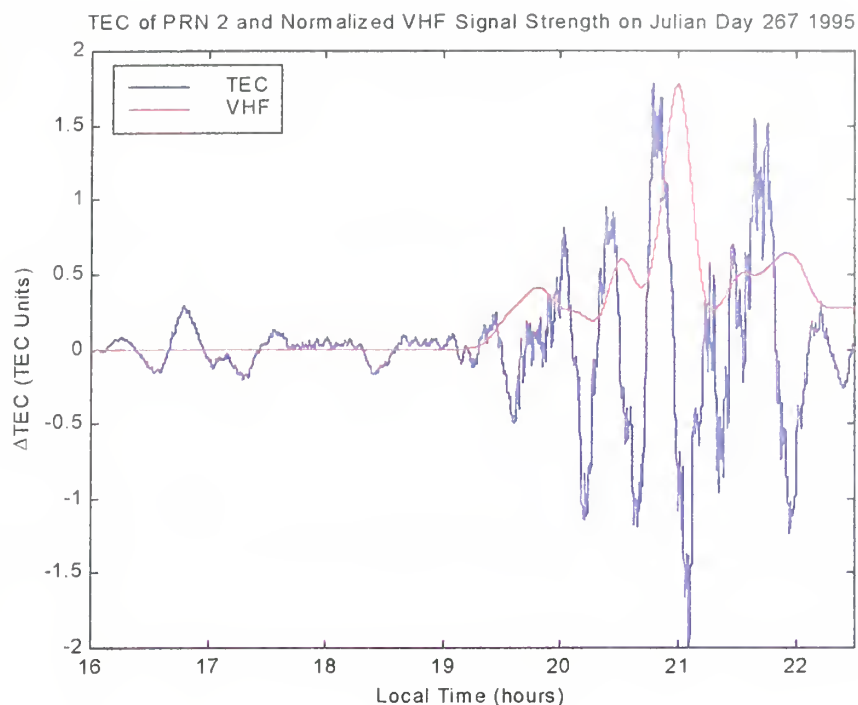


Figure 48.  $\Delta\text{TEC}$  and normalized VHF signal strength on day 267.

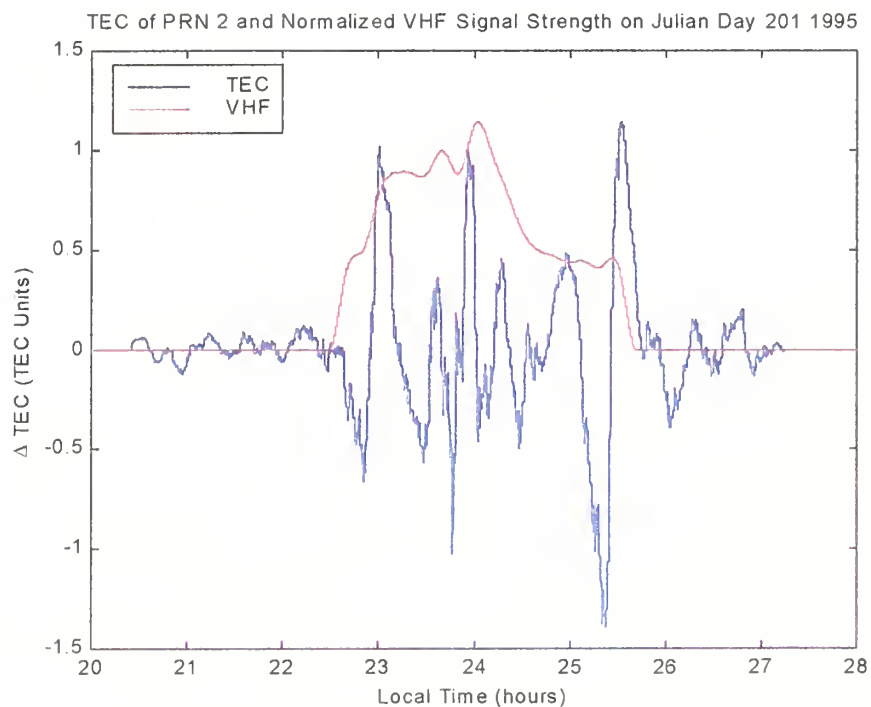


Figure 49.  $\Delta\text{TEC}$  and normalized VHF signal strength on day 201.

conforms. This behavior continues until the VHF signal ceases at about 0200 (shown as 2600 in the figure for plotting continuity), at which time the TEC scintillation diminishes.

For comparison to the days on which there is no VHF propagation, the day after the previous example is chosen. On this day no VHF signal was received in Rarotonga which suggests that no duct formed overhead Christmas Island. Again examining the TEC signal from PRN 2, just one day after observing the response from the same PRN in Figure 49, should yield telling significance to the identification of scintillating TEC. The TEC for Day 202 is shown in Figure 50. The time of satellite

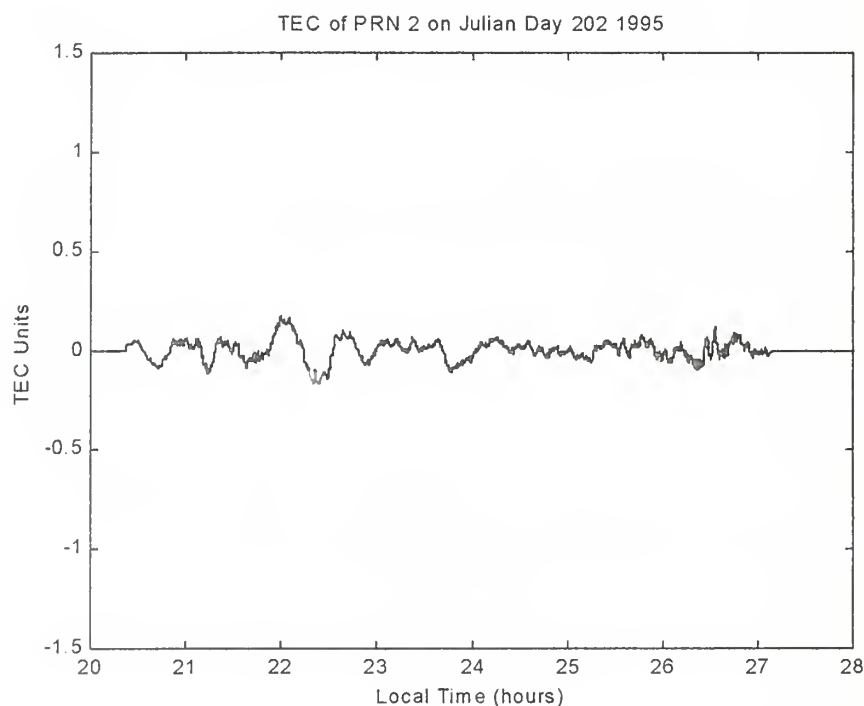


Figure 50.  $\Delta$ TEC for day 202. No VHF signal is present .

crossing overhead is again 2400. As seen in the figure, the amplitude of the TEC scintillation does not rise above the quiescent state of approximately  $\pm 0.1$  TEC units,



the apparent noise threshold of the data. Observation of the TEC in its dormant state, with no duct formation, is repeatable throughout the data set.

The TEC scintillations pictured in the previous plots have been transformed from slant to vertical reception angle. The details of this transformation will be demonstrated in Section E.

It is apparent from the foregoing analyses that TEC scintillation is readily observable using GPS signals. However, the methods used in this section to identify the times and locations of scintillation are unacceptably slow, tedious, and labor intensive. A procedure must be developed to more effortlessly identify the TEC scintillation.

## **B. FREQUENCY DOMAIN TEC SCINTILLATION ANALYSIS**

Transforming time series signals into the frequency domain for analysis is a natural technique since filters can be designed and used to eliminate or attenuate unwanted parts of the signal while enhancing the desired components. The initial step in analysis in the frequency domain is to identify those frequencies or frequency bands which are the desired aspects of the signal.

In the context of this analysis, it is desired to determine the differences between the frequency components of the quiescent TEC signals and those of the scintillated signals. An obvious way to compare the differences is to transform the signals from Figures 46, 48, and 49, i.e., the TEC on those days during which scintillation occurs. The time series can be divided into two parts: the parts with and without scintillation. Each part can then be transformed into the frequency domain,

normalized to a maximum amplitude of unity, and compared. It is anticipated that the transform of the scintillating part will have frequency domain components which are absent or attenuated in the non-scintillating part (or vice-versa). This procedure was employed and plots of the results are shown in Figure 51.

The figure consists of three plots, one for each of the analysis days, each of which contains the scintillated and non-scintillated spectra for that day. The scintillated data are shown in red and the non-scintillated data are in blue. Examining each plot, it is seen that there is no apparent difference between the scintillated and the non-scintillated data. This is true for any of the three days, and this result is found consistently throughout the data set. This finding can be explained by considering the source of the scintillation.

The TEC scintillation is caused by the ducts passing between the observer and the satellite. The ducts themselves consist of randomly sized tubes imbedded in their ceilings. Since the ducts and their constituents are all random in size and shape, their effects upon the signals passing through them will be somewhat random. The frequency spectra displayed in Figure 51 are manifestations of that randomness, and are themselves, somewhat random.

This analysis has shown that frequency domain techniques for analyzing, modeling, or identifying the scintillation data are inadequate. Since the data are randomly distributed, the obvious candidates for further analysis are statistical techniques.

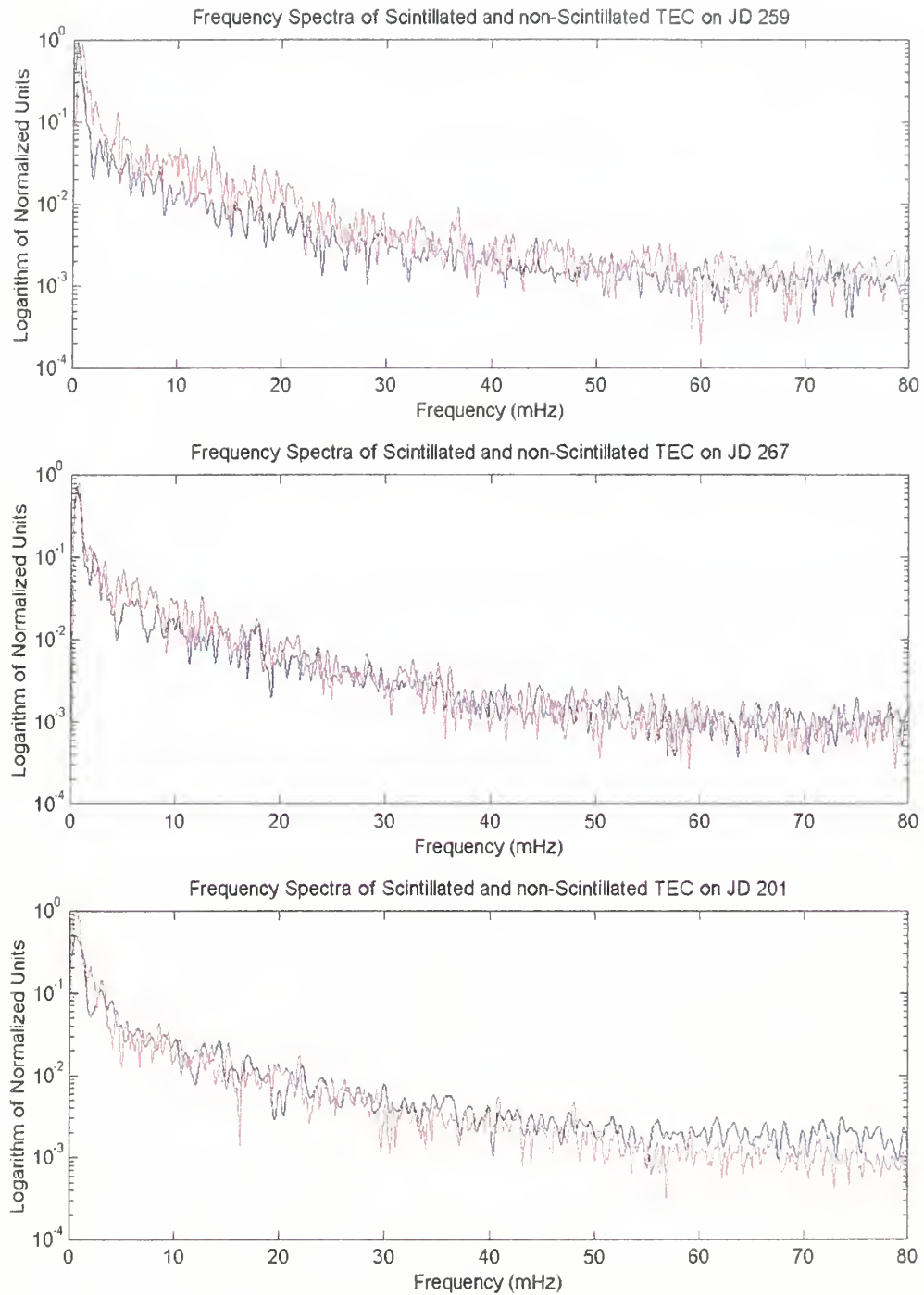


Figure 51. Frequency spectra for three days containing TEC scintillation. Scintillation spectra shown in red and non-scintillation spectra shown in blue

### C. STATISTICAL ANALYSIS OF TEC SCINTILLATION

Statistical techniques for time series analysis describe how the data vary from different perspectives. Usual descriptors are the various moments which can be computed from the data. Moments such as the mean and the variance can often differentiate one group of data from another. To help glean information as to the distribution of the data, the same days which were previously analyzed were divided into two groups, the scintillating and non-scintillating. Histograms were created of each to show their amplitude distributions. These histograms are shown in Figure 52.

The top plot shows the distribution of the non-scintillated data set while the bottom plot shows that of the scintillated. Both distributions show a quasi-normal

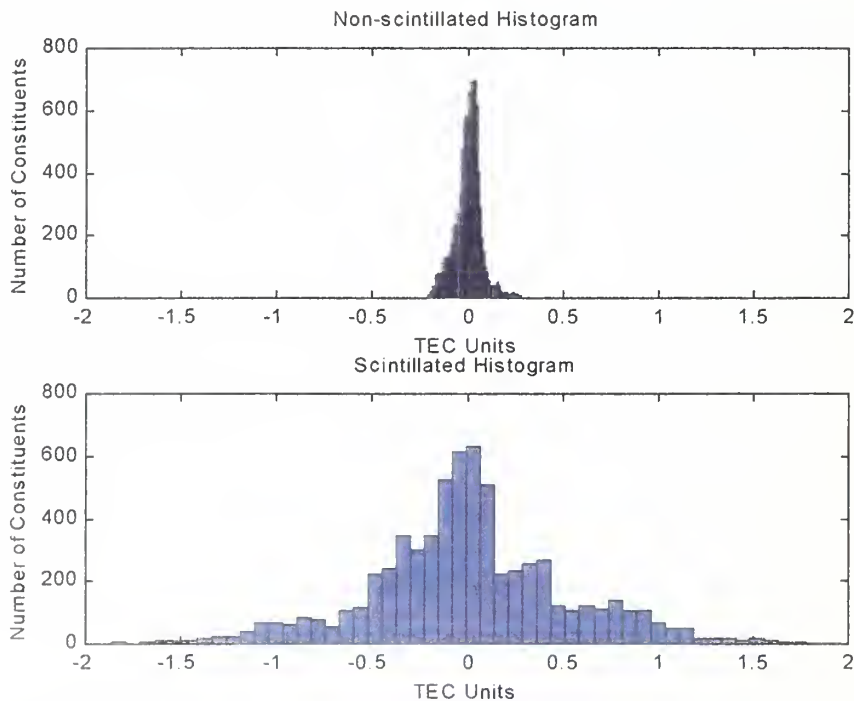


Figure 52. Histograms of the scintillated and non-scintillated data

distribution with a mean of zero. The prominent difference between the two is the spread of the data. The non-scintillated data are constricted between approximately  $\pm 0.25$  TEC units while the scintillated data extend to approximately  $\pm 1.75$  TEC units. From these observations it is concluded that by quantifying the spread of the data, a useful scintillation identification tool can be formulated.

Quantifying data spread is accomplished by computing the second and higher-order moments. But, since the data set is not stationary, a single computation of a higher-order moment of a TEC data record, such as those shown in Figures 46, 48, and 49, will be meaningless. Instead, it will be necessary to compute a “moving moment”, where a group of data is selected, the moment computed and stored, then the next group of data is selected, etc. In this manner a new data record can be generated which represents the moments of the data record with respect to time.

To visualize this procedure, the TEC data from Julian Day 201 (Figure 49) is subdivided into groups of one-half hour each. The 2<sup>nd</sup>, 3<sup>rd</sup>, and 4<sup>th</sup> central moments are computed for each half-hour block of data. The results are shown in Figure 53 where the 2<sup>nd</sup> order moment (variance) is shown in blue, the 3<sup>rd</sup> (skew) in green, and the 4<sup>th</sup> (kurtosis) in red. The 2<sup>nd</sup> and 4<sup>th</sup> order moments appear to be more illustrative than the 3<sup>rd</sup>, and the 2<sup>nd</sup> appears more robust than the 4<sup>th</sup>. Therefore, it is determined that the 2<sup>nd</sup> order central running moment is a reliable indicator of the presence of scintillation. The variance has units of TEC units squared. The standard deviation contains the same informational value as the variance, but its advantage is that the units are those of the original variable, i.e., TEC units. Therefore, the

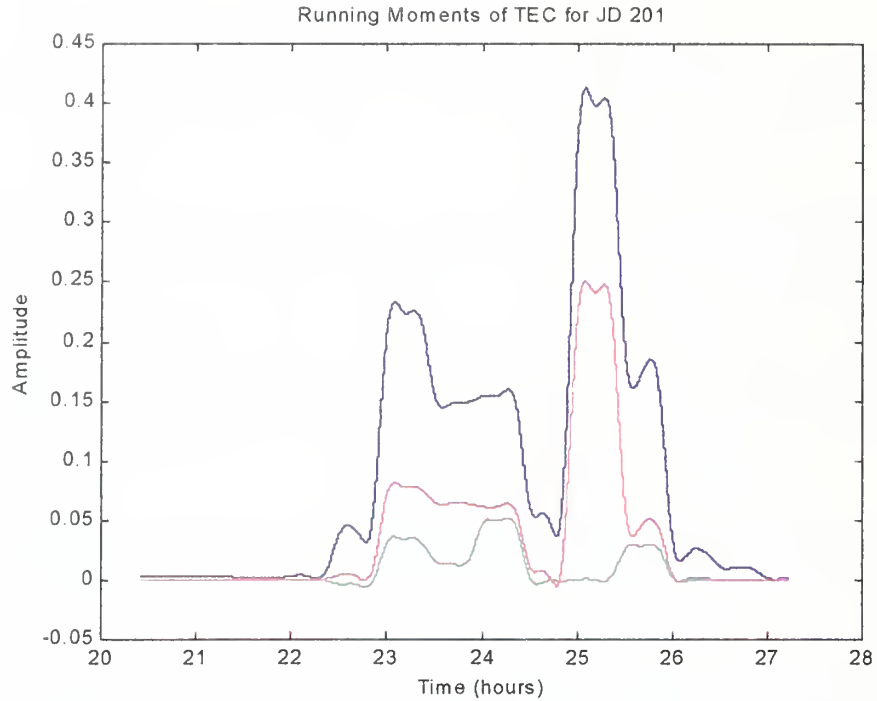


Figure 53. Variance (blue), Skew (green), and Kurtosis (red) of TEC

scintillation indicator used in this study will be the running standard deviation (RSD). For confirmation, the running standard deviation and the TEC from which it was computed are plotted together in Figure 54. The running standard deviation is seen to track the TEC scintillation. The value of 0.25 TEC units for the running standard deviation is subjectively chosen as being significant.

#### D. TIME-SPACE DISTRIBUTION OF TEC SCINTILLATION

The TEC data arrive at the receiver site from all the GPS satellites within the field of view of the receiving antenna. Thus, from one receiving site at any given time, the TEC scintillation at that time can be mapped full-circle around the site. This is achieved by tagging the received TEC to the satellite (and consequently the azimuth and elevation angle to it) from which it came. Estimating the height of the



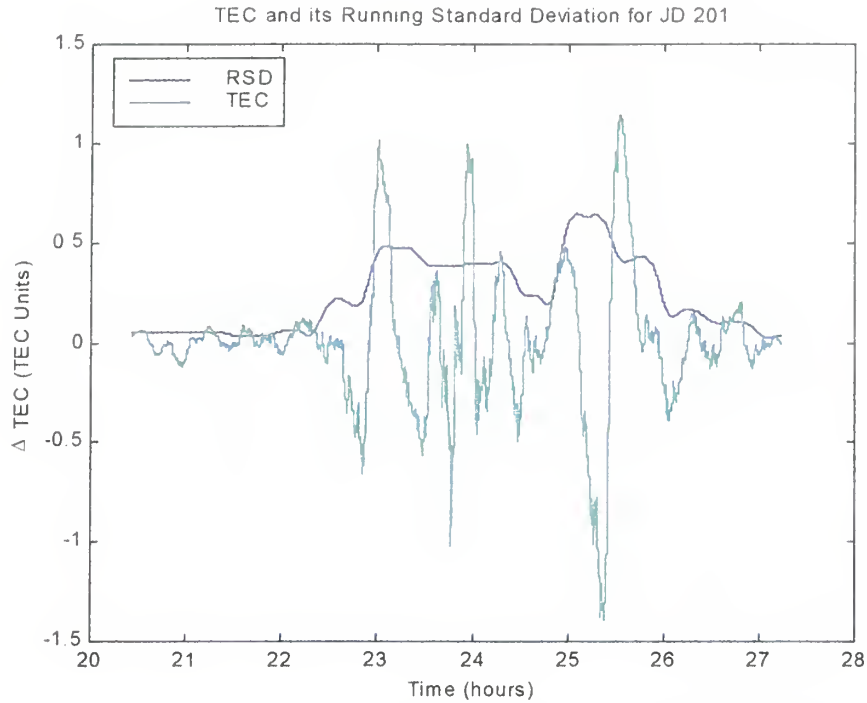


Figure 54. TEC variation shown in green with its running standard deviation shown in blue.

ionosphere at this azimuth and elevation, the TEC is mapped uniquely to a three-dimensional point in the surrounding sky. Appending the time stamp to the three-dimensional point, a time-space map of the TEC can be constructed. Each point is a five-dimensional vector: latitude, longitude, altitude, time, and TEC magnitude. For purposes of this study the altitude is used only to help determine the latitude and longitude. Once those are found, the altitude can be eliminated. But, the point still represents a four-dimensional vector.

There is no satisfactory stationary method to properly visualize a collection of points in four dimensions. For example, returning to Julian Day 201, the RSD can be computed for the two PRNs 2 and 4. Once found, the RSD can be plotted against the other three members of the vector one at a time, as shown in Fig. 55 against time



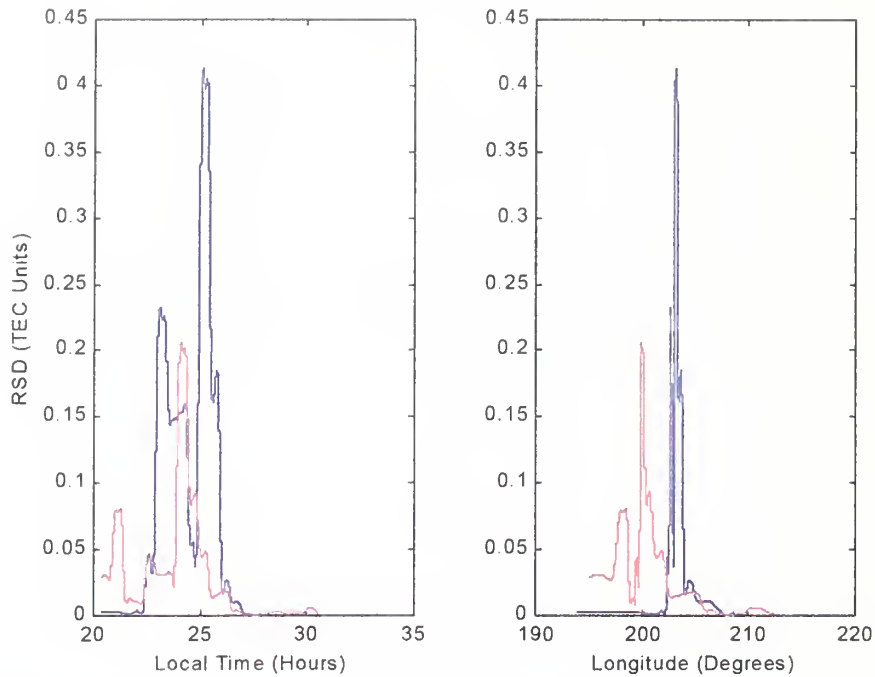
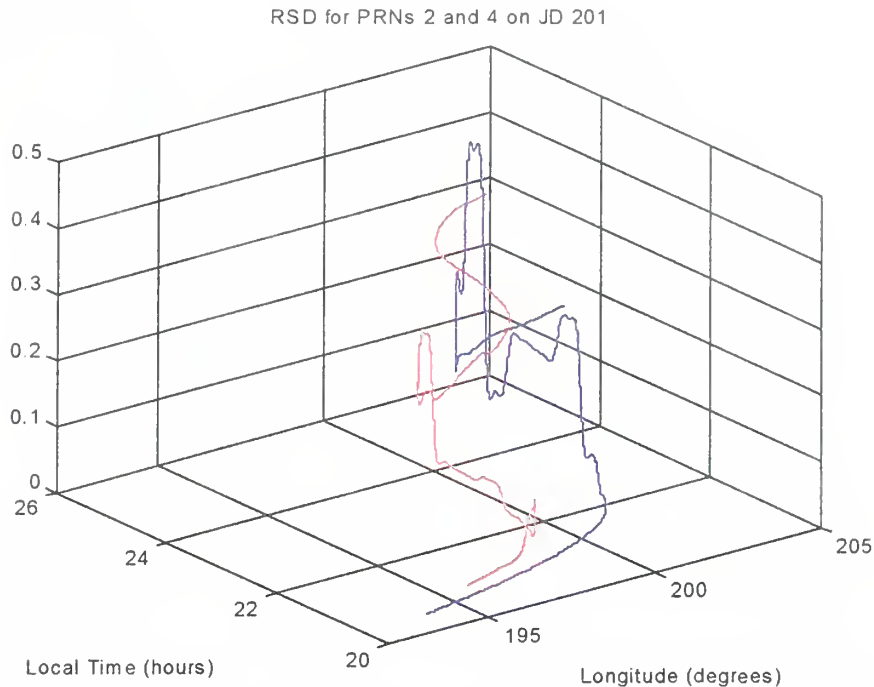


Figure 55. Running standard deviation for PRN 2 and PRN 4

on the left and longitude on the right with the RSD for PRN 2 shown in blue and for PRN 4 in red. While each plot displays useful information, neither shows enough alone or together to gain a situational awareness of the environment. The RSD can also be plotted in three dimensions, against two of the other three. The RSD plotted against time and longitude in three dimensions is shown in Figure 56. Again, PRN 2 is plotted in blue and PRN 4 in red. While this plot gives better perspective, the fourth dimension, latitude, is still missing.

In order to properly display the data so its behavior can be more easily understood, the vector dimension must be reduced from four to three. Upon examination of the members of the vector, latitude, longitude, time, and RSD, with the additional information that the scintillation is a post-sunset event, it is



**Figure 56.** Running standard deviation plotted in three dimensions

ascertained that time and longitude contain redundant information. If it is agreed that the parameter that is actually needed to describe the space-time relationship is time-after-sunset (TAS), then time and longitude can be combined to derive that parameter. This operation reduces the functional vector to three dimensions comprised of latitude, RSD, and TAS.

Before computing the TAS for each point in the data set, recall that the scintillation-producing ducts are aligned along the magnetic field lines (see Chapter II). The magnetic declination angle around Christmas Island is  $10.9^\circ$ . Therefore, the ducts are not aligned from true south to true north, but instead are rotated  $10.9^\circ$  clockwise. Suppose Christmas Island is receiving signals from two PRNs which have passed through an ionospheric duct as shown in Figure 57. There are two data

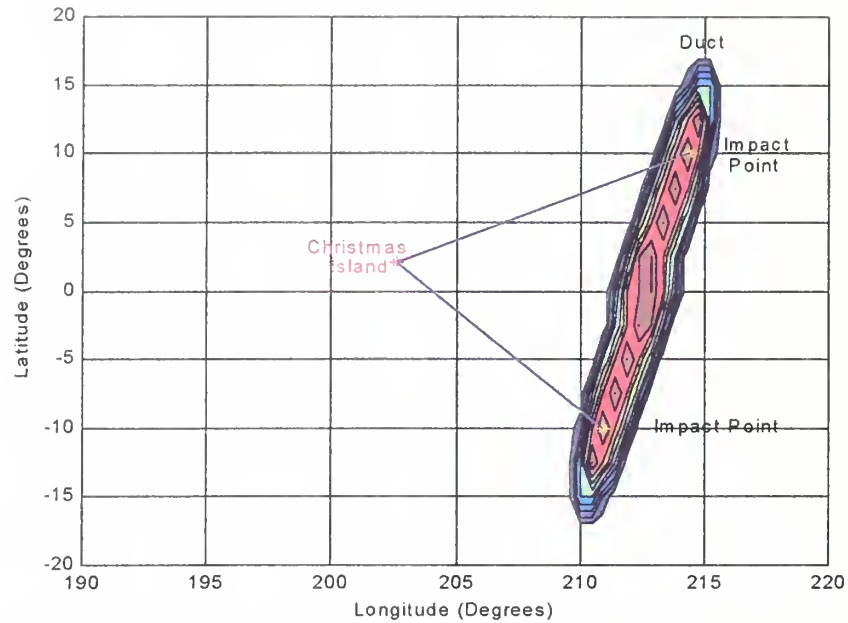


Figure 57. Two GPS signals passing through different parts of duct

points at which the latitude, longitude, and altitude are represented by the impact points. The two signals arrive after being influenced by the same scintillating event, one ionospheric duct. By resolving the positions of the scintillations, i.e., latitude, longitude, and altitude, one finds that the scintillating cause lies at similar positive and negative latitudes, but two separate longitudes are returned, 211 and 214 degrees. While this is correct geographically, it does not reveal that both observations are from the same event. If the geomagnetic coordinates are used instead of geographic, both signal observations are properly resolved to the same longitude.

With the data point positions transformed to geomagnetic coordinates, the duct shown in Figure 57 will appear as shown in Figure 58. Also shown in this figure is an arbitrarily positioned solar terminator. Computing the time-after-sunset, shows

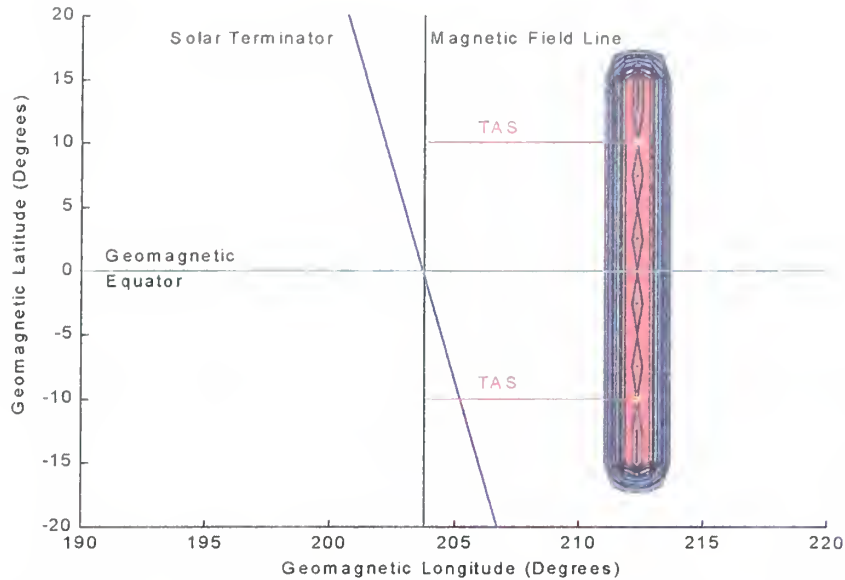


Figure 58. Duct in geomagnetic coordinates showing TAS

the time from the upper impact point to the solar terminator is greater than that from the lower impact point. Since both times are describing the same event, it is not desirable to have two separate times to describe the event. The only point on the solar terminator which is common to both is the time of sunset on the magnetic equator. Accordingly, it is this time from which the TAS is computed, as shown in the figure.

If all the satellite signals for an entire day are thus transformed, a time-space map can be drawn depicting the TEC scintillation as a function of magnetic latitude and time-after-sunset for that day. This transformation and mapping was performed for four days using Christmas Island data, Julian Days 187, 194, 200, and 202. Days 187 and 200 experienced VHF propagation while days 194 and 202 did not. The scintillation data were then averaged first across all latitudes and then across all times. These averages are plotted in Figure 59 where the latitude-averaged

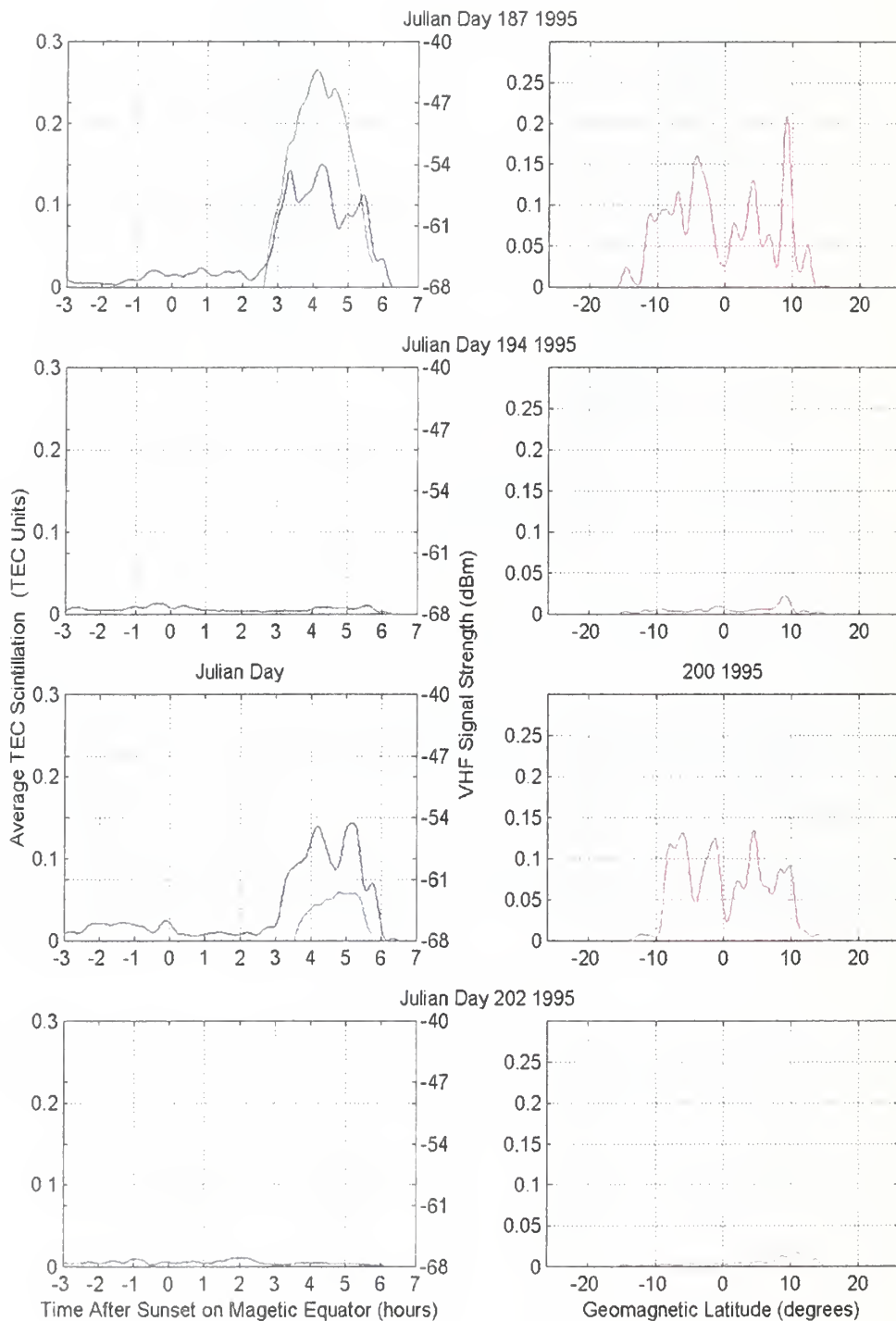


Figure 59. Time-space TEC scintillation around Christmas Island.

scintillation is shown on the left for each of the days and the time-averaged data on the right. Also on the left hand plots, the received signal strength, in dBm, is plotted in green (axis on right hand side of left hand plot). The VHF signal has also been transformed to time-after-sunset on the magnetic equator. On the two days with VHF propagation, significant scintillation coincides in time. Also, on the two days with no propagation, scintillation is not present. On the right hand side, the data averaged across time shows the scintillation distribution in latitude. Scintillation is again present on days of propagation and absent otherwise. The latitudinal distribution spans from about  $-12$  to  $12$  degrees. It is confined to these limits since only Christmas Island data is presented which limits the extent of the field of view of the receiving antenna.

Finally, to gain a more complete picture of the space-time distribution of scintillation, every GPS signal from every day can be transformed and plotted. Assuming that every scintillation event is mirrored in the opposite hemisphere, the data from the southern hemisphere can be folded on top of the northern hemisphere and vice-versa for visualization enhancement. Low-pass filtering in two dimensions provides smoothing. The results of transforming, folding, and filtering the scintillation data are shown in Figures 60 and 61. The top plot of Figure 60 shows scintillation as a function of time after sunset. Significant scintillation begins at approximately 1.5 hours after sunset on the magnetic equator. The magnitude then continues to build until about 5 hours after sunset, at which time it diminishes until about 6 hours after sunset when it disappears. In the bottom plot, the scintillation

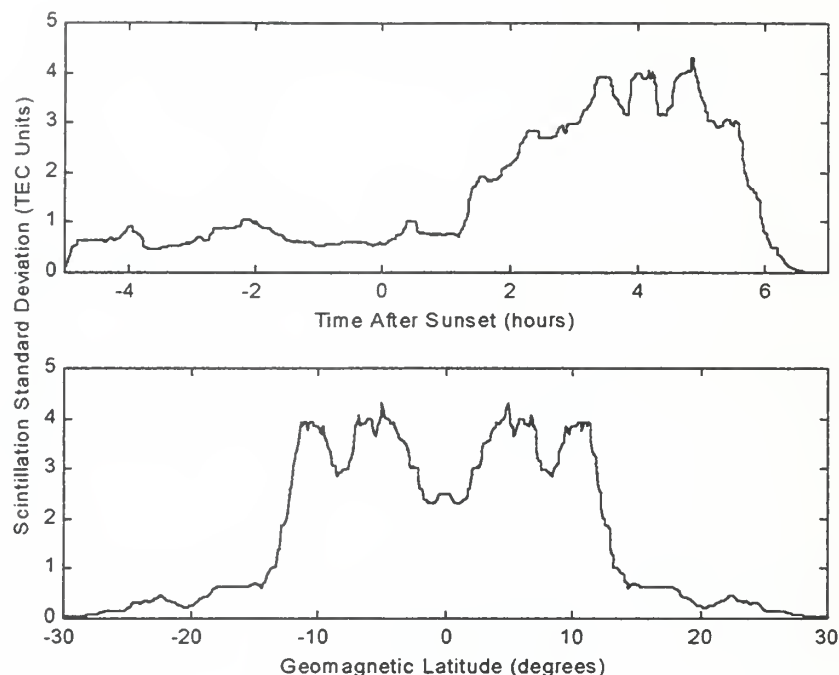


Figure 60. Scintillation standard deviation versus time and geomagnetic latitude

is seen to occur from about 14 degrees each side of the magnetic equator. Although there is still scintillation directly over the magnetic equator, the magnitude is not as great as it is at even two degrees away. In the top plot, surprisingly scintillation is evident prior to sunset. An explanation is found in Figure 61, where the scintillation before sunset exists in the neighborhood of 10 to 15 degrees, the location of the equatorial anomalies. This pre-sunset low-level scintillation is caused by the anomalies alone. Notice also that the late-afternoon shrinking of the anomalies is tracked by the GPS signals from -3 hours to -1 hour.

On the other side of the solar terminator, the scintillation becomes substantial about two hours after sunset. It spans from -15 to 15 degrees with a maximum at 10 degrees. This continues for two hours until four hours after sunset where the



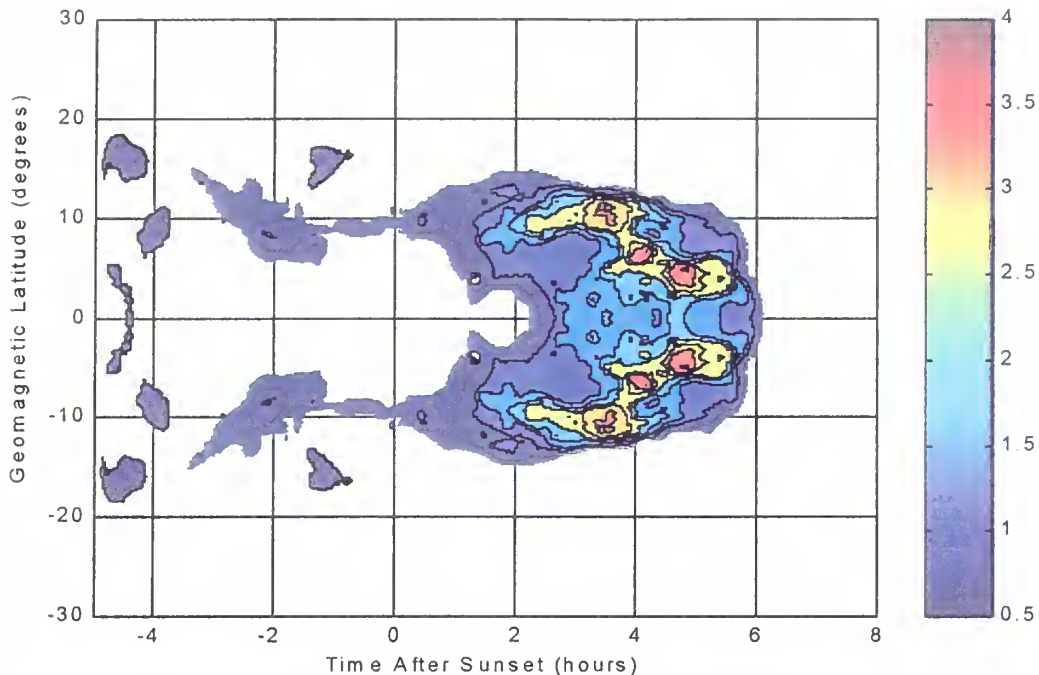


Figure 61. Scintillation standard deviation seen from above

intensity does not diminish (it increases) but the latitudinal spread lessens and withdraws toward the equator. At five hours after, the maxima are found at about four degrees. One final observation about this figure is although meaningful scintillation begins at about 1.5 hours after sunset, there is no scintillation directly overhead the equator for about another hour.

#### E. ELEVATION ANGLE EFFECTS

The scintillation analysis depends upon the measurements of TEC. The TEC is the integrated sum of the number of electrons between the observer and the transmitter. If the ionosphere were stratified, the fewest number of electrons on the path from transmitter to receiver would occur if the satellite transmitter were directly overhead. If the satellite moves from this position, the wave travels a longer path

through the ionospheric part of the journey. A longer path through a stratified ionosphere implies a higher number of electrons between the two sites, a greater TEC.

This concept applies to scintillating TEC as well. The minimum TEC scintillation will be measured directly overhead (an elevation angle of 90 degrees), and will increase with decreases in elevation angle. In Figure 50, the TEC of a quiescent day was pictured. It appears to be uniformly minimal across the entire time the satellite is within field of view. However, the TEC of Figure 50 is the equivalent vertical-incidence measurement. In its unmodified form, the TEC of Figure 50 is as shown in Figure 62 plotted against the elevation angle at which it was collected. Here it is seen that although the TEC is from an undisturbed ionosphere,

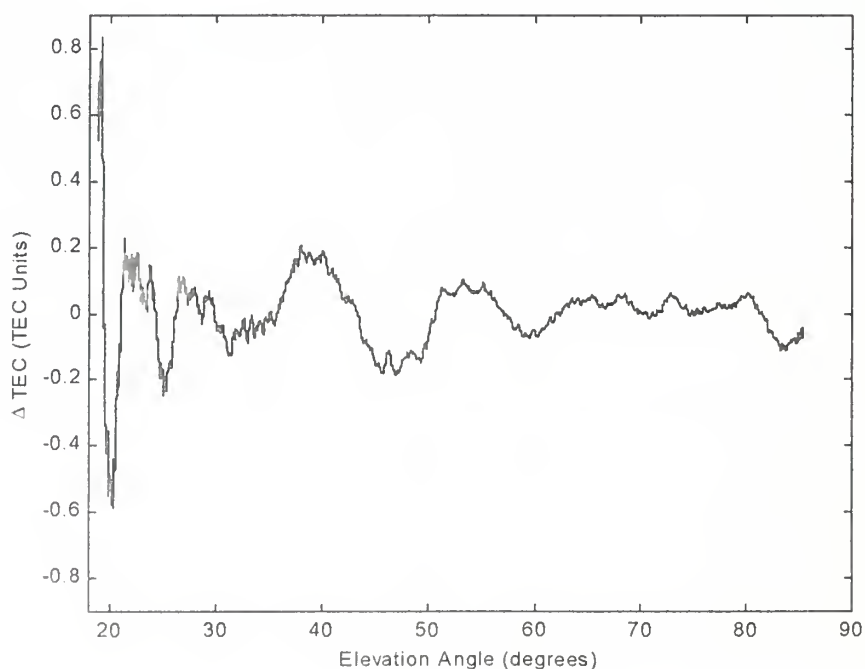


Figure 62. Variation of TEC as function of elevation angle.

the TEC increases as the elevation angle decreases from its most-near overhead position, with radical changes as the elevation angle approaches twenty degrees. This same elevation angle dependence is ubiquitous throughout the data set.

The scintillation that has been analyzed and discussed is relevant only to the overhead (elevation angle 90 degrees) position. At other elevation angles the TEC and its scintillation values will be increased based upon elevation angle. To allow for that effect, a compensation factor must be included in any scintillation computation algorithm. A reasonable compensation factor is

$$TEC_{vertical} = TEC_{slant} \cdot \left( 1 - e^{-\frac{\Delta - 18.5}{10}} \right), \quad (53)$$

(where  $\Delta$  is the elevation angle in degrees), and is plotted in Figure 63. This factor was used to transform the TEC data which have been used in the foregoing analyses.

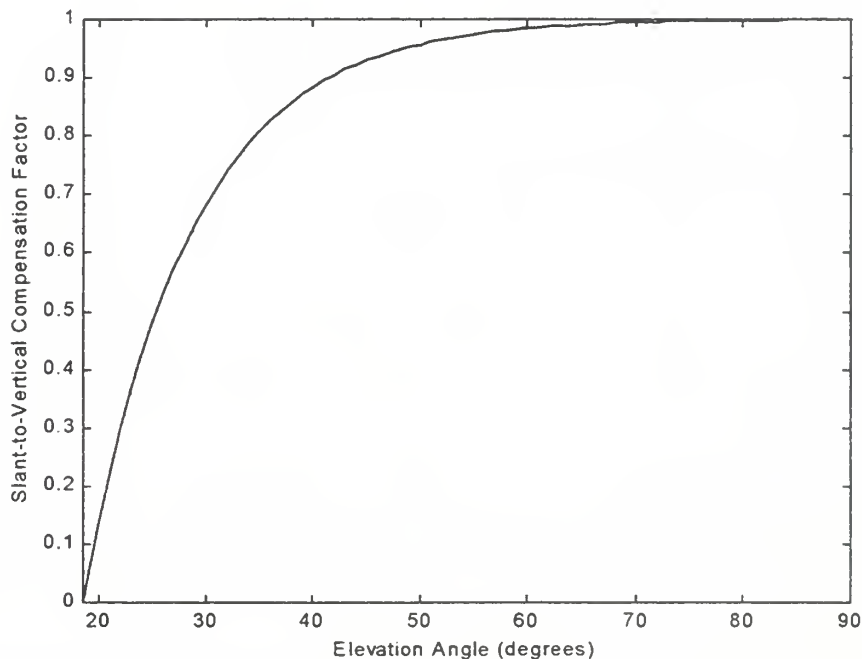


Figure 63. Slant TEC to Vertical multiplicative compensation factor.

When the receiver is aboard a space-borne vehicle, the elevation angle can be estimated using a topocentric system at the estimated location of the transmitter. This estimated elevation angle can then be used in Eq. 53.

#### **F. TEC SCINTILLATION EFFECTS UPON GEOLOCATION**

In Section D it was determined where and when scintillation will occur. However, its effects at those locations were not addressed. The scintillation can cause deviations in time, frequency, and angle measurements. Using the derivations of Chapter IV the errors caused by each of those factors will be discussed.

##### **1. Time Difference of Arrival Errors**

In Equation 30, it was determined that the time of arrival of the received signal is altered by the TEC using the relationship

$$\Delta t = \frac{1.34 \times 10^{-7}}{f^2} \cdot TEC = \frac{1.34 \times 10^9}{f^2} \cdot TEC \text{ Units.} \quad (54)$$

Time difference of arrival geolocation systems resolve distance from each receiver to the transmitter by multiplying time by the speed of light. Multiplying Eq. 54 by  $c$  results in the distance error of  $c\Delta t$ . A percentage error in the distance measurement can be computed based upon the height of the space platform. For two platforms, one at 1000 km height and the other at 20000 km height, the percentage error at one TEC unit is computed and shown in Figure 64. The percentage error is greater for the space platform closer to earth. For example, assume the frequency of the transmitted frequency is 10 MHz, the receiving platform is directly overhead at 1000 km, with one TEC unit of scintillation. From the plot, the percent error in distance

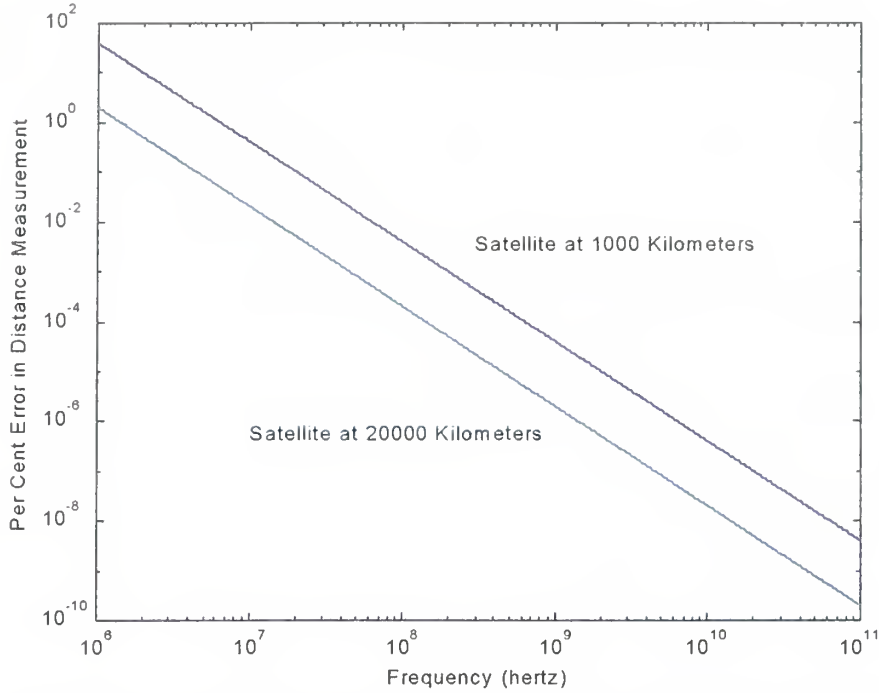


Figure 64. Distance measurement errors from two satellites

measurement will be approximately one percent. In Figure 60, the TEC scintillation is seen to be approximately three TEC units for most of the post-sunset, pre-midnight sector. In this case, the example cited above would increase to a three percent error in distance measurement. If the elevation angle from the transmitter were 20 degrees, Eq. 53 can be used to find the scintillation at this elevation angle, i.e.,

$$TEC_{slant} = \frac{TEC_{vertical}}{\left(1 - e^{-\frac{\Delta - 18.5}{10}}\right)}. \quad (55)$$

With  $TEC_{vertical}$  at three TEC units and  $\Delta$  at twenty degrees, the  $TEC_{slant}$  is found to be approximately 18 TEC units, with a resulting percentage error of approximately 50 percent.

By this analysis, the optimum observation position is directly overhead. As the position of the observer moves, the errors in the resolution progressively worsen. The amount of degradation is algorithm specific. Time and distance errors predicted here must be applied to the user's algorithm to determine individual effects.

## 2. Frequency Difference of Arrival Systems

From Equation 32, the change in frequency resulting from the change in TEC is given by

$$\Delta f = \frac{1.34 \times 10^9}{f} \frac{d}{dt} (\text{TEC Units}) \text{ Hz.} \quad (56)$$

As an example of change in TEC with respect to time, the TEC of PRN2 on Julian Day 259 shown in Figure 46 is expanded around time 2100 as shown in Figure 65. The

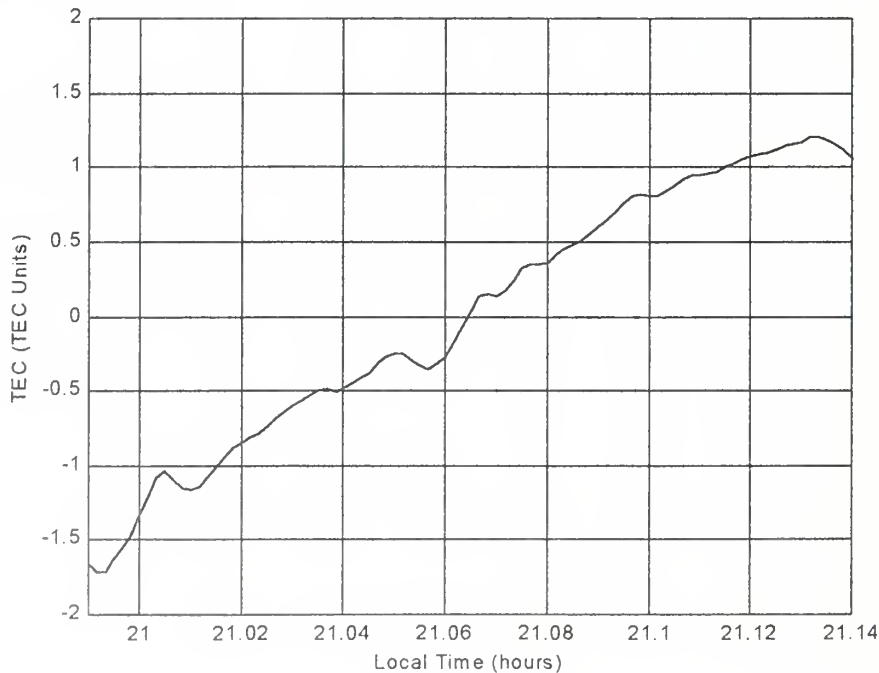


Figure 65. Change in TEC with change in time

plot shows a change in TEC of about 3 TEC units during a time change of approximately 0.14 hours, or 0.006 TEC units per second. Substituting this value for  $d/dt(\text{TEC Units})$  in Eq. 56, the change in frequency for this case can be computed. Figure 66 shows this frequency deviation as a function of transmitted frequency. For a transmitted frequency of 10 MHz, the change in frequency at the receiver is seen

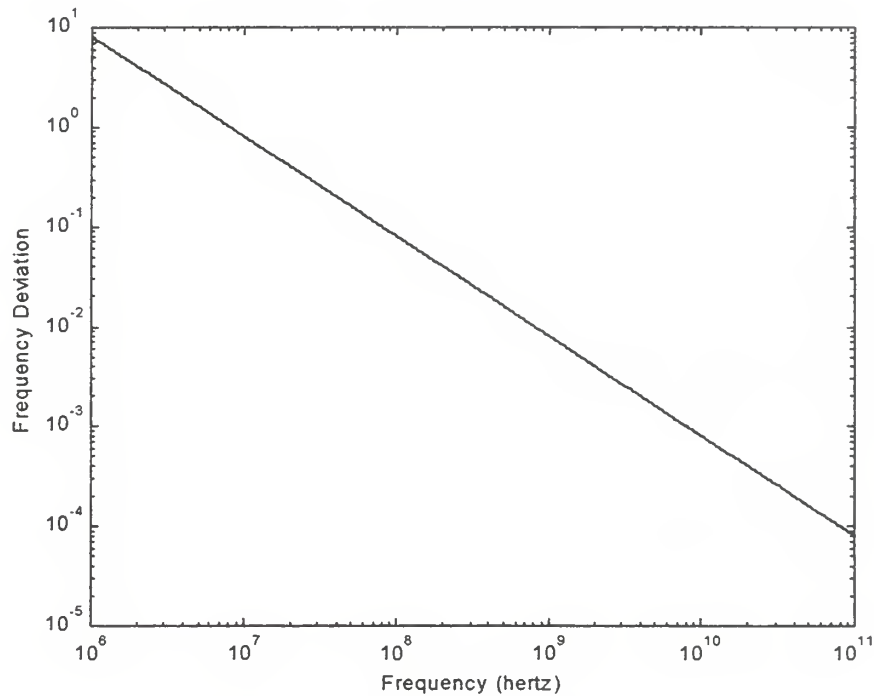


Figure 66. Frequency deviation caused by scintillation

to be about one hertz. Based on the previous derivation based upon three TEC units, at 20 degrees elevation, the frequency change is about 18 hertz.

These values must be tested in the user's algorithm to determine the extent of the degradation to geolocation.



### 3. Angle of Arrival Systems

To use wedge refraction theory, the change in TEC with respect to horizontal distance is required. The time derivative of Figure 65 can be used to estimate this spatial derivative. The TEC time derivative was found to be approximately 3 TEC units in 0.14 hours. On the equator, one hour equates to 15 degrees of longitude which is equivalent to 1665 kilometers. The spatial derivative is estimated as 3 TEC units per 233 kilometers or  $13 \mu\text{TEC}$  units per meter. From Eq. 33

$$\alpha = \frac{40.3 \times 10^{16}}{f^2} \frac{d}{dx} (\text{TEC Units}), \quad (57)$$

where  $\alpha$  is in radians. Substituting for the spatial derivative, the angle deviations can be computed as a function of frequency as shown in Figure 67. At 10 MHz, the

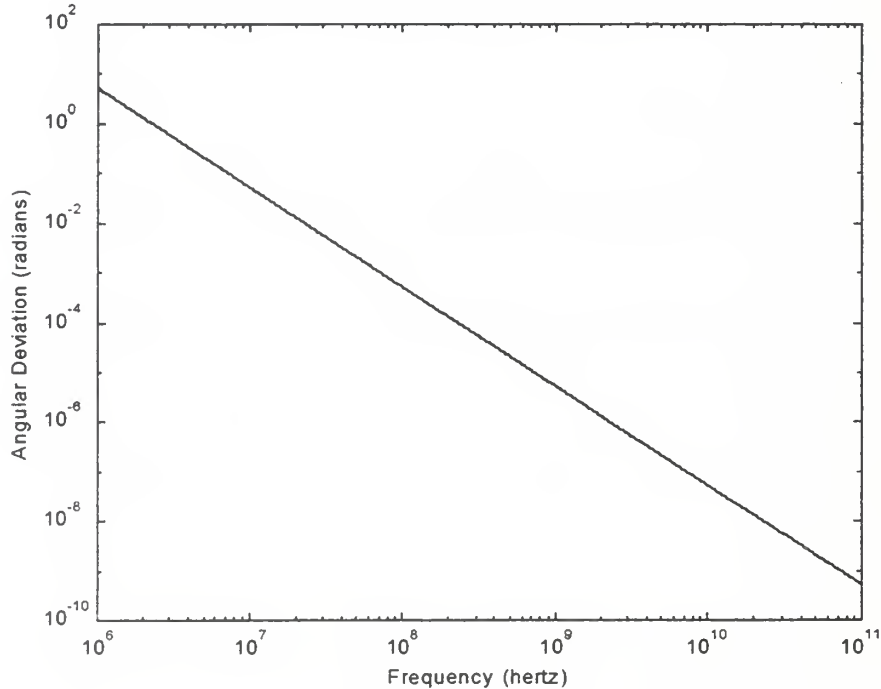


Figure 67. Angular deviation due to spatial TEC variation

angular change is 0.1 radian, or 5.7 degrees. At 1000 km altitude, this equates to about 25 kilometers on the ground. As before, this plot is for an overhead receiver. Receivers at positions other than the optimum suffer even more severe errors.

## G. SCINTILLATION PREDICTION

The prediction of the ionospheric TEC scintillation can be divided into two different areas. First, the prediction of the probability that scintillation will exist, and second, when scintillation is present, where it will occur and with what magnitude.

### 1. Probability of Scintillation

Analysis of the data in Figures 46, 48, 49, and 50 shows that the presence of the VHF signal implies scintillation and vice-versa. This is shown for a few examples. Thus, a prediction of one is a prediction of the other. Prediction of VHF signal propagation was developed in Chapter VI. The MATLAB program used to compute the VHF probability has been modified slightly to predict scintillation and is included as Appendix E.

### 2. Space-Time Distribution

The distribution prediction modeling is based upon the results shown in Figures 60 and 61. The top plot of Figure 60 shows the magnitude of the scintillation based upon time after sunset can be modeled with two exponentials, one to model the rise and peak and the other to model the fall. The equations of these two exponentials are

$$timemag1 = 3.5 \cdot \left( 1 - e^{-\frac{TAS - 1}{0.9}} \right), \quad 1 < TAS \leq 5.5, \quad (58)$$

and zero otherwise for the first, and

$$timemag2 = 3.5 \cdot \left( e^{-\frac{TAS - 5.5}{0.3}} \right), \quad 5.5 < TAS < 7, \quad (59)$$

and zero otherwise for the second where TAS is time after sunset. Scintillation with respect to time after sunset is the sum of timemag1 and timemag2. A plot showing both the top plot of Fig. 60 and this sum is shown in Figure 68. Note that since this

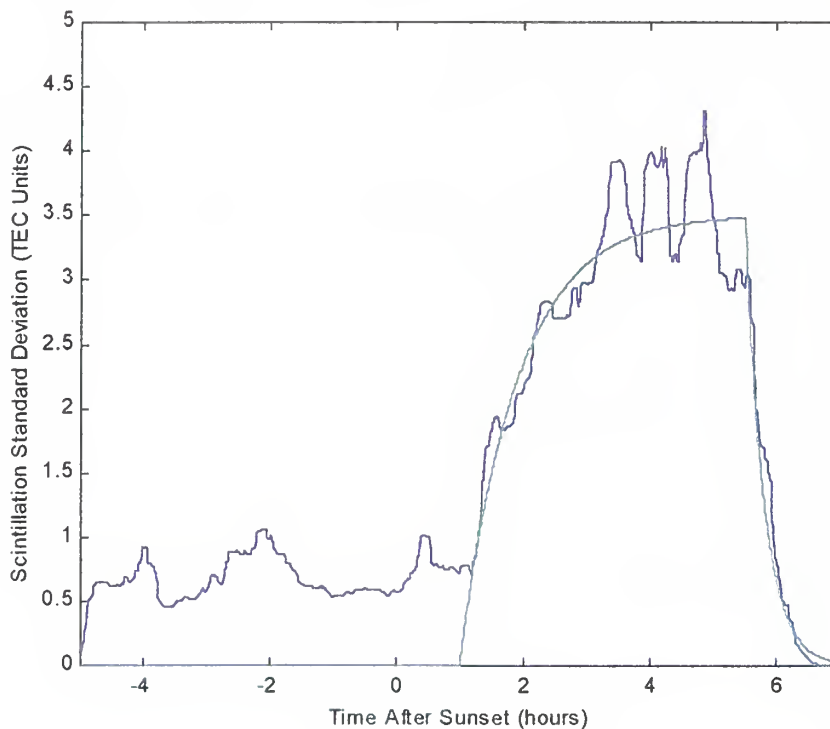


Figure 68. Time after sunset observation and model.

is a nighttime effects model, all effects prior to one hour after sunset have been eliminated. The purpose of this mathematical model is to predict the scintillation versus time. Scintillation is also a function of latitude, as shown in Figures 60 and 61.

To derive mathematical descriptions of the scintillation variation with respect to latitude, the bottom plot of Figure 60 and Figure 61 will be used. First, the peak latitude as a function of time will be patterned. The greatest latitudinal extent is about 15 degrees occurring approximately two hours after sunset. The latitude peak for this time is 12 degrees. The peak latitude decreases from there until six hours after sunset. A cosine fit to this peak and fall-off is

$$peaklat = 12 \cos\left(\frac{2\pi(TAS - 2)}{17.5}\right), \quad 1 \leq TAS \leq 7. \quad (60)$$

From the latitude of peak scintillation at any given time, the magnitude falls off steeply at latitudes greater than peak, and gradually at latitudes less. For the greater latitudes, the magnitude falls as a cosine with zero magnitude attained at six degrees above peak latitude, i.e.,

$$abovemag = 0.5 \cdot \left( 1 + \cos\left(\frac{2\pi(peaklat - maglat)}{12}\right) \right), \quad (61)$$

$peaklat \leq maglat \leq peaklat + 6$ , where  $maglat$  represents geomagnetic latitudes, in this case greater than the peak latitude. The magnitude at latitudes less than peak is

$$belowmag = 0.5 \cdot \left( 1 + \cos\left(\frac{2\pi(peaklat - maglat)}{32}\right) \right), \quad (62)$$

$0 \leq maglat < peaklat$ .

The predicted scintillation magnitude at a given TAS and geomagnetic latitude can be determined by the following steps:

- 1) Determine the magnitude with respect to time using either Eq. 58 or 59. Call this value *timemag*.
- 2) Use Eq. 60 to determine the location of peak latitude, called *peaklat*.
- 3) Either Eq. 61 or 62 is used to determine the modifying factor based upon latitude. Call this value *latfactor*.
- 4) The predicted value of scintillation is then the product of *timemag* and *latfactor*.

A MATLAB program to compute these values is contained in Appendix F. Figure 69 shows a plot with all relevant times and latitudes and Figure 70 shows an overhead view.

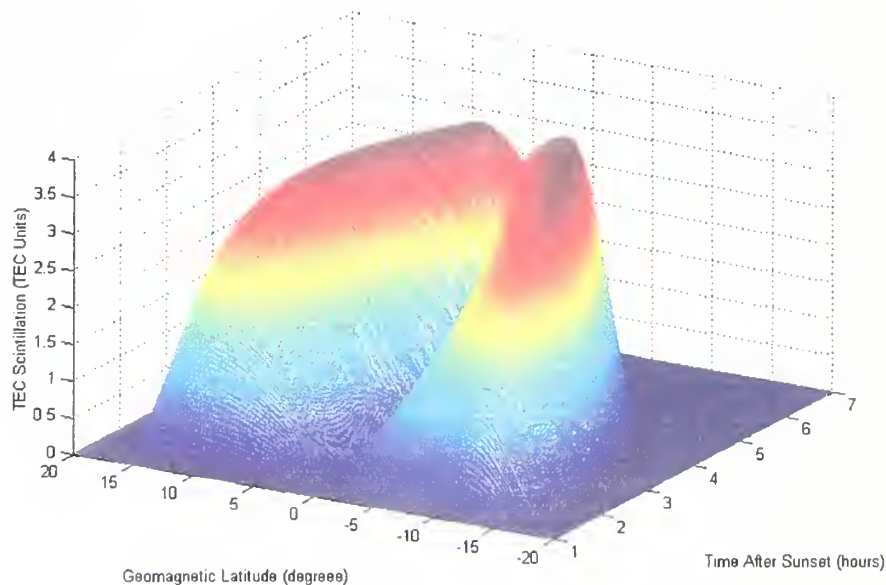


Figure 69. Plot of predicted TEC scintillation

The equations and plots above are for overhead observer only. If the elevation angle from earth to satellite is not 90 degrees, then the results obtained above must be modified from vertical to slant TEC using Equation 55.

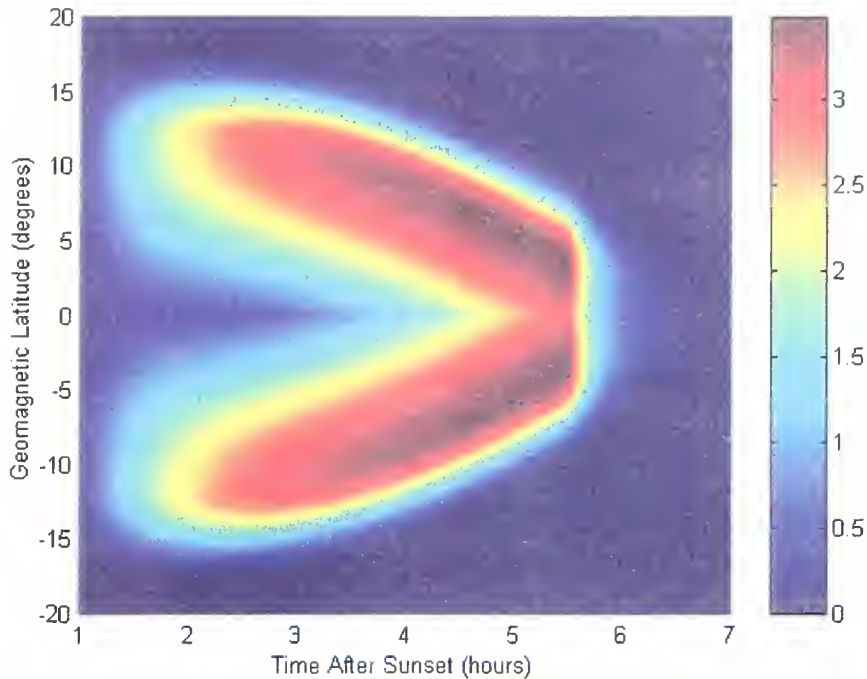


Figure 70. Scintillation prediction from above.

The magnitudes of the scintillation predictions are based upon a data set collected at sunspot minimum. The scintillation dependence upon sunspot number cannot be determined from this data set, but it is anticipated that the observations here are the “best case” conditions.

#### H. NON-TEP SCINTILLATION

It has been shown that TEP and low-latitude scintillation are separate, independent, but correlated manifestations arising from the Rayleigh-Taylor instability of the anomalies. When TEP occurs, an ionospheric duct is the conduit which permits the propagation. Due to the irregularities in the duct ceiling, scintillation of a transionospheric signal coexists with the TEP.

There exists the possibility of the Rayleigh-Taylor instability developing within each anomaly without formation of ionospheric ducts. Bubbles could rise within the anomalies but never elongate sufficiently to adjoin. Alternatively, a bubble could form in one anomaly but not the other. In these circumstances no TEP would transpire, but scintillation would.

The measure of scintillation magnitude adopted here has been the running standard deviation of TEC. The peak RSD for each day of the experiment is shown in Figure 71. The average peak RSD for the entire record is 0.99 TEC units.

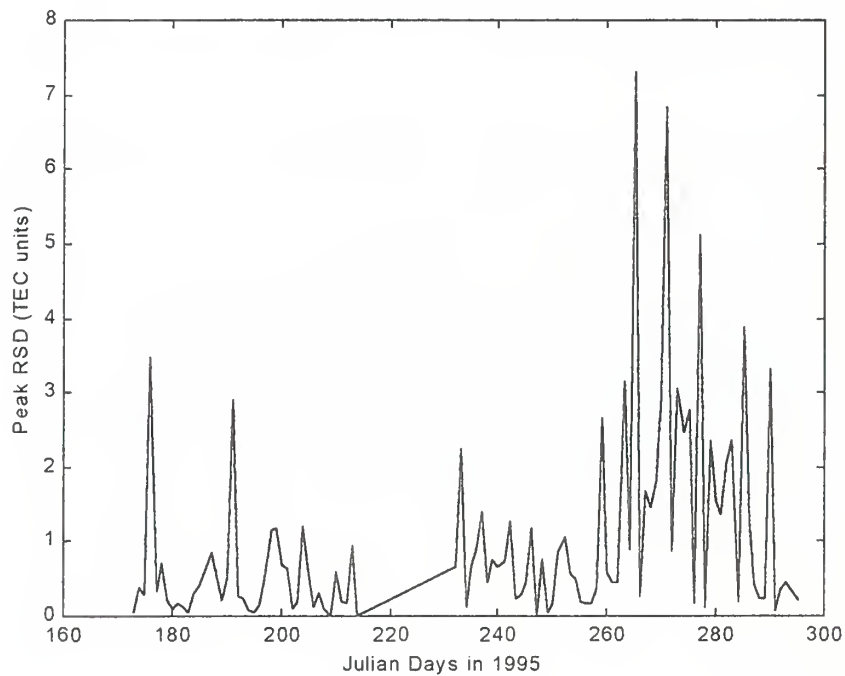


Figure 71. Peak RSD for each day of the GPS experiment. The line between days 218 and 230 indicates an absence of data on those days.



The peak RSD for days with and without TEP can be plotted separately to determine if scintillation is significant on days without TEP. Figure 72 shows the

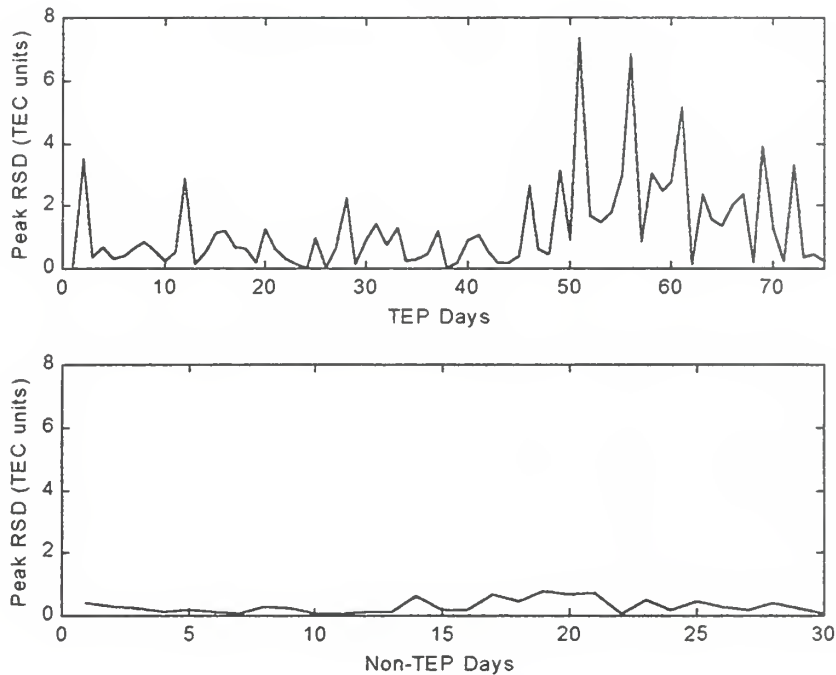


Figure 72. Peak RSD. The top plot shows the RSD for days when TEP occurred, while the bottom depicts the values when TEP did not occur.

peak RSD over the record divided into days when TEP occurred, shown in the top plot, and days when it did not, on the bottom. The RSD on TEP days shows a maximum of about seven TEC units while the non-TEP plot has a maximum of about 0.7. The average peak RSD for TEP days is 1.27, and for non-TEP 0.29 TEC units.

While it cannot be stated that scintillation does not exist on days when TEP is not present, it is apparent that its severity is greatly reduced. The average value of 0.29 TEC units on non-TEP days barely exceeds the significance threshold

established earlier of 0.25 TEC units. It is therefore concluded that scintillation does not occur, in a practical sense, without the formation of a TEP conducting ionospheric duct.

## VIII. THE ANCILLARY EXPERIMENTS

Two ancillary investigations were performed which supplement the VHF transequatorial and GPS transionospheric experiments. The first supplemental experiment was the measurement of transequatorial propagation in the opposite direction to the VHF propagation. The other was the evaluation of airglow overhead Christmas Island which was taken to augment the GPS scintillation data there.

### A. THE IONOSONDE EXPERIMENT

An oblique incidence digital ionosonde was activated from Rarotonga to Oahu over the time period 26 August to 25 September 1995. The purpose of the experiment was two-fold: (1) determine the bi-directionality of the VHF TEP, i.e., determine if propagation in one direction implies propagation in the other and (2) allow observation of afternoon-TEP.

The information supplied by an ionogram consists of a plot of the time-of-flight for the frequencies which propagate. In order to make some sense of the time-of-flight numbers, an analysis of the geometry of the path must be undertaken. Using the geometrical distances of different flight profiles and a propagation velocity of  $c$ , estimated times-of-flight can be obtained.

The two forms of TEP, afternoon and evening, arrive at the receiver from different paths. The afternoon-TEP path allows reflection from one anomaly to the other, then to the receiver. In order to compute the path length and propagation time, both the heights and positions of the anomalies must be estimated. The

geometry of the afternoon-TEP path is pictured in Figure 73. The path is divided into three segments:  $P_1$  from transmitter to first reflection point,  $P_2$  from the first to the

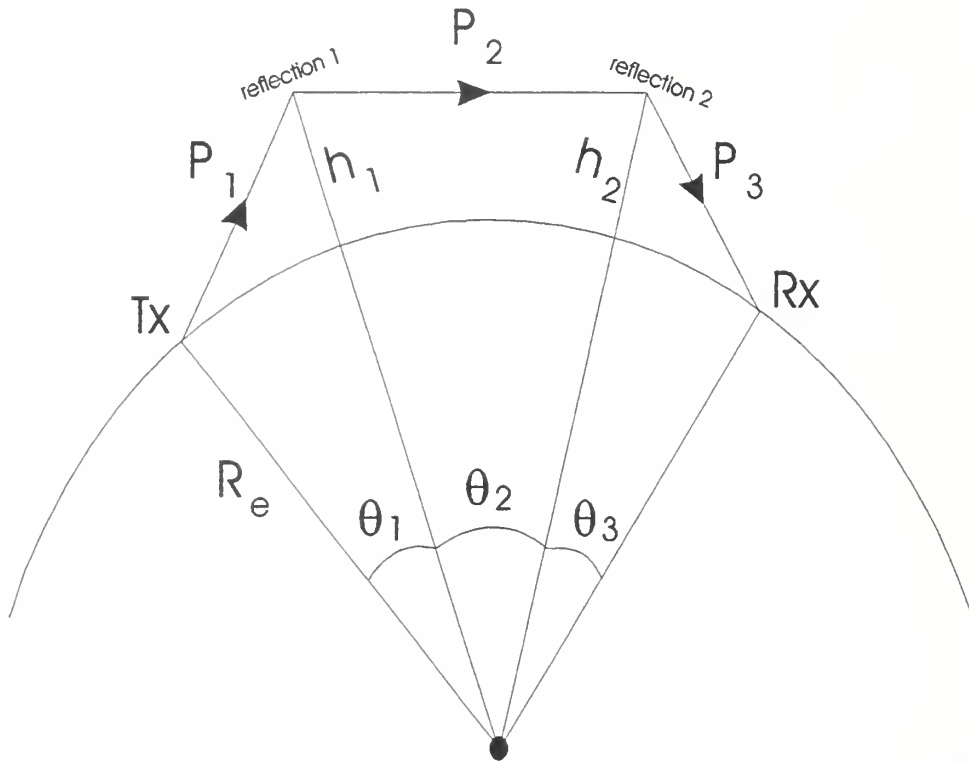


Figure 73. Afternoon-TEP path geometry.

second reflection point, and  $P_3$  from second reflection point to receiver. Simple trigonometry using the radius of the earth ( $R_e$ ),  $h_1$ ,  $h_2$ , and the angles  $\theta_1$ ,  $\theta_2$ , and  $\theta_3$  can be used to solve for the three path lengths. Since the anomaly positions are not known a priori, the values of  $\theta_1$ ,  $\theta_2$ ,  $\theta_3$ ,  $h_1$ , and  $h_2$  must be estimated. For typical values of anomalies positioned at  $\pm 12^\circ$  geomagnetic latitude,  $\theta_2$  is  $24^\circ$ . The angles  $\theta_1$  and  $\theta_3$  can be found using the transmitter and receiver latitudes. Reflection heights can be estimated as  $h_1 = h_2 = 250$  km. Using these values, a path length of approximately 4900 km is found with a time-of-flight of 16.3 milliseconds. This represents the flight time for the low ray reflected from the anomalies. There exists

the possibility of a high ray, as well. The time-of-flight of the high ray will be greater than that of the low ray, except at the maximum propagation frequency, where they merge.

For evening TEP, if the ray path follows a magnetic field line from transmitter to receiver, an estimate of the path length can be attained. The length of the magnetic field line, from Equation 1, produces a path length of approximately 5025 km with a flight time of 16.7 ms.

Using these estimates of time-of-flight over paths of the two types of TEP, selected ionograms recorded during the experiment were examined. The following ionograms were selected from the recordings made on September 25. The first one, taken at local time 1527, is a normal, HF-limited ionogram, shown in Figure 74. The

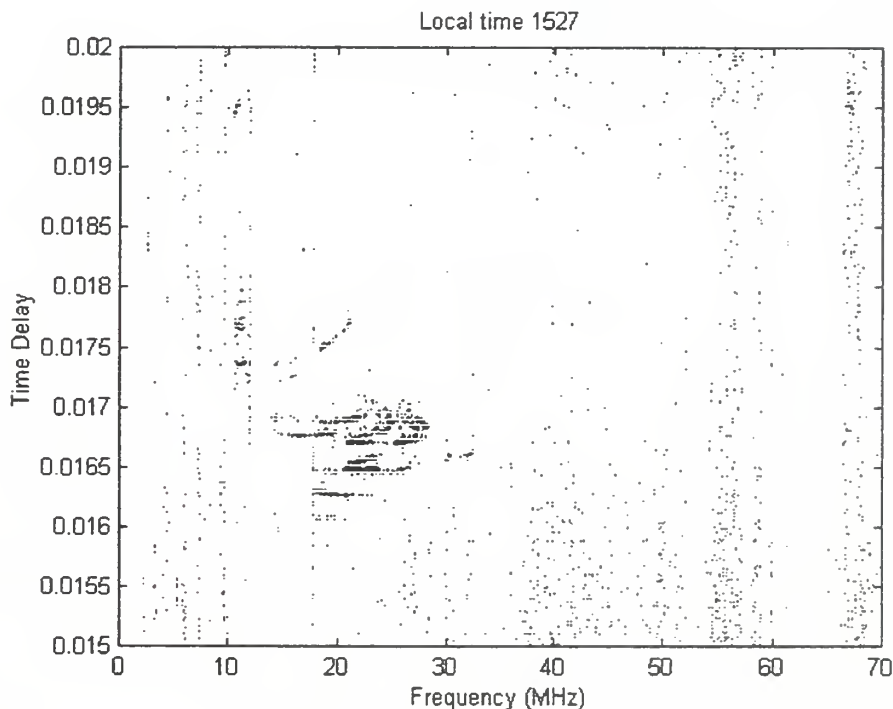


Figure 74. HF ionogram at 1527.

maximum observed frequency (MOF) is about 30 MHz. The time-of-flight is consistent with that of high altitude propagation with possibilities of multiple hops evident. This is not TEP, but indicates a high density ionosphere, reflecting HF.

In the second ionogram, Figure 75, taken 10 minutes later, the same HF reflected traces are still visible, but a new trace reflecting much higher frequencies appears. This new trace, arriving at approximately 16.3 ms, is the emerging

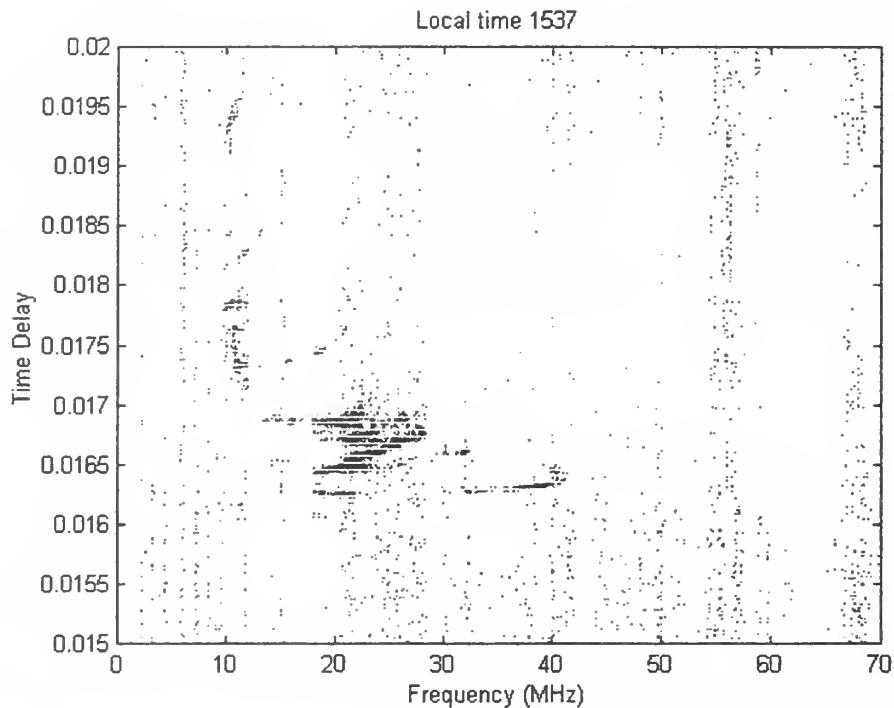


Figure 75. Emerging Afternoon-TEP at 1537.

afternoon-TEP with a MOF of about 40 MHz. The time-of-flight is consistent with the theoretical time-of-flight for afternoon-TEP derived above. Both the low and high rays are seen on the trace. The TEP trace continues to strengthen and allows higher propagation frequencies, shown in Figure 76. The MOF is about 46 MHz at 1632 local time.

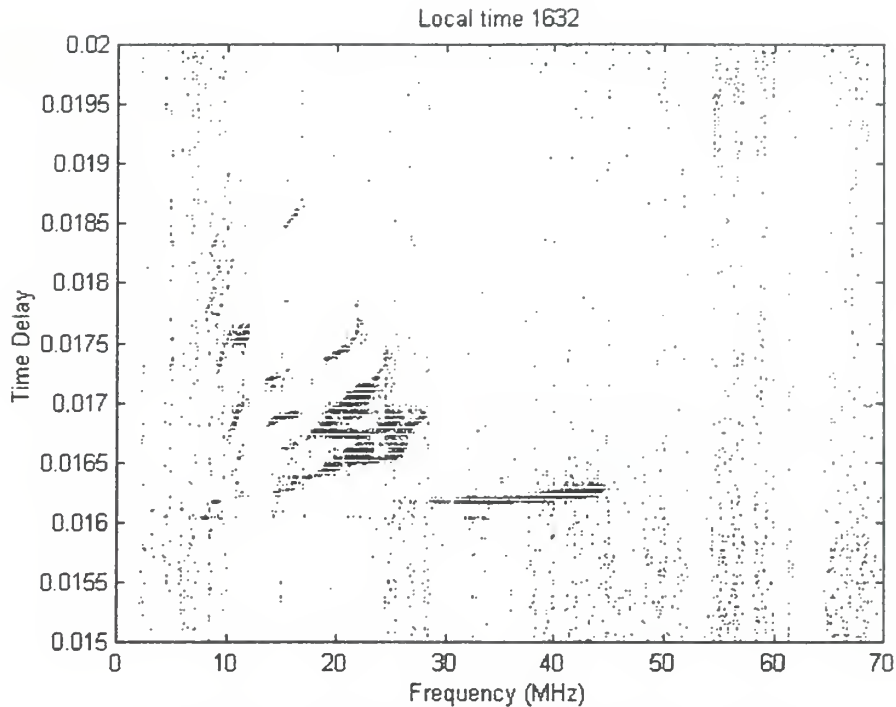


Figure 76. Afternoon-TEP extending to 46 MHz.

The afternoon-TEP trace continued until after sunset. At 1852 local time, the recorded ionograms begin a radical alteration as shown in Figure 77. The afternoon-TEP trace has all but disappeared but the trace at approximately 16.7 ms is extending into the VHF region. Twenty minutes later, the continued extension of this trace approaches 50 MHz, as shown in Figure 78. The time-of-flight of the frequencies observed on this trace is also consistent with that derived for evening-TEP and shows the emergence of evening-TEP. This behavior continues until the layer reflections have all but disappeared and the MOF continues to increase, as shown in Figure 79. The reception of evening-TEP continues throughout the evening, but in Figure 80, near midnight, signals begin to weaken, as the propagation mechanism is dissipating.



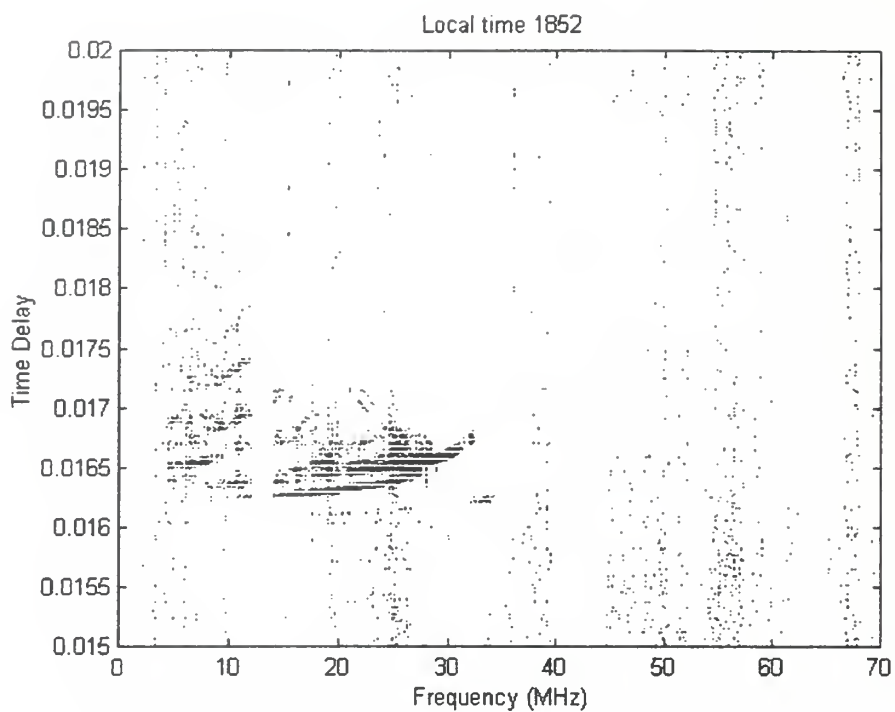


Figure 77. Afternoon-TEP trace disappears at 1852.

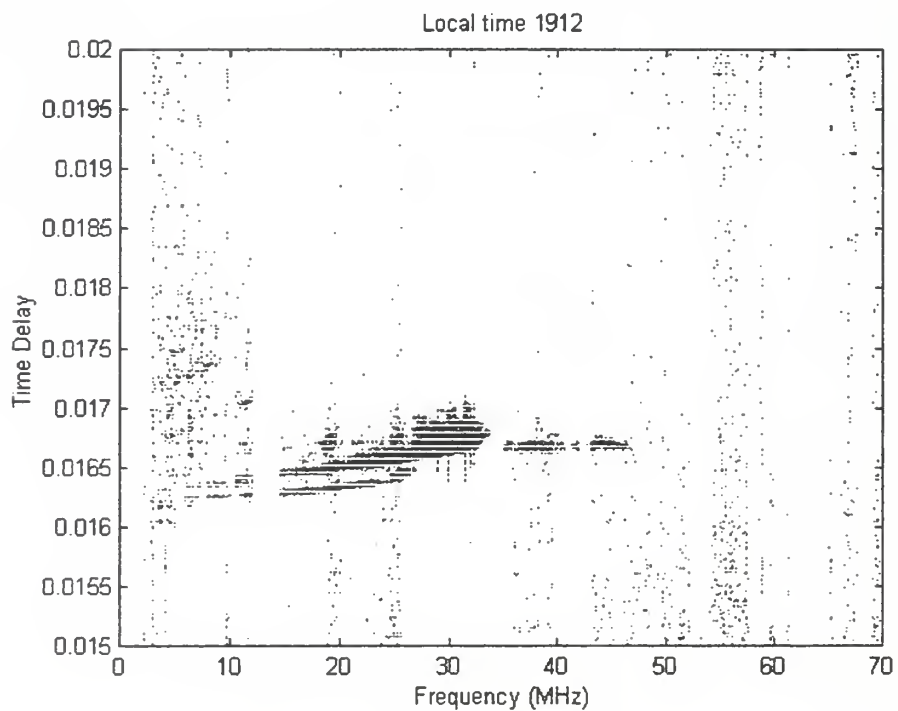


Figure 78. Evening-TEP develops.

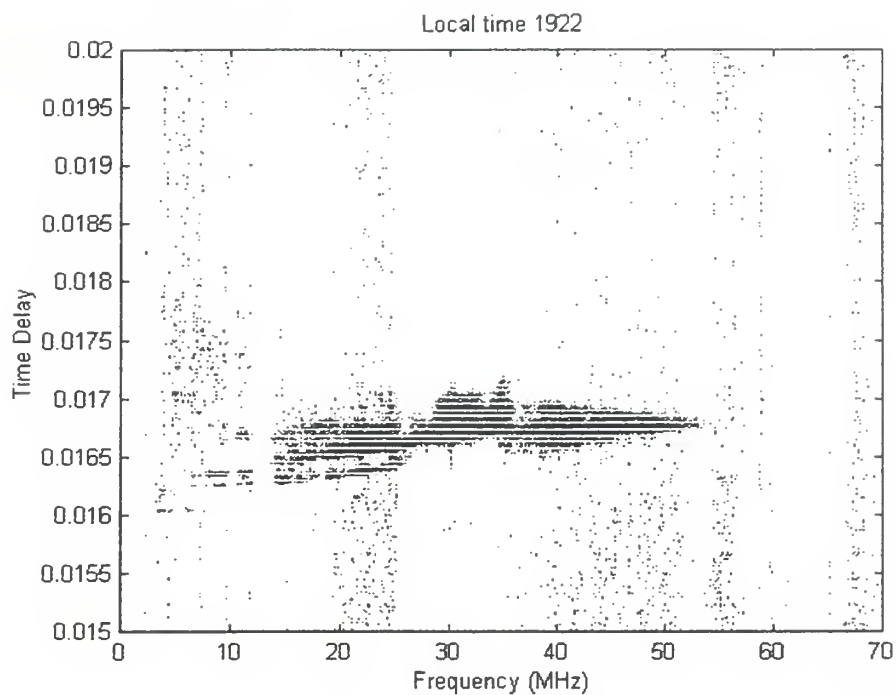


Figure 79. Evening-TEP.

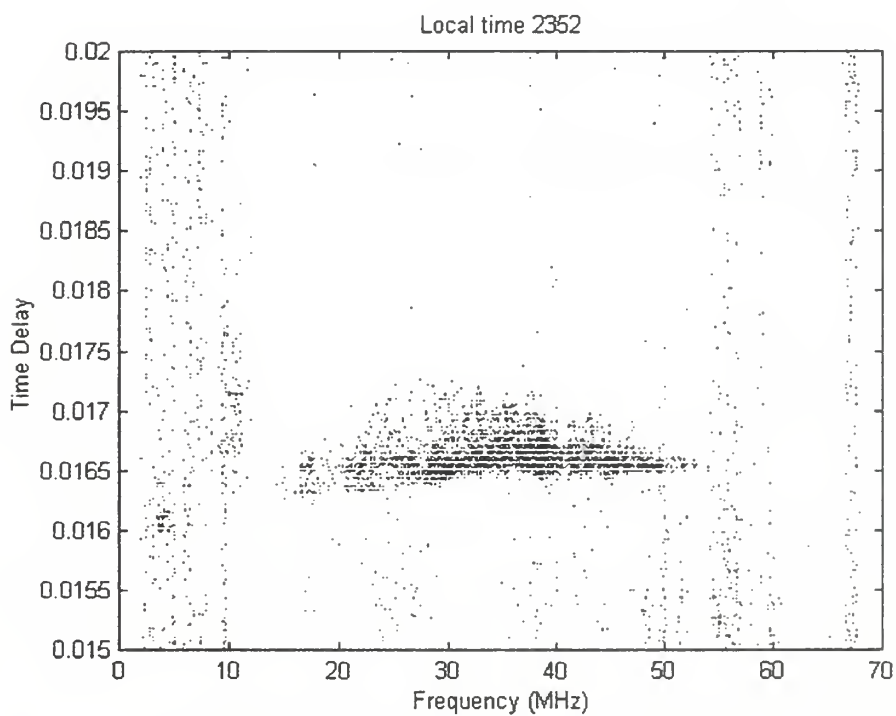


Figure 80. Dissipating evening-TEP.

An appreciation for the frequencies the two TEP types will support is obtained from the maximum observed frequency of each ionogram, shown in Figure 81. The maximum observed frequency of evening-TEP was 65 MHz while the afternoon-TEP maximum was about 45 MHz.

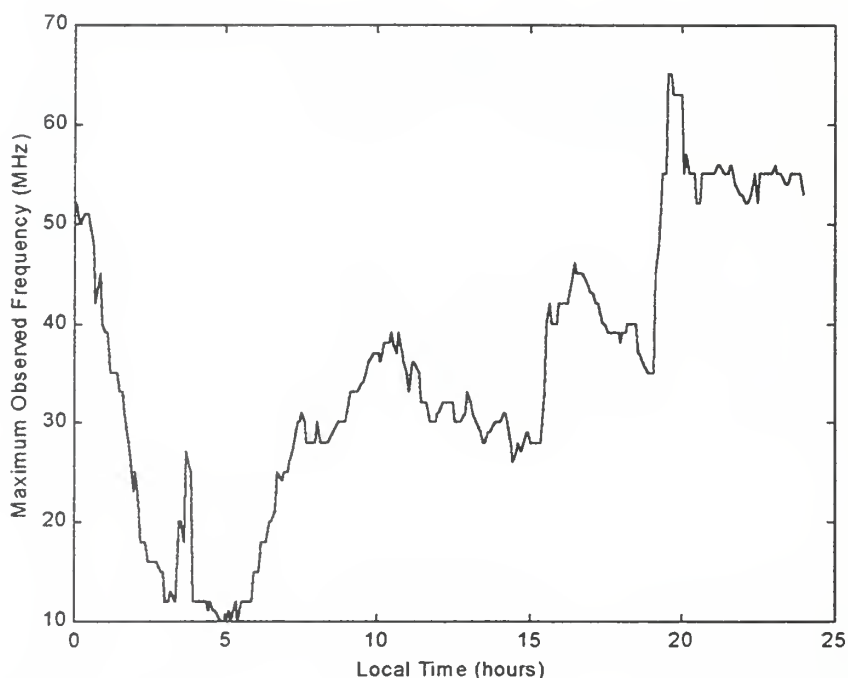


Figure 81. Maximum observed frequencies over 24 hours at Oahu.

The bi-directionality of the path is established if for each night of VHF evening-TEP there is also a TEP on the sounder circuit. The onset and cessation times for both paths for the days when the sounder was operational are plotted in Figures 82 and 83. The plots show that both the start and stop times are comparable. More important, the paths are bi-directional with the exceptions of Julian days 239 (south-to-north only) and 260 (north-to-south only).

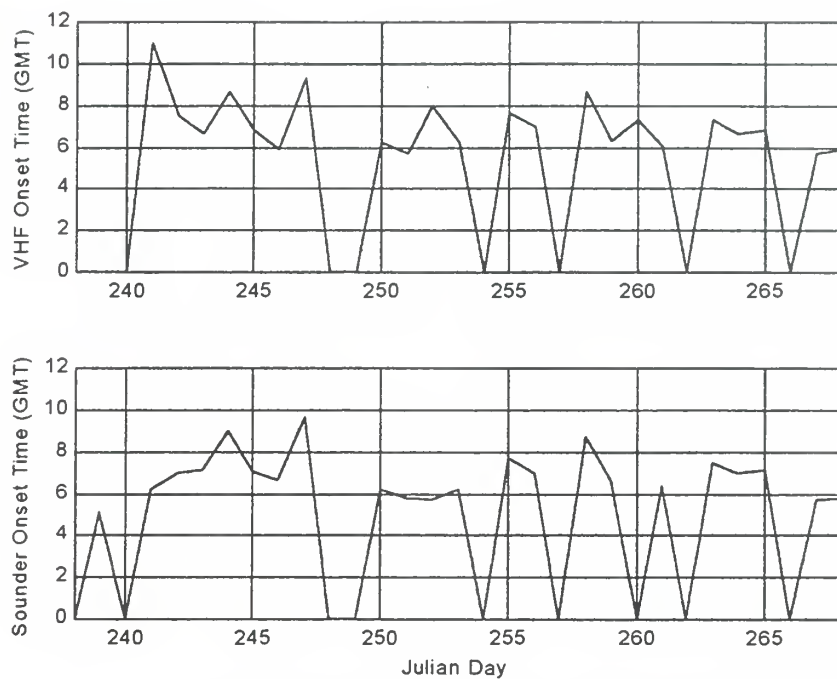


Figure 82. VHF and sounder onset times.

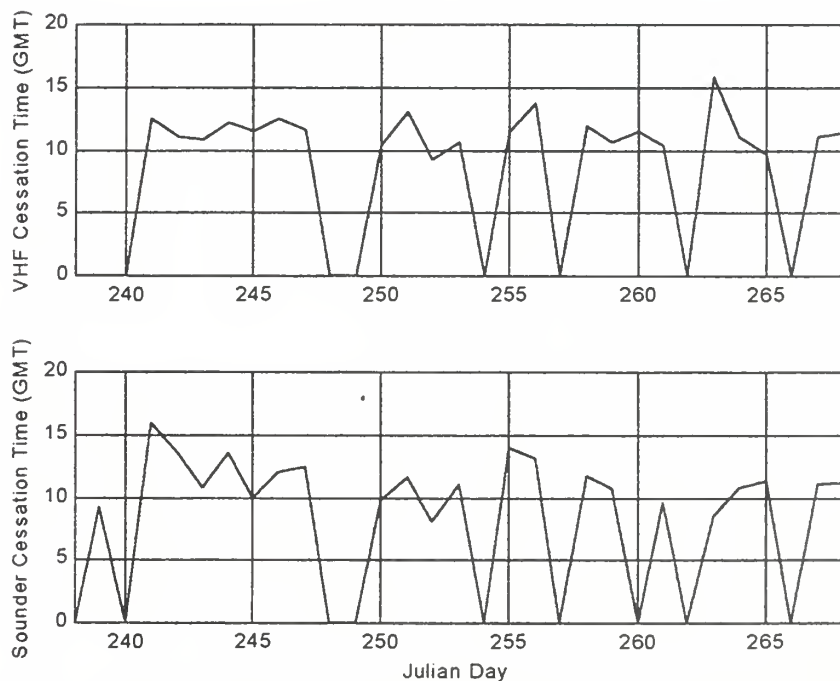


Figure 83. VHF and sounder cessation times.

## B. THE AIRGLOW EXPERIMENT

An airglow monitor was placed at Christmas Island from 14 September through 2 October 1995. The purpose of observing the airglow variations overhead Christmas Island was two-fold. The first and primary objective was to obtain an independent verifier of the GPS-TEC scintillation data. The second objective was to appraise airglow monitoring as a real-time evaluator of the presence of ionospheric ducts.

Ionospheric scintillation was shown in Chapter VII to be observable using GPS. Simultaneous observations of the ionosphere directly overhead Christmas Island via GPS signal scintillation and airglow variation provides independent and useful verification of the findings of Chapter VII.

Comparison of the two data sets is not trivial. Since the airglow data consists of zenith intensity measurements, the GPS data to correlate it with must come from directly overhead, also. This limits the amount of data available for comparison as many GPS satellites do not cross overhead on a given day. Furthermore, satellites which do cross overhead pass quickly, making comparison even more difficult.

GPS signals observed solely at zenith do not provide enough information for comparison. The satellite signal must be observed for some period of time before and after the time of overhead crossing. The filtering criterion used in this analysis for GPS signal comparison was  $\pm 4^\circ$  from zenith in both latitude and longitude. While this window is narrow enough to ensure spatial correlation, observations off zenith must be translated in time to transform them to the overhead position. The

airglow and GPS signals are not calibrated to the same units so absolute magnitude comparisons are not useful. Instead, both signals are normalized so that relative magnitude changes can be compared. After transformation and normalization, the airglow and GPS signals can be plotted together for correlation.

The plot of airglow and GPS data from Julian Day 271 in Figure 84 show airglow intensity variations in blue while the signals from several GPS satellites are in green. On this night, TEP did occur and scintillation is evident on the GPS signals. Note the significant variability in the airglow intensity signal. Although the airglow

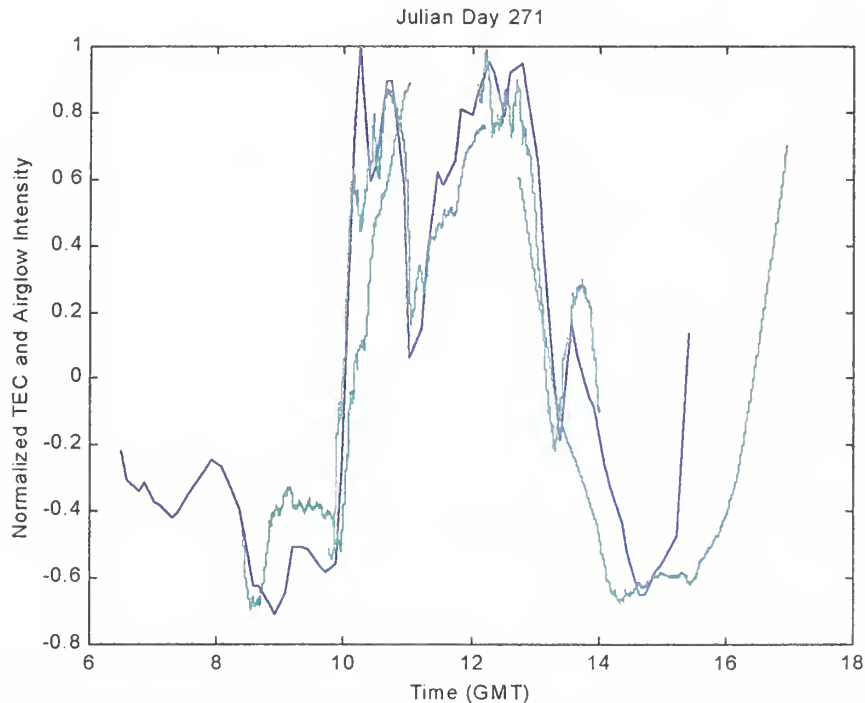


Figure 84. Normalized Airglow and TEC during TEP.

and GPS signals do not closely track each other, it is evident that similar processes created both and that they are correlated.

Figure 85 shows a similar plot for Julian Day 257 when TEP did not occur. Only one satellite passed overhead during the time of airglow data recording but its waveform in green follows the airglow trace in blue. Equally as important is the fact that the structure formed during TEP (shown in the measurements of Figure 84), is absent in this figure, when there is no TEP.

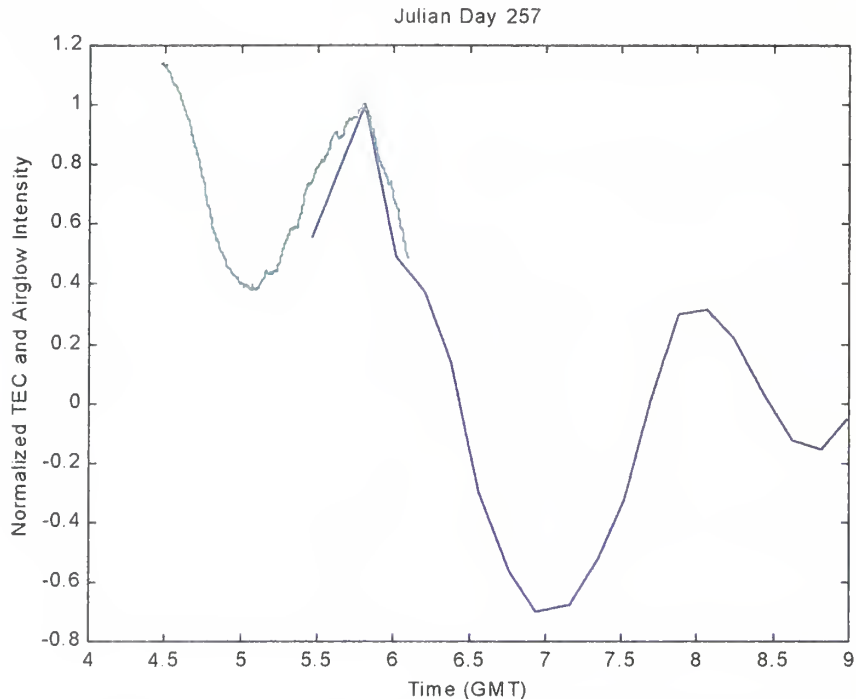


Figure 85. Normalized Airglow and TEC with no TEP.

It is evident from these figures that airglow intensity is correlated with GPS TEC measurements. It is also seen that airglow observations are a reliable indicator of the presence of ionospheric ducts. However, complete correlation of the two signals was impossible because only the zenith airglow data were analyzed. This limitation eliminated most of the GPS measurements from the correlation data pool, permitting only a cursory comparison.



## IX. CONCLUSIONS AND RECOMMENDATIONS

The two major objectives of this research were to attain an ability to predict (1) the when and where of transequatorial propagation and (2) the temporal and spatial distribution of low-latitude transionospheric signal scintillation. These goals were met using radio circuits, GPS receivers, airglow monitoring, and an oblique ionosonde. The primary contributing factor to the predictive algorithms was found to be the relative solar intensity.

### A. TRANSEQUATORIAL PROPAGATION PREDICTION

From observations and analysis of transequatorial VHF propagation, a list of the physical parameters which exercise control over propagation variables has been identified. Propagation variables which were identified, and for which predictions were produced, are the circuit onset time, the circuit cessation time, the probability of the existence of the circuit, and the path loss. The physical parameters, used as predictors, controlling these variables are the 10.7 cm solar flux, the magnetic declination angle, and the solar magnetic angle, all related to the intensity and relative position of the sun.

Using algorithms derived in Chapter VI, a user must simply supply the latitude and longitude of a transmitter, the frequency, the solar flux value, and the date. For a given receiver location, the outputs are:

- 1) the probability of a TEP circuit developing,
- 2) the predicted starting and stopping times given that the circuit exists, and

3) the path loss.

The propagation path was shown to be bi-directional over 28 of 30 days, 93% of the time. On the two days when bi-directionality did not exist, one day allowed propagation north-to-south and the other the south-to-north, eliminating different circuit gain margins as a cause. While greater than 90% is within acceptable limits of ionospheric predictability, it is not known why signals will propagate in one direction and not in the other. Possibly the magnetic field renders the ducts non-reciprocal so that bi-directionality was present on all the days but signal strength in one direction was severely attenuated. The science of low-latitude ionospheric ducts is still maturing.

#### **B. SCINTILLATION AND GEOLOCATION**

Global positioning receivers have proven to be an invaluable asset in monitoring both the quiescent and disturbed ionosphere. By capitalizing on the coherent frequencies of the GPS signal, the traveling disturbances in the equatorial region can be observed, quantified, and predicted.

The occurrence of scintillation was found to be very highly correlated with TEP. No cases of severe running standard deviation scintillation were observed in the absence of TEP.

The predictability of low-latitude scintillation, both in time and in space, has been demonstrated. Mathematical relationships have been developed to help predict the scintillation value at an arbitrary point in time and location in the low latitude ionosphere.

The impact of low-latitude ionospheric scintillation upon the geolocation solution was found to vary from catastrophic to minimal, depending on time, frequency, and radio signal penetration angle through the ionosphere. Highlights of the findings are summarized below.

Geolocation at low latitudes can be severely affected by the nighttime ionosphere. The low latitude scintillation extends from about  $-20$  to  $20$  degrees geomagnetic latitude. The effect on the geolocation solution is three-fold: temporal, frequency, and elevation angle.

### **1. Temporal Impact**

In this report only nighttime ionospheric effects were examined. Nighttime effects are the most severe from one to seven hours after sunset at the magnetic equator. The recurrence rate of scintillation is a function of sun position.

### **2. Frequency Dependence**

The effect of frequency on a geolocation solution depends on which system (TDOA, AOA, or FDOA) is employed. In general, when scintillation is present, signals below one megahertz are so severely disturbed that geolocation using any of the methods is impossible, where the signal path is through the low-latitude ionosphere. For microwave frequencies (above 10 gigahertz), minimal disturbance occurs for any of the geolocation methods. Frequencies between these two limits are affected by varying levels of severity.

The preferred position for the geolocation receiver is directly above the emitter, at a 90 degree elevation angle from the terrestrial-based transmitter. For

comparison, an elevation angle of 90 degrees is assumed, with the receiver at 1000 km altitude. At three TEC units of scintillation standard deviation, errors generated from the scintillated portion of the geolocation solution are:

Overhead Geolocation Errors

<u>Frequency (MHz)</u>	<u>TDOA (km)</u>	<u>FDOA (Hz)</u>	<u>AOA (km)</u>
1	1200	24	7860
10	12	2.4	79
100	0.12	0.24	0.8
1000	0.0012	0.024	0.008

### 3. Elevation Angle Dependence

The elevation angle is defined from the point of view of the terrestrial transmitter, with the vertical transmission direction at 90 degrees and a horizontal launch at zero-degree elevation angle. The degree of degradation of the arriving signal is highly dependent upon the elevation angle. A receiver positioned directly above the transmitter has the maximum resolution, with lower elevation angles producing worse solutions. For example, at 40 degrees elevation, the scintillation magnitude increases by 13%, at 30 degrees by 50%, and at 20 degrees by 700%. This elevation angle effect is illustrated in the computations of Paragraph 2, repeated below for 20 degrees elevation.

### Geolocation Errors at Twenty Degree Elevation Angle

<u>Frequency (MHz)</u>	<u>TDOA (km)</u>	<u>FDOA (Hz)</u>	<u>AOA (km)</u>
1	8680	174	56000
10	87	17.4	560
100	0.87	1.74	6
1000	0.009	0.174	0.06

#### **C. EXTENSIONS OF CURRENT STUDY**

For extending the knowledge and predictive ability gained from this study, several additional investigations are needed. Seven of these follow.

##### **1. Longitudinal Extension**

A useful supplement to the data analysis of this study would be to analyze existing GPS data at other longitudes in the Pacific during the same time period as that of this data set. Data sets that could be helpful are those from Tahiti, Central/South America, and Kwajalein Island. Analysis could assist in determining longitudinal correlation of nighttime equatorial scintillation. If fruitful, an observation of scintillation in Central America could provide information on the probability of scintillation near Hawaii a few hours later. Similarly, scintillation observation in Christmas Island might help predict scintillations over the Phillipines on the same evening.

##### **2. Scintillation Monitoring at Higher Sampling Rate**

No frequency distinctions were found in the scintillation data. One limitation with the data set is the sampling period at Christmas Island and Rarotonga was six

seconds. The JPL data is even more limited, with sampling at 30 seconds. A six-second sampling period restricts the highest observable frequency to 80 millihertz which may be too low. One solution is to collect additional data at a higher sampling rate. This might reveal distinguishing frequency content data at higher frequencies. If scintillation frequencies can be determined, appropriate filters can be constructed to detect scintillation in real time.

### **3. Determine Solar Cycle Dependence**

The GPS data collected here were at solar cycle minimum. This is the best-case scenario, as scintillation becomes worse as the solar cycle increases toward maximum. To determine how the magnitude of scintillation varies with changes in the solar cycle, monitoring low-latitude ionospheric scintillation should be repeated at mid-cycle and cycle maximum. This could be accomplished using the JPL site in Hawaii and a GPS receiver at Christmas Island.

### **4. Develop Daytime Scintillation Models**

This report was concerned primarily with nighttime scintillation effects at low latitudes. In Chapter VII, the equatorial anomalies were shown to contribute afternoon scintillation. This same data set can be analyzed to determine the extent of scintillation magnitude during the daytime.

### **5. Real-Time Nowcasting**

Real-time nowcasting can be accomplished using GPS receivers. The analysis conducted here can be expanded to determine the optimum method for attaining that capability. A limitation in this data set is that it is for a comparatively benign

environment where the magnetic equator varies smoothly and constantly with respect to the geographic equator. For better prediction of world-wide behavior, this experiment should be repeated in an area of the world where the environment is not so well behaved. One candidate area is South America where a few GPS receivers could be emplaced to analyze the low latitude scintillation there. This data set would help to generate a real-time nowcasting model for low-latitude scintillation.

## **6. Sensor Augmentation**

It is apparent from the TEP prediction plots of Chapter VI, that not all the controlling variables have been identified. The connection between TEP and the earth's magnetic indices (i.e., the planetary magnetic index,  $K_p$ , and the equatorial magnetic index, DST) is unknown at present. These inputs may improve TEP predictions and are possibilities for refinements.

## **7. Correlate All-Sky Airglow and GPS-TEC**

Scintillation correlation between airglow intensity and TEC scintillation at zenith offered only limited analysis capability. A more meaningful analysis could be attained by correlating, with the GPS measurements, airglow intensity values which are obtained from the same azimuth and elevation as the GPS satellites.





## APPENDIX A. GEOGRAPHIC TO GEOMAGNETIC COORDINATES

In cartesian coordinates the conversion can be computed from geographic to geomagnetic coordinates by (Bhavanani and Vancour, 1991)

$$r_{mag} = \begin{bmatrix} 0.320158 & -0.928599 & -0.187626 \\ 0.945388 & 0.325947 & 0 \\ 0.061156 & -0.177380 & 0.982240 \end{bmatrix} * r_{geog}, \quad (63)$$

where  $r_{mag}$  is the cartesian coordinate vector ( $x_{mag}, y_{mag}, z_{mag}$ ) for the magnetic latitude and longitude and  $r_{geog}$  is the cartesian coordinate vector ( $x_{geog}, y_{geog}, z_{geog}$ ). The cartesian geographical coordinate vector can be found by

$$r_{geog} = \begin{bmatrix} x_{geog} \\ y_{geog} \\ z_{geog} \end{bmatrix} = \begin{bmatrix} \cos(\theta_g) * \cos(\phi_g) \\ \cos(\theta_g) * \sin(\phi_g) \\ 0.9966472 * \sin(\theta_g) \end{bmatrix} \quad (64)$$

where  $\theta_g$  is the geographic latitude and  $\phi_g$  is the geographic longitude. Similarly,  $\theta_m$  is used for the geomagnetic latitude and  $\phi_m$  for the geomagnetic longitude. The numerically modified z component in Eq. 64 accounts for the earth's eccentricity.



## APPENDIX B. MAGNETIC DECLINATION ANGLE

The magnetic declination angle,  $\Delta$ , is the angle, with the point of interest  $(\theta_g, \phi_g)$  on earth as the apex, formed by the lines drawn from the point of interest to true north and to magnetic north as shown in Figure 84.

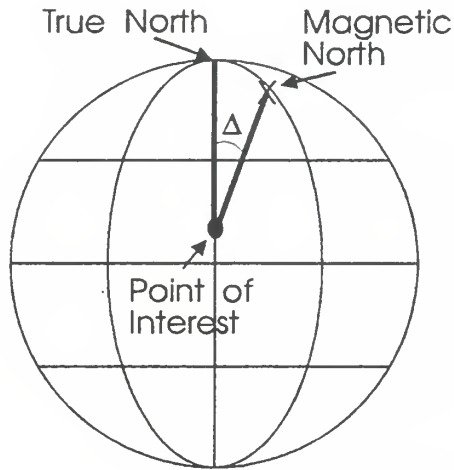


Figure 84 Magnetic Declination Angle.

After computing the magnetic coordinates of the point of interest, as detailed in Appendix A, the magnetic declination angle can be computed. By incrementing the point of interest a minuscule amount toward true north, finding the magnetic coordinates of the new point, then comparing the angular changes, the declination angle can be computed. This is shown in Figure 85.

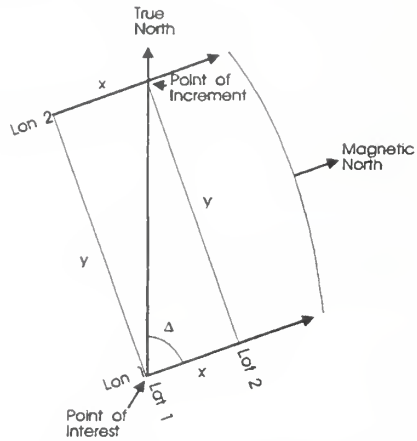


Figure 85 Computing the Magnetic Declination Angle

From the figure, the length of  $y$  can be seen to be the difference between the two longitudes multiplied by the cosine of the latitude, i.e.,

$$y = (lon1 - lon2) * \cos(lat1) \quad (65)$$

and that  $x$  is the difference of the two latitudes,

$$x = lat2 - lat1. \quad (66)$$

With these relationships the magnetic declination angle can then be found as

$$\Delta = \tan^{-1}\left(\frac{y}{x}\right). \quad (67)$$

## APPENDIX C. SOLAR MAGNETIC ANGLE

As the earth precesses, its axis tilts with respect to the ecliptic plane of the sun. The earth tilts toward the sun in spring and summer months and tilts away in fall and winter. On the days of equinox, the tilt is zero and the sun is directly over the earth's equator. The tilt maxima occur on the solstices with magnitudes of  $\pm 23.5^\circ$ , with positive being when the northern hemisphere is tilted toward the sun.

The solar declination angle is the angle formed (at the center of the earth) between the earth's and sun's ecliptic planes. The declination angle limits, as with the tilts, are  $\pm 23.5^\circ$ .

The vernal equinox, March 21 of each year, which is day 80 on the Julian calendar in non-leap years, marks the transition between a negative to a positive declination angle. Assuming a sinusoidal variation, an appropriate equation for the solar declination angle is

$$\delta = 23.5 \sin \left( \frac{2\pi(JD - 80)}{365} \right), \quad (68)$$

where JD is the Julian date of the day of interest.

This equation for the solar declination angle is based upon the assumption of sinusoidal tilt variation. For many applications, this equation yields acceptable accuracy. For additional accuracy, the empirically based formulation given by Bourges (1985) can be entered into a programmable device such as a calculator or

PC. A MATLAB program to compute the solar declination angle in this manner is given in Appendix D7.

The magnetic declination angle is the angle formed when great-circle lines are drawn from a point-of-interest to both the geographic and magnetic poles. A MATLAB program to compute the magnetic declination angle is given in Appendix D5.

When the point-of-interest is on the equator, the magnetic declination angle indicates not only the angular offset of the magnetic from the geographic poles, but also the tilt of the magnetic equator with respect to the geographic equator. For example, if the magnetic north pole is offset  $10^\circ$  eastwardly from the geographic north pole at some point-of-interest on the geographic equator, the magnetic equator will be likewise tilted  $10^\circ$  from the geographic equator.

If an eastward magnetic declination angle is defined as positive (and westward negative), a comparison can be made between the solar and magnetic declination angles. When they are the same, the sun will set on the magnetic equator. The *solar magnetic angle* is the difference between the solar declination and the magnetic declination angles. With the magnetic declination angle given as  $10^\circ$  from above, on approximately Julian days 106 and 239 the solar magnetic angle will be zero.



## APPENDIX D. TEP PREDICTION PROGRAMS

The prediction programs developed in Chapter VI are listed in this appendix. The programs are written modularly so that each module may be easily converted to a subroutine for the parent program in the parent language. Each module is listed in a sub-appendix starting with the main program in sub-appendix D1.



## D1. MAIN

```
% File Name: main.m
%
% Purpose:  Serves as the controlling program to call the subroutines
%           and collects input data.
%
% Inputs:   year, julian day, solar flux, frequency of transmission
%
% Output:   Predicted opening time of circuit, closing time of circuit,
%           path loss, and probability of circuit existing
%
% Author:   R. Smith
% Mod Date: 26 June 1996

%Programs called:  getsites.m, gtcirc.m, findeq.m, geo2mag.m, tepchk.m,
%                 decang.m, opetime.m, clostime.m, prob.m, ploss.m

% Initialize

dtr = pi/180;

% Get input data

year = input('Enter the current year (e.g., 1996): ');
jday = input('Enter Julian Day (e.g., 319): ');
flux = input('Enter the 10.7 cm Solar Flux: ');
freq = input('Enter the frequency of interest (in MHz): ');

% Call getsites to enter the latitudes and longitudes of the
% transmit and receive sites.

getsites

% Call gtcirc to find the great circle azimuths between the sites
% and the distance between them.

gtcirc

% Call findeq to get the longitude of the equatorial crossing point
% of the path between the two sites.

equator_long = findeq(s2n,n2s,latn,lonn,lats,lons)/dtr;
```

```
% Convert site geographic coordinates to geomagnetic coordinates  
% and get magnetic declination angle
```

```
[maglatn,maglonn,ma] = geo2mag(latn,lonn);  
[maglats,maglons,ma] = geo2mag(lats,lons);  
[maglateq,magloneq,ma] = geo2mag(0,equator_long);
```

```
% Check to see if locations are within TEP limits.
```

```
tepchk
```

```
% Get today's solar zenith angle and filtered solar magnetic angle
```

```
[fsma,chi] = decang(year,jday,ma);
```

```
% Compute circuit opening time
```

```
opetime
```

```
% Compute circuit closing time
```

```
clostime
```

```
% Compute probability of circuit actually opening
```

```
prob
```

```
% Compute path loss
```

```
ploss
```

## D2. GETSITES

```
% File Name: getsites.m
%
% Purpose:  Prompts user for the latitudes and longitudes of the
%           two points of interest (transmit site and receive
%           site).  A library of named sites can be augmented so
%           that often used sites can be entered by name.
%
% Inputs:   There are three ways to enter the latitudes and
%           longitudes: 1) site name, 2) decimal degrees, and
%           3) degrees and minutes.
%
% Author:   R. Smith
% Mod Date: 24 April 1996

% Programs Called: hr2deg.m

%Build library of named sites

raro = [-21.22 -159.74];
khon = [21.32 -157.85];
np = [ 90 0];
sp = [-90 0];

%Display information concerning orientation of data

line1 = ['The following inputs assume north and east as positive,'] ;
line2 = ['south and west as negative.'];
disp(line1)
disp(line2)
clear line1; clear line2

% Initialize

ce = 'n';

% Input northernmost latitude until correct (indicated by 'y')

while ce ~= 'y'

% Determine if data is in degrees, minutes (1), a named site (2),
% or in degrees and tenths of degrees.
```

```

line1 = ['If northernmost latitude is in DDHHMM enter 1,'];
disp(line1)
clear line1
hrmin = input('site name 2; (otherwise any other key): ');

if hrmin == 1;
    lat = input('Enter latitude in DD.HHMM: ');
    North_latitude = lat
    clear North_latitude
    latn = hr2deg(lat);
    ce = input('Is this the correct latitude? (y/n): ','s') ;

elseif hrmin == 2
    loc = input('Enter the name of the location of the northernmost site: ','s')
    dummy = eval(loc);
    latn = dummy(1);
    lonn = dummy(2);
    ce = 'y';

else
    latn = input('Enter latitude in DD.decimal: ');
    North_latitude = latn
    clear North_latitude
    ce = input('Is this the correct latitude? (y/n): ','s') ;
end

% End While
end

% Reinitialize for longitude

ce = 'n';

% If a site name was entered the longitude is already recorded
% so that this while block can be skipped

if hrmin == 2;
    ce = 'y';
end

%Input northernmost longitude until correct (indicated by 'y')

while ce ~= 'y';

```

```

line1 = ['If northernmost longitude is in DDHHMM type 1,'];
disp(line1)
hrmin = input( '(otherwise any other key): ');

if hrmin == 1;
    lon = input('Enter longitude in DD.HHMM: ');
    North_longitude = lon
    clear North_longitude
    lonn = hr2deg(lon);
    ce = input('Is this the correct longitude? (y/n): ','s') ;
else
    lonn = input('Enter longitude in DD.decimal: ');
    North_longitude = lonn
    clear North_longitude
    ce = input('Is this the correct longitude? (y/n): ','s') ;
end

% End While
end

% Reinitialize for southern point

ce = 'n';

while ce ~= 'y';

line1 = ['If southernmost latitude is in DDHHMM type 1,'];
disp (line1)
hrmin = input('site name 2, (otherwise any other key): ');

if hrmin == 1;
    lat = input('Enter latitude in DD.HHMM: ');
    South_latitude = lat
    clear South_latitude
    lats = hr2deg(lat);
    ce = input('Is this the correct latitude? (y/n): ','s') ;

elseif hrmin == 2
    loc = input('Enter the name of the location of the southernmost site: ','s');
    dummy = eval(loc);
    lats = dummy(1);
    lons = dummy(2);
    ce = 'y';

```



```

else
    lats = input('Enter latitude in DD.decimal: ');
    South_latitude = lats
    clear South_latitude
    ce = input('Is this the correct latitude? (y/n): ','s') ;
end
end

ce = 'n';
if hrmin == 2 ce = 'y';
end

while ce ~= 'y'

line1 = ['If southernmost longitude is in DDHHMM, type 1,']
disp(line1)
hrmin = input('(otherwise any key): ');

if hrmin == 1;
    lon = input('Enter longitude in DD.HHMM: ');
    South_longitude = lon
    clear South_longitude
    lons = hr2deg(lon);
    ce = input('Is this the correct longitude? (y/n): ','s') ;

else
    lons = input('Enter longitude in DD.decimal: ');
    South_longitude = lons
    clear South_longitude
    ce = input('Is this the correct longitude? (y/n): ','s') ;
end
end

clear lat; clear lon; clear ce; clear hrmin

% Keep longitudes between 0 and 360 degrees

if lonn < 0
    lonn = lonn + 360;
end
if lons < 0
    lons = lons + 360;
end

```

### D3. GTCIRC

```
% File Name:      gtcirc.m
%
% Purpose:   Find the distance between and the great circle
%            azimuths between two lat/long positions on earth,
%            specifically the transmit and receive sites.
%
% Inputs:    The northernmost latitude (latn), northernmost
%            longitude (lonn), the southernmost latitude (lats),
%            and the southernmost longitude (lons). (All in degrees)
%
% Outputs:   Great circle azimuths between the two sites
%            (X and Y in radians) and the distance between them
%            (Z in radians).
%
% Author:    R. Smith
% Mod Date:  24 April 1996

% Initialize

dtr = pi/180;

%Prevent divide by zero in equations below

if (90 - latn < 0.001 )
    n2s = pi/2;
    s2n = 0;
    dist = pi/2 - lats*dtr;

elseif (90 + lats < 0.001)
    n2s = pi/2;
    s2n = 0;
    dist = pi/2 + latn*dtr;
else

% Use spherical trig to determine the great circle azimuths from
% each point to the other (X and Y) and the distance between them
% in radians (Z).

cosdist = sin(latn*dtr)*sin(lats*dtr);
cosdist = cosdist + cos(latn*dtr)*cos(lats*dtr)*cos((lons - lonn)*dtr);
```

```

cosdist = max(cosdist, -1);
cosdist = min(cosdist, 1);

dist = acos(cosdist);

cosn2s = (sin(lats*dtr) - sin(latn*dtr)*cosdist)/(cos(latn*dtr)*sin(dist));
coss2n = (sin(latn*dtr) - sin(lats*dtr)*cosdist)/(cos(lats*dtr)*sin(dist));

cosn2s = max(cosn2s, -1);
cosn2s = min(cosn2s, 1);
coss2n = max(coss2n, -1);
coss2n = min(coss2n, 1);

n2s = acos(cosn2s);
s2n = acos(coss2n);

if (sin((lons - lonn)*dtr) <= 0)
    n2s = 2*pi - n2s;
else
    s2n = 2*pi - s2n;
end

if s2n > 2*pi
    s2n = s2n - 2*pi;
end

if s2n < (-2*pi)
    s2n = s2n + 2*pi;
end

if n2s > 2*pi
    n2s = n2s - 2*pi;
end

if n2s < (-2*pi)
    n2s = n2s + 2*pi;
end

end

```

#### D4. FINDEQ

```
% File Name: findeq.m
%
% Purpose:   Given two points north and south of the equator
%            finds the point on the equator which lies on
%            the great circle between the two points.
%
% Inputs:    great circle azimuth from southern point to
%            northern point (X), great circle azimuth from
%            northern point to southern point (Y), latitude
%            and longitude of northern point (latn & lonn),
%            latitude and longitude of southern point (lats
%            lons)
%
% Output:    longitude of equatorial great circle intersection
%            between the two input points (newlon)
%
% Mod Date: 24 April 1996

function [newlon] = findeq(X,Y,latn,lonn,lats,lons)

%Initialize

dtr = pi/180;
newlat = pi/4;

%For fewest iterations migrate toward the equator from the point
%which is closer to the equator. Determine which point is closer
%and assign its latitude to the variable lat, its longitude to
%lon and the great circle azimuth toward the other point as hdg.

if (abs(latn) >= abs(lats))
    lat = lats*dtr;
    lon = lons*dtr;
    hdg = X;
else
    lat = latn*dtr;
    lon = lonn*dtr;
    hdg = Y;
end

%Perform iterations to tolerance of within 0.01 radians away from
```

```
%equator.
```

```
while ( abs(newlat) > 0.01)
```

```
%Set distance to move toward the equator to an amount equal  
%to the value of the latitude.
```

```
    dist = abs(lat);
```

```
%Find new latitude after moving distance dist toward equator
```

```
    sinNewlat = sin(lat)*cos(dist) + cos(lat)*sin(dist)*cos(hdg);  
    newlat = asin(sinNewlat);
```

```
%Find new longitude after moving distance dist toward equator
```

```
    sinDeltaLon = sin(dist)*sin(hdg)/cos(newlat);  
    DeltaLon = asin(sinDeltaLon);  
    newlon = lon + DeltaLon;
```

```
%Maintain  $0 < \text{newlon} < 2\pi$ 
```

```
    if (newlon < 0)  
        newlon = newlon + 2*pi;  
    end
```

```
    if (newlon > 2*pi)  
        newlon = newlon - 2*pi;  
    end
```

```
%Find azimuth from new point toward equator along great circle
```

```
    sinNewHdg = cos(lat)*sin(hdg)/cos(newlat);  
    newhdg = asin(sinNewHdg);
```

```
%Ensure that new azimuth is reverses direction if the equator  
%is overshot.
```

```
    if (lat > newlat)  
        if (DeltaLon > 0)  
            newhdg = pi - newhdg;  
        else  
            newhdg = -pi - newhdg;
```

```

        end
    end

%keep  $0 < \text{newhdg} < 2\pi$ 

    if (newhdg >  $2\pi$ )
        newhdg = newhdg -  $2\pi$ ;
    end

    if (newhdg < 0)
        newhdg = newhdg +  $2\pi$ ;
    end

%Assign new values for next iteration

    lat = newlat;
    lon = newlon;
    hdg = newhdg;

end

```





## D5. GEO2MAG

```
% File Name: geo2mag.m
%
% Purpose:   Given the geographic latitude and longitude of the
%            point of interest, the geomagnetic latitude and
%            longitude are computed. The magnetic declination
%            angle is also computed.
%
% Note:      The declination angle is the difference between
%            true north and magnetic north at the point of interest.
%            This value can be found from a navigation chart
%            or a geographic to geomagnetic conversion program.
%
% Inputs:    geographic latitude and longitude in degrees (lat and lon).
%
% Outputs:   geomagnetic latitude and longitude in degrees
%            (latm and lonm) and the magnetic declination angle
%            in degrees (magangle).
%
% Mod Date: 26 April 1996
% Author:   R. Smith

function [latm,lonm,magangle] = geo2mag(lat,lon)

%Initialize

dtr = pi/180;
bump = 0.00001;

%Convert to radians

latr = lat*dtr;
lonr = lon*dtr;

%Bump the latitude to make comparison from which to determine
%the magnetic declination.

lat1 = latr + bump;

%Convert from spherical to cartesian. The z component accounts
%for the earth eccentricity.
```

```

x = cos(latr)*cos(lonr);
y = cos(latr)*sin(lonr);
z = 0.9966472*sin(latr);

x1 = cos(lat1)*cos(lonr);
y1 = cos(lat1)*sin(lonr);
z1 = 0.9966472*sin(lat1);

%Geographic to geomagnetic conversion matrix

m = [ 0.320158 -0.928599 -0.187626
      0.945388 0.325947 0
      0.061156 -0.177380 0.982240];

xmag = m * [x; y; z];

%Convert back to spherical

x2 = xmag .* xmag;
theta = acos(xmag(3)/sqrt(x2(1)+x2(2)+x2(3)));
phi = atan2(xmag(2),xmag(1));

latm = (pi/2 - theta)/dtr;
lonm = phi/dtr;

x1mag = m * [x1; y1; z1];
x2 = xmag .* xmag;

theta = acos(x1mag(3)/sqrt(x2(1)+x2(2)+x2(3)));
phi = atan2(x1mag(2),x1mag(1));

lat2 = (pi/2 - theta)/dtr;
lon2 = phi/dtr;

magangle = atan( (lonm-lon2)*cos(latm*dtr)/abs((lat2-latm)))/dtr;

```

## D6. TEPCHK

```
% File Name: tepchk.m
%
% Purpose:  Determine if the two sites are within the geomagnetic
%           limit to make TEP probable
%
% Inputs:   magnetic latitude and longitude of transmit and receive sites
%
% Author:   R. Smith
% Mod Date: 20 June 1996

% Initialize

transflag = 0;
latflag = 0;
lonflag = 0;

% Check to see that two sites are in opposite hemispheres

if (sign(maglatn) ~= sign(maglats))
    transflag = 1;
end

% Check latitudes

latmin = min(abs(maglatn),abs(maglats));
latmax = max(abs(maglatn),abs(maglats));

if ((latmin >= 14) & (latmax <= 26))
    latflag = 1;
end

% Check longitudes

abslon = abs(maglonn - maglons);
if abslon <= 8
    lonflag = 1;
end

% Set TEP flag as 1 for sites within limits, 0 otherwise

if ((transflag + latflag + lonflag) == 3)
```

```

        tepflag = 1;
else
        tepflag = 0;
end

```

## D7. DECANG

```
% File Name: decang.m
%
% Purpose:   Computes the declination angle of the sun at noon (GMT)
%            on the specified day. The day of the spring equinox
%            is computed and saved as n0.
%
% Inputs:    year (year), Julian day of year (n), and magnetic declination
%            angle (ma)
%
% Outputs:   solar declination angle in degrees (d), value of filtered
%            solar magnetic angle angles (dec), and day of spring equinox
%            (n0)
%
% Author:    R. Smith
% Mod Date:  24 April 1996

% This algorithm is based on the article by Bourges (1985)

function [fsma,d] = decang(year,jday,ma)

%Initialize

w = 360/365.2422;
dtr = pi/180;
dec = [];
summag = 0;

%Normalize year to reference

ref = year - 1969;

%Compute spring equinox

n0 = 78.801 + (.2422 * ref) - floor(ref/4);

%Compute the solar declination angle for current and previous 149 days

for n = jday-149:jday

t = n - .5 - n0;
phi = w * t * dtr;
```

```

d = .3723 + (23.2567*sin(phi)) ;
d = d + .1149*sin(2*phi) - .1712*sin(3*phi) ;
d = d - .7580*cos(phi) + .3656*cos(2*phi) + .0201*cos(3*phi);

% Find solar magnetic angle (SMA) and cos(SMA)

sma = d - ma;
cossma = cos(sma*dtr);

% Integrate cos(SMA) with previous values

summag = summag + cossma;

end

% Normalize integrated cos(SMA) values (providing filtering)

summag = summag/150;

% Add the value of today's cos(SMA) and the filtered previous values

fsma = cossma + summag;

```

## D8. OPETIME

```
% File Name: opetime.m
%
% Purpose:  compute the predicted opening time of the TEP circuit
%
% Inputs:   solar flux (flux), solar zenith angle (chi)
%
% Output:   Circuit Opening Time (ot)
%
% Author:   R. Smith
% Mod Date: 26 June 1996

% Initialize

dtr = pi/180;

% Compute the opening time derived from solar flux

otf = 0.0000181*(flux.^2) - 0.0123 * flux + 9.46;

% Compute the opening time based on today's solar zenith angle

otchi = 18.61 - 10.76 * cos(chi * dtr);

% Compute opening time using both flux and chi

otfx = otf .* otchi;

ot = 0.011 * (otfx.^2) - 1.334 * otfx + 61.46
```





## D9. CLOSTIME

```
% File Name: clostime.m
%
% Purpose:  compute the predicted closing time of the TEP circuit
%
% Inputs:   solar flux (flux), solar zenith angle (chi)
%
% Output:   Circuit Closing Time (ct)
%
% Author:   R. Smith
% Mod Date: 26 June 1996

% Initialize

dtr = pi/180;

num = flux * sin(chi*dtr) + 10;

ras = num/100;

ct = exp(ras) + 23.4
```



## D9. PROB

```
% File Name: prob.m
%
% Purpose:  compute the probability of TEP circuit opening
%
% Inputs:   solar flux (flux), filtered solar magnetic angle (fsma),
%           magnetic declination angle (ma)
%
% Output:   Circuit Opening probability (cprob)
%
% Author:   R. Smith
% Mod Date: 26 June 1996

% Normalize sum of cosine of solar magnetic angle added to the
% filtered value to have maximum of one and minimum of zero

% Find maximum and minimum of sum which is function of
% the magnetic declination angle

maxsum = -0.00000294673148 * (ma ^ 3) - 0.00009418067769 * (ma ^ 2);
maxsum = maxsum + 0.00480080226611 * ma + 1.95151868361121;

minsum = -0.00026774397313 * (ma ^ 2) - 0.00936506722977 * ma +
1.88527023661150;

% Find the normalized filtered cos(SMA)

diff = maxsum - minsum;
drop = minsum/diff;

redsma = fsma/diff;
normsma = redsma - drop;
normsma = min(normsma,1);
normsma = max(normsma,0);

% Compute probability envelope from solar flux and circuit probability

env = flux/480 + .6;
env = min(env,1);
env = max(env,0);
```

```
cprob = env * normsma;  
cprob = min(cprob,0.99);  
cprob = max(cprob,0.01);
```

```
% Set probability to zero if frequency is outside allowable range
```

```
if (freq < 2) + (freq > 200)  
    cprob = 0;  
end
```

```
% Set probability to zero if transmitter or receiver location is  
% out of range
```

```
if (tepflag == 0)  
    cprob = 0;  
end
```

## D10. PLOSS

```
% File Name: ploss.m
%
% Purpose:  Compute the path loss of the circuit from the transmitte
%           to the receiver.
%
% Inputs:   magnetic latitudes and longitudes of the transmitter and receiver,
%           the predicted opening and closing times of the circuit, and
%           the
%           transmission frequency
%
% Output:   path loss in dB
%
% Author:   R. Smith
% Mod Date: 26 Jun 1996

% Initialize

tvec = [];
lossvec = [];

% Compute geographical loss for northern location

maglat = abs(maglatn);

if maglat <= 18
    latfn = cos(2*pi*(maglat-18)/16);
else
    latfn = cos(2*pi*(maglat-18)/32);
end

% Compute geographical loss for southern location

maglat = abs(maglats);

if maglat <= 18
    latfs = cos(2*pi*(maglat-18)/16);
else
    latfs = cos(2*pi*(maglat-18)/32);
end

% Compute longitudinal difference loss
```

```

delong = maglonn - maglons;
lonf = cos(2*pi*delong/32);

% Compute total losses as function of time for predicted circuit
% duration of path. Eleven points are computed during this time

dur = ct - ot;

% Bump the duration inward from the extremes to prevent log(0)

bumpdur = dur - 2e-6;
inc = bumpdur/10;
optloss = 93 + 20 * log10(freq);

for t = (ot+1e-6):inc:(ct-1e-6)

    tlf = sin(pi*(t - ot)/dur);
    loss = optloss - 10 * log10(latfn) - 10 * log10(latfs);
    loss = loss - 10 * log10(lonf) - 10 * log10(tlf);

    lossvec = [lossvec loss];
    tvec = [tvec t];

end

```



## APPENDIX E. PROBABILITY OF SCINTILLATION

Two MATLAB programs are included in this appendix. The first, prob.m, predicts the probability of scintillation occurrence at low latitudes. The second program, solar.m, is called from within prob.m.

### E1. PROB.M

```
% File Name: prob.m
%
% Purpose:          compute the probability of equatorial scintillation
%
% Inputs:           solar flux (flux), filtered solar magnetic angle (fsma),
%                   Julian Day (jday), magnetic declination angle (ma)
%
% Output:           Scintillation probability of occurrence (sprob)
%
% Author:           R. Smith
% Mod Date: 22 Feb 1998

% Get inputs

jday = input('Enter the Julian Day of interest ==> ');
year = input('Now the year for that day ==> ');
flux = input('And the solar flux for that day ==> ');
ma = input('Enter the magnetic declination angle ==> ');
[fsma,dec] = decang(year,jday,ma);

% Normalize sum of cosine of solar magnetic angle added to the
% filtered value to have maximum of one and minimum of zero

% Find maximum and minimum of sum which is function of
% the magnetic declination angle

maxsum = -0.00000294673148 * (ma ^ 3) - 0.00009418067769 * (ma ^ 2);
maxsum = maxsum + 0.00480080226611 * ma + 1.95151868361121;

minsum = -0.00026774397313 * (ma ^ 2) - 0.00936506722977 * ma +
1.88527023661150;

% Find the normalized filtered cos(SMA)
```

```
diff = maxsum - minsum;  
drop = minsum/diff;
```

```
redsma = fsma/diff;  
normsma = redsma - drop;  
normsma = min(normsma,1);  
normsma = max(normsma,0);
```

```
% Compute probability envelope from solar flux and circuit probability
```

```
env = flux/480 + .6;  
env = min(env,1);  
env = max(env,0);
```

```
sprob = env * normsma;  
sprob = min(sprob,0.99);  
sprob = max(sprob,0.01)
```

## E2. SOLAR.M

```
function [fsma,d] = solar(year,jday,ma)

% File Name: solar.m
%
% Purpose:   Computes the declination angle of the sun at noon (GMT)
%           on the specified day and the filtered value for the previous 150
%           days.
%           The day of the spring equinox is computed and saved as n0.
%
% Inputs:    year (year), Julian day of year (n), and magnetic declination
%           angle (ma)
%
% Outputs:   solar declination angle in degrees (d), value of filtered
%           solar magnetic angle (fsma)
%
% Author:    R. Smith
% Mod Date:  22 Feb 1998

% This algorithm is based on the article by Bourges (1985)

%Initialize

w = 360/365.2422;
dtr = pi/180;
dec = [];
summag = 0;

%Normalize year to reference

ref = year - 1969;

%Compute spring equinox

n0 = 78.801 + (.2422 * ref) - floor(ref/4);

%Compute the solar declination angle for current and previous 149 days

for n = jday-149:jday

t = n - .5 - n0;
```

```

phi = w * t * dtr;
d = .3723 + (23.2567*sin(phi)) ;
d = d + .1149*sin(2*phi) - .1712*sin(3*phi) ;
d = d - .7580*cos(phi) + .3656*cos(2*phi) + .0201*cos(3*phi);

% Find solar magnetic angle (SMA) and cos(SMA)

sma = d - ma;
cossma = cos(sma*dtr);

% Integrate cos(SMA) with previous values

summag = summag + cossma;

end

% Normalize integrated cos(SMA) values (providing filtering)

summag = summag/150;

% Add the value of today's cos(SMA) and the filtered previous values

fsma = cossma + summag;

```

## APPENDIX F. SCINTILLATION MAGNITUDE PREDICTION

This appendix contains one MATLAB program, `scintdist`, which predicts the magnitude of scintillation in TEC units at a given time after sunset and a geomagnetic latitude.

```
% Name:  SCINTDIST.M
% Purpose: Compute predicted magnitude at given time and place
%
% Inputs: time after sunset (tas) and magnetic latitude (maglat)
%
% Output: Predicted scintillation magnitude (scintmag) in TEC units

% Author:  R. Smith
% Last Mod: 26 Feb 98

% Get time after sunset input

tas = input('Enter time (in hours) after sunset (1 - 7) ==> ');

% Find amplitude as function of time

if tas < 1
    error('Minimum time is one hour after sunset');
elseif tas > 7;
    error('Maximum time is seven hours after sunset');
elseif tas <= 5.5
    timemag = 3.5*(1-exp(-(tas - 1)/.9));
else
    timemag = 3.5*exp(-(t - 5.5)/.3);
end

% Find peak latitude as function of time

peaklat = 12 * cos(2*pi*(tas - 2)/17.5);

% Get magnetic latitude input

maglat = input('Enter the magnetic latitude of interest ==> ');
maglat = abs(maglat);
```

```
% Comput magitude factor based upon latitude
```

```
if maglat >= peaklat
```

```
    latfactor = cos(2*pi*(peaklat - maglat)/12);
```

```
else
```

```
    latfactor = cos(2*pi*(peaklat - maglat)/32);
```

```
end
```

```
latfactor = (latfactor + 1)/2;
```

```
scintmag = timemag * latfactor
```

## LIST OF REFERENCES

- Bhavnani, K. H. and R. P. Vancour, "Coordinate Systems For Space and Geophysical Applications," Phillips Laboratory Scientific Report No. 9, 1991.
- Bourges, B., "Improvement in Solar Declination Computation," *Solar Energy*, Vol. 35, 1985.
- Chen, Francis F., *Introduction to Plasma Physics and Controlled Fusion*, Plenum Press, 1984.
- Cracknell, R. G., R. A. Whiting, "Twenty-one Years of TE," *Radio Communication*, June/July, 1980.
- Davies, Kenneth, *Ionospheric Radio*, Peter Peregrinus Ltd., 1990.
- Fejer, B. G., et al., "F Region East-West Drifts at Jicamarca," *Journal of Geophysical Research*, Vol. 86, No. A1, 1981.
- Forbes, Jeffrey M., "The Equatorial Electrojet," *Reviews of Geophysics and Space Physics*, Vol. 19, No. 3, 1981.
- Hargreaves, J. K., *The Solar-Terrestrial Environment*, Cambridge, 1992.
- Heron, M. L., "Recent Progress in Transequatorial Propagation-Review," *Journal of Atmospheric and Terrestrial Physics*, Vol. 43, No. 5/6, 1981.
- Hunsucker, R. D., *Radio Techniques for Probing the Terrestrial Ionosphere*, Springer-Verlag, 1991.
- Kelley, M. C., *The Earth's Ionosphere*, Academic Press, 1989.
- McNamara, Leo F., *The Ionosphere: Communications, Surveillance, and Direction Finding*, Krieger Publishing Company, 1991.
- Nielson, D. L., "Long-Range VHF Propagation Across the Geomagnetic Equator," Stanford Research Institute Research Report, 1969.
- Nielson, D. L. and George H. Hagn, "Frequency Transformation Techniques Applied to Oblique-Incidence Ionograms," Stanford Research Institute Research Report, 1964.



Platt, I. G. and P. L. Dyson, "VHF Transequatorial Propagation via Three Dimensional Waveguides," *Journal of Atmospheric and Terrestrial Physics*, Vol. 51, No. 11/12, 1989.

Steiger, Walter R., "Low Latitude Observations of Airglow," *Aurora and Airglow*, Edited by B. M. McCormac, Reinhold Publishing Corporation, 1966.

Tsunoda, Roland T., "Time Evolution and Dynamics of Equatorial Backscatter Plumes, 1. Growth Phase," *Journal of Geophysical Research*, Vol. 86, No. A1, 1981.

Weber, E. J., et al., "North-South Aligned Equatorial Airglow Depletions," *Journal of Geophysical Research*, Vol. 83, No. A2, 1978.

Weill, G. M., "Airglow Observations Near the Equator," *Aurora and Airglow*, Edited by B. M. McCormac, Reinhold Publishing Corporation, 1966.

Woodman, Ronald F., "Vertical Drift Velocities and East-West Electric Fields at the Magnetic Equator," *Journal of Geophysical Research, Space Physics*, Vol. 75, No. 31, 1970.

## INITIAL DISTRIBUTION LIST

1. Defense Technical Information Center ..... 2  
8725 John J. Kingman Rd., STE 0944  
Ft. Belvoir, VA 22060-6218
  
2. Dudley Knox Library ..... 2  
Naval Postgraduate School  
411 Dyer Rd.  
Monterey, CA 93943-5100
  
3. Center for Reconnaissance Research ..... 1  
Attn: EC/Po  
Naval Postgraduate School  
Monterey, CA 93943
  
4. Naval Information Warfare Center ..... 1  
Attn: CNSG/Code N9  
9800 Savage Road  
Fort Meade, MD 20755-6000
  
5. Mr. Stuart Kingan ..... 1  
Scientific Research  
Box 66  
Rarotonga  
Cook Islands
  
6. RP Consultants ..... 1  
Attn: Dr. Robert Hunsucker  
7917 Gearhart Street  
Klamath Falls, OR 97601
  
7. Chairman, Code EC ..... 1  
Department of Electrical and Computer Engineering  
Naval Postgraduate School  
Monterey, CA 93943
  
8. Rasler W. Smith, Code EC/Sr ..... 10  
Department of Electrical and Computer Engineering  
Naval Postgraduate School  
Monterey, CA 93943-5000

9. Richard W. Adler, Code EC/Ab ..... 1  
Department of Electrical and Computer Engineering  
Naval Postgraduate School  
Monterey, CA 93943-5000
  
10. CDR Gus K. Lott, Code EC/Lt ..... 1  
Department of Electrical and Computer Engineering  
Naval Postgraduate School  
Monterey, CA 93943-5000
  
11. Wilbur R. Vincent, Code EC/Ab ..... 3  
Department of Electrical and Computer Engineering  
Naval Postgraduate School  
Monterey, CA 93943-5000
  
12. Jeffrey B. Knorr, Code EC/Ko ..... 1  
Department of Electrical and Computer Engineering  
Naval Postgraduate School  
Monterey, CA 93943-500-
  
13. Kenneth L. Davidson, Code MR/Ds ..... 1  
Department of Meteorology  
Naval Postgraduate School  
Monterey, CA 93943-5000
  
14. David D. Cleary, Code PH/Cl ..... 1  
Department of Physics  
Naval Postgraduate School  
Monterey, CA 93943-5000
  
15. Monique Fargues, Code EC/Fa ..... 1  
Department of Electrical and Computer Engineering  
Naval Postgraduate School  
Monterey, CA 93943-5000
  
16. Dr. Donald Nielson ..... 1  
SRI International  
333 Ravenwood Ave.  
Menlo Park, CA 94025









DUDLEY KNOX LIBRARY  
NAVAL POSTGRADUATE SCHOOL  
MONTEREY CA 93943-5101



DUDLEY KNOX LIBRARY



3 2768 00365970 7